POLITECNICO DI TORINO

Master's Degree in Biomedical Engineering

Master's Degree Thesis

He-Check: verification of the repeatability of dose delivery based on the simultaneous acceleration of helium and carbon ions

Supervisors:

Prof. Gianni COPPA
Dr. Marco PULLIA
Dr. Simone SAVAZZI

Candidate:

Carlotta BROGLIA FRATIN

Academic Year 2022/2023

Abstract

Radiation therapy is a cancer treatment technique that uses particle radiation to either kill or control the growth of malignant cells. One of the most promising radiotherapy techniques is hadrontherapy, which uses heavy particles, such as protons and carbon ions, to offer both physical and biological advantages in the treatment of localized tumors. The heavy charged particles have the peculiar characteristic of depositing a large part of their energy at a controlled depth, resulting in the characteristic Bragg's peak. This leads to highly accurate targeting of tumors while sparing the surrounding healthy tissues.

Due to the localized energy deposition of charged particles, high precision is demanded. Range and energy uncertainties make this challenging and affect treatment precision. To address these challenges, advanced techniques like real-time verification methods are required. These methods aim to provide dynamic feedback on patient position and delivered dose, enhancing treatment safety and precision.

At CNAO (*Centro Nazionale di Adroterapia Oncologica*), one of the few facilities offering dual treatment capabilities with protons and carbon ions, a novel system for the real-time verification of the patient position during beam delivery is under development.

The system, called He-Check, employs an ion beam to evaluate the variation of the patient's anatomy during treatment. To this purpose, a fraction of helium ions are accelerated in combination with the primary ^{12}C beam used for therapy. This characteristic permits the joint acceleration of the two ion species.

Helium ions possess almost identical magnetic rigidity at the same velocity and three times the range of carbon ions. By correctly dosing the helium the increase in the dose administered to the patient can be kept under control.

The system exploits a plastic scintillator that, once exposed to the helium beam, generates optic photons detected by a sCMOS sensor.

The present work is focused on the analysis of the spatial and temporal resolution of the

system, with a particular focus on the characterization of the repeatability of measurements.

Spatial resolution was assessed by capturing images at various depths to establish the maximum achievable resolution of the system. Additionally, a mirror was introduced along the axis of the scintillator to have a three-dimensional measurement of the beam. Repeatably and resolution can be assessed by subtracting images, either by administering the same plan or by administering plans with known differences.

Furthermore, a comprehensive evaluation of various acquisition modalities for the sCMOS camera was conducted. The primary objective was to synchronize the proposed acquisition system with the beam time necessary to irradiate a single slice during treatments.

To achieve this synchronization, the output signal from the Dose Delivery System (DDS), which operates in synchrony with the beam-on signal, interfaces with an Arduino device. The DDS generates a 5V digital signal, detected by the Arduino, which subsequently generates a pulse train tailored to trigger the sCMOS camera.

Overall, the proposed system takes another step in the direction of proposing a robust solution for real-time imaging during particle therapy treatments.

Sommario

La radioterapia è una tecnica di trattamento del cancro che utilizza radiazioni, in genere i raggi X, per uccidere o controllare la crescita delle cellule maligne. Una delle tecniche di radioterapia più promettenti è l'adroterapia, che utilizza particelle pesanti come protoni e ioni di carbonio per offrire vantaggi sia fisici che biologici nel trattamento dei tumori localizzati.

Le particelle cariche pesanti hanno la particolare caratteristica di depositare una grande parte della loro energia a una profondità controllata, risultando nel caratteristico picco di Bragg. Ciò porta a un bersagliamento mirato e accurato dei tumori, risparmiando i tessuti sani circostanti.

A causa della deposizione localizzata di energia delle particelle cariche, è richiesta un'elevata precisione. Le incertezze nel range e nell'energia rendono questa sfida difficile e influenzano la precisione del trattamento. Per affrontare queste sfide, sono necessarie tecniche avanzate come i metodi di verifica in tempo reale, che mirano a fornire un feedback dinamico sulla posizione del paziente e sulla dose somministrata, migliorando la sicurezza e la precisione del trattamento.

Presso il CNAO (Centro Nazionale di Adroterapia Oncologica), una delle poche strutture che offre capacità di trattamento duale con protoni e ioni di carbonio, è in fase di sviluppo un sistema innovativo per la verifica in tempo reale della posizione del paziente durante la somministrazione del fascio.

Il sistema, chiamato He-Check, impiega un fascio di ioni per valutare la variazione dell'anatomia del paziente durante il trattamento. A questo scopo, una frazione di ioni di elio viene accelerata in combinazione con il fascio primario di ioni di carbonio utilizzato per la terapia. Questa caratteristica permette l'accelerazione congiunta delle due specie.

Gli ioni elio possiedono, se accelerati alla stessa velocità, una rigidità magnetica quasi identica e una portata tre volte maggiore rispetto agli ioni di carbonio. Dosando correttamente l'elio, l'incremento della dose somministrata al paziente può essere mantenuto sotto controllo.

Il sistema sfrutta uno scintillatore plastico che, una volta esposto al fascio di elio, genera fotoni ottici rilevati da un sensore sCMOS.

Il presente lavoro è incentrato sull'analisi della risoluzione spaziale e temporale del sistema, con particolare attenzione alla caratterizzazione della ripetibilità delle misurazioni.

La risoluzione spaziale è stata valutata catturando immagini a diverse profondità per stabilire la massima risoluzione ottenibile dal sistema. Inoltre, è stato introdotto uno specchio lungo l'asse dello scintillatore per ottenere una misurazione tridimensionale del fascio.
La ripetibilità e la risoluzione possono essere valutate sottraendo le immagini, sia somministrando lo stesso piano o somministrando piani con differenze conosciute.

Inoltre, è stata condotta un'ampia valutazione delle modalità di acquisizione per il sensore sCMOS. L'obiettivo principale era sincronizzare il sistema di acquisizione proposto con il tempo del fascio necessario per irradiare una singola fetta durante i trattamenti.

Per raggiungere questa sincronizzazione, il segnale in uscita dal sistema di somministrazione della dose (Dose Delivery System, DDS), che opera in sincronia con il segnale di accensione del fascio, interagisce con un dispositivo Arduino. Il DDS genera un segnale digitale a 5V, rilevato dall'Arduino, che successivamente genera un treno di impulsi adattato per attivare il sensore sCMOS.

Nel complesso, il sistema proposto compie un ulteriore passo nella direzione di proporre una soluzione robusta per l'imaging in tempo reale durante i trattamenti di terapia con particelle.

Contents

Introduction

Radiation therapy is a type of cancer treatment that predominantly employs X-rays. However, X-rays have limitations in terms of their ability to accurately target tumors since they present a relatively broad distribution of energy within the tissues. Due to these limitations, alternative treatments have gained momentum over the years.

Among these alternatives, hadrontherapy has emerged as a compelling option in the past. Hadrontherapy harnesses charged particles known as hadrons. Many particles fall under this classification, but the ones that are mainly employed in hadrontherapy are protons and ions [1].

Compared to the particles used in conventional photon radiation therapy, hadrons offer better dose conformity to the treatment target. Their characteristic distribution is known as Bragg's peak, allowing for precise targeting of specific tumor types while minimizing exposure to nearby healthy tissues and organs.

Furthermore, their higher Linear Energy Transfer (LET) results in a greater number of double-strand breaks in the DNA, providing additional advantages.

However, as a drawback, various sources of uncertainties arise in hadrontherapy, affecting the treatment plan. This makes it necessary to increase the safety margin and, therefore, reduces the potential benefits. The most critical sources of uncertainty include anatomical changes, setup errors, and inaccuracies in the proton stopping powers in different materials [2].

To address these challenges, various techniques have been explored. In-beam positron emission tomography (PET) has already found clinical application but suffers from the downside of intrinsically low signal.

Another avenue under study is the use of charged particles for their potential in dual-purpose applications. The goal is to utilize the same particle source employed for the treatment to acquire patient radiography before tumor irradiation. However, the main limitation of this technique is that the machine needs to accelerate to energies higher than the clinical ones, and there is an intrinsic impossibility of real-time monitoring [3].

Real-time verification techniques have emerged as a solution to reduce uncertainties by providing dynamic feedback on the ion beam range within the patient during treatment sessions.

A novel system, currently under development at CNAO (*Centro Nazionale di Adroterapia Oncologica*), one of the few facilities in the world to offer dual treatment capabilities with protons and carbon ions, is designed to detect real-time density modifications in the patient compared to the planning CT scan (Computed Tomography).

The central concept of the system, named *He-Check*, involves the use of both ^{12}C and ^{4}He nuclei, for both therapeutic treatment and verification purposes. These nuclei possess similar magnetic rigidity, enabling their joint acceleration and the administration of a combined particle beam to irradiate the patient.

While ^{12}C serves its therapeutic purpose, the system measures the residual range of ^{4}He. This is possible due to the different energy loss of carbon and helium nuclei, resulting in helium having a range approximately three times that of carbon, within the same medium and at the same velocity.

The He-Check system consists of a detector based on a plastic scintillator combined with a scientific CMOS (sCMOS) camera. When exposed to the helium beam, the scintillator generates optical photons, detected by the sCMOS sensor. The choice of sCMOS technology is driven by its higher acquisition speed, greater compactness, and lower cost compared to other sensor technologies.

The present work will initially introduce the theoretical foundations of radiation-matter interaction and the physical characteristics of dose delivery within the target volume. Subsequently, the advantages associated with proton therapy will be explored, followed by an introduction to the layout of CNAO. This section will provide details about the accelerator and the dose distribution system.

The critical topic of patient positioning will be discussed, exploring potential error sources that can impact it. Innovative techniques, such as He-Check, currently under study for this purpose, will be presented, and the achieved results will be discussed in detail.

In Chapter 7, the concept of repeatability in image acquisition is explored. Repeatability denotes the consistency of a feature or characteristic in images acquired under similar conditions. The chapter discusses techniques for assessing repeatability, including background subtraction, and explores post-processing methods to eliminate noise and hot pixels. Additionally, the effectiveness of filtering methods, such as median filtering and re-binning, for noise reduction is examined. The chapter concludes with a comparison of images with paints taken at various depths to evaluate the system's resolution.

In Chapter 8, a significant modification to the experimental setup is introduced involving the integration of a mirror. The addition of the mirror aims to enable a three-dimensional measurement of the beam's characteristics, enhancing the existing two-dimensional assessment. Placed at a 45-degree angle, the mirror's impact on the system's parameters is discussed. Crucial parameters, including the mirror's K value and the coordinates of the beam center at different depths, are carefully evaluated.

In Chapter 9, the potential advantages of adopting an alternative trigger modality for image acquisition are discussed. This modality enables synchronization with the timing events of the treatment by introducing an Arduino. The chapter explores key considerations, such as exposure time, pulse train period, signal loss, and noise levels.

In the appendix, a selection of MATLAB codes developed during the course of this work, as well as the Arduino code necessary to use the external trigger modality, will be included.

Chapter 1

Hadrontherapy

In this chapter, hadrontherapy will be presented as a technique of treatment for patients affected by tumors. The principal characteristics of this treatment will be highlighted, emphasizing its advantages over conventional radiotherapy. This distinction is based on the different mechanisms of interaction with matter and biological tissue.

1.1 Radiotherapy

Radiotherapy, also known as radiation therapy, is a crucial treatment modality in the field of oncology, based on the use of high-energy rays or radioactive substances to damage and inhibit the growth of tumoral cells.

Ionizing radiation is employed to target tumor cells, inducing their clonogenic death, rendering them unable to reproduce and proliferate. This radiation can take the form of neutral particles such as photons or neutrons, or charged particles like protons. The use of these particles causes ionization of the tissues, which can cause damage to cellular components and kill the cells. The target cells are tumor cells but since radiation deposits dose in all tissues also the healthy cells will be damaged. The primary goal of radiotherapy is to minimize damage to healthy cells and maximize the impact on cancerous ones. This is achieved by depositing as much dose[1] as possible in the tumoral tissue.

---

[1] The term 'dose' refers to the amount of radiation energy that is absorbed by a specific tissue or target area within the patient's body. It is a measure of the radiation dose deposited per unit mass of tissue and is expressed in units of Gray (Gy).

1.1.1 History of the treatment of tumors

Before the use of ionizing particle beams, medicine had few options for the treatment of certain diseases. This changed after the discovery of X-rays which happened in 1895 by Wilhelm Conrad Roentgen [4]. In the same year, the phenomenon of radioactivity was beginning to be studied by Antoine Henri Becquerel and a few years later Becquerel and Curie reported on the physiologic effects of radium rays.

The first years of the new century brought forth an increasing number of studies reporting the use of X-rays and radium in medicine, skin cancers being the most frequently treated, but the beneficial results were poor in comparison to the side effects. The first X-ray tubes evolved from experimental Crookes tubes which were used until the 1920s.

In the 1910s Coolidge, improving the Crookes tube, developed a new device called the Coolidge tube, also called the hot cathode tube. The latter uses thermionic emission, where a tungsten cathode is heated to a high enough temperature to be able to emit electrons, which are accelerated toward the anode. Only in the 1920s physicians started to realize the benefits of fractionating the total radiation dose, administering it over multiple sessions instead of a single treatment session. This approach was found to be more effective and could lead to the reduction of the side effects associated with radiotherapy [5]. In 1928 the International Commission on Radiological Protection (ICRP) was created to address the question of radio protection [6].

The following years were characterized by continuous scientific progress, brachytherapy was used, allowing the operators to treat the tumor without an external beam source and limiting the side effects, and super-voltage X-ray tubes were developed, able to deliver energy from 50 kV to 200 kV. Later cobalt teletherapy was introduced and more potent electron linear accelerators were developed (also known as electron LINACS) [7]. The new devices were able to deliver a higher dose of energy, making the treatment of deeper tumors possible. The 1970s and 1980s were characterized by the introduction of innovative devices delivering proton beams, allowing for a treatment that was more controllable and more effective for difficult-to-treat diseases.

1.1.2 Radiotherapy with photons

Nowadays the most widely used treatment modality in the oncology field is X-ray therapy. This treatment employs high-energy X-rays to target cancer cells and can be employed alone or in combination with other therapies, such as surgery or chemotherapy. The energy used in therapy typically ranges from a few hundred kilo electron volts (keV) to a few mega electron volts (MeV), depending on the specific treatment requirements. A typical treatment dose is set to be around 60 Gy, administered in fractions of 2 Gy.

Photons interact with matter through various mechanisms of action, the main ones being the photoelectric effect, Compton effect, and pair production. These mechanisms influence the behavior of X-rays and their interactions with tissues. In Figure 1.1, it can be seen how the photoelectric effect, the Compton effect, and pair production are predominant in various absorbing materials (Z) and at different energies.

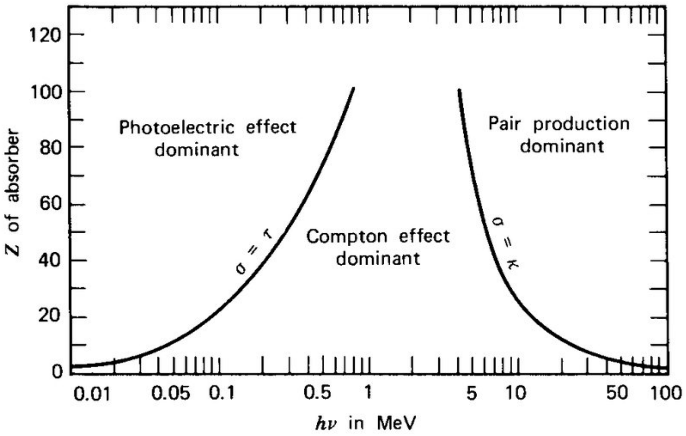

Figure 1.1: Illustration of the relative significance of the photoelectric effect, the Compton effect, and pair production in various absorbing materials (Z) and at different energies [8].

Compton scattering, observed by Arthur H. Compton, is one of the primary interactions that occur between X-rays and matter. In the Compton effect, individual photons collide with single electrons that are free or loosely bound in atoms. Colliding photons transfer some of their energy and momentum to the electron. In the instant of the collision, new photons of less energy and momentum are produced and scattered at an angle that depends on the amount of energy lost during the collision.

The photoelectric effect is another mechanism that plays a significant role in X-ray therapy. X-ray photons interact with an inner-shell electron, ejecting the electron from the atom and depositing all its energy within the tissue. This interaction is more likely to occur at lower X-ray energies and is useful for treating superficial tumors.

Pair production occurs at very high X-ray energies, greater than 1 MeV. In this process, an X-ray photon interacts with the electromagnetic field near the atomic nucleus, resulting in the creation of an electron and a positron. The latter quickly annihilates with an electron, producing two high-energy photons.

All these mechanisms have the peculiarity of generating secondary charged particles (electrons and positrons) that are directly responsible for the ionization of atoms and molecules. These mechanisms result in a decrease in the photon dose in the tissue and, mainly due to the Compton effect, in a high spatial dispersion of the particle beam. These intrinsic characteristics of neutral particles make it challenging to use them for deep-seated tumors, as they limit the ability to conform the dose adequately within the tumor and minimize the dose to surrounding healthy tissue.

To address deep-seated tumors with photons, the conventional strategy involves irradiating the tumor from multiple directions, aggregating the dose within the tumor and dispersing it across a substantial volume of healthy tissue. An alternative approach, however, emerges with the utilization of charged particles known as hadrons.

1.2 Hadrontherapy

Hadrontherapy represents an innovative form of radiation therapy that utilizes hadrons (hence the name hadrontherapy) as projectile particles. Hadrons are particles composed of quarks and antiquarks and are subject to the strong nuclear force. In hadrontherapy, the predominantly used particles are protons and light ions such as He^{2+}, C^{6+} e O^{8+}. Unlike photons, which are neutral particles, the charged particles interact with the matter with different mechanisms of action than those seen in the previous paragraph.

A charged particle can lose its energy through two different mechanisms:

- Through *collision*: the particle transfers its energy to atoms and molecules of the matter it collides with. The energy released to these particles can alternatively cause their excitation or ionization.
- Through *irradiation*: the charged particle is slowed down and deflected from its trajectory due to the interaction with the Coulombic electrostatic field of the nuclei of the material which is traversed. This causes the emission of X-rays of continuous spectrum by the moving particle, and consequently the loss of energy (Bremsstrahlung phenomenon).

The contribution of the energy loss through irradiation depends on the inverse square of the projectile's mass. For ions, it is negligible even at extremely high energies; therefore this term will not be considered.

By focusing on the collisional term, the energy loss behavior can be described through the Bethe Bloch equation, provided below (Equation 1.1):

$$-\frac{dE}{dx} = k^2 \cdot NZ \cdot \frac{4\pi \mathrm{e}^4 \mathrm{z}^2}{\mathrm{m_e v}^2} \cdot \left(\ln \frac{2m_e \mathrm{v}^2}{I} - \ln(1-\beta^2) - \beta^2 \right) \tag{1.1}$$

- N = atomic density of the target [cm^{-3}]
- Z = atomic number of the target
- z = atomic number of the projectile particle
- v = velocity of the projectile particle [cm/s]
- I = average ionization potential of the target [eV]
- e = fundamental charge 1.6×10^{-19} [C]
- m_e = rest mass of the electron 9.11×10^{-31} [kg]
- k = Coulomb constant 8.99×10^{9} [Nm^{2}C^{-1}]
- $\beta = v/c$ with c = velocity of light 3×10^{8} [m/s]

The term $-dE/dx$ is referred to as stopping power, representing the average energy dissipated by ionizing radiation in a medium per unit path length of travel of the radiation through the medium.

In analogy to stopping power, another quantity commonly defined in radiobiology to estimate the dose delivered to tissues is Linear Energy Transfer (LET). It represents the linear transfer of energy from the charged particles to the matter.

If only collisions that result in an energy transfer below a certain threshold Δ (in eV) are considered, it will be called restricted LET:

$$L_\Delta = \left(\frac{dE}{dx}\right)_\Delta \tag{1.2}$$

Otherwise, if all the collisions that deposit energy along the trajectory of the particle are considered, the total Linear Energy Transfer (LET) of the particle coincides with the stopping power value. The higher the stopping power, the greater the LET of the particle, and consequently the deposited dose into the matter. In Table 1.1 the LET values of some particles at different energies can be observed.

In Figure 1.2, a direct comparison in terms of the delivered dose between protons, carbon ions (the most commonly used among light ions), and electrons is presented.

It is evident that the dose distribution for protons or light ions has a much more advantageous profile compared to photons. This profile allows for the deposition of less energy in the healthy tissues located before the tumor volume and higher energy at the Bragg peak, followed by a rapid decrease immediately after the target volume. The distinctive

Table 1.1: Table of Particles and their corresponding Energy and LET value

Particle	**Energy [MeV]**	**LET [keV μm^{-1}]**
Electrons	0.01	2.30
	0.1	0.42
	1	0.25
Protons	0.09	100
	2	16
	10	4
	250	0.4
Alfa particles	0.65	250
	1000	0.6
Carbon ions	10	170
	250	15

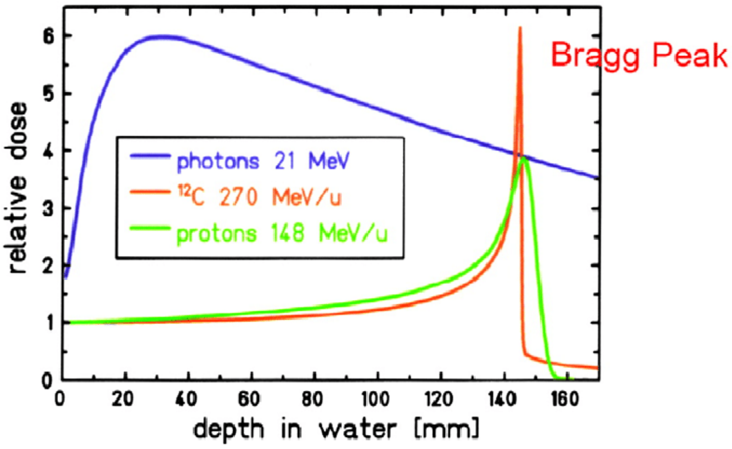

Figure 1.2: Depth dose distribution for photons and monoenergetic Bragg curves for carbon ions and protons [9].

Bragg peak profile can be exploited to maximize damage to cancerous cells within the target area while sparing the surrounding healthy tissues.

The second major advantage of the charged hadrons is that they are characterized by minimal energy and positional straggling, ensuring almost straight trajectories until complete deceleration. This feature can guarantee high ballistic precision during the treatment.

Therefore, the significant potential of proton therapy allows for excellent dose conformation even at greater depths. This means that a high dose can be delivered to the target tumor while simultaneously minimizing the dose to the healthy tissues in the proximal and distal regions.

1.2.1 Spread Out Bragg Peak

The Bragg peak generally exhibits a very narrow Full Width at Half Maximum (FWHM), which is the width of the peak at half of its maximum height. The FWHM of the Bragg peak is usually on the order of millimeters.

To deliver an adequate dose throughout the treatment, it is not sufficient to use a single Bragg peak, but it is necessary to produce what is called a Spread-Out of Bragg Peak (SOBP) with different intensities. This involves widening the Bragg peak by overlapping multiple pristine Bragg peaks at different energies resulting in a profile shown in Figure 1.3. This approach ensures that the maximum dose is not only delivered within the pristine Bragg peak but also maintained constant and distributed over a broader range of depths.

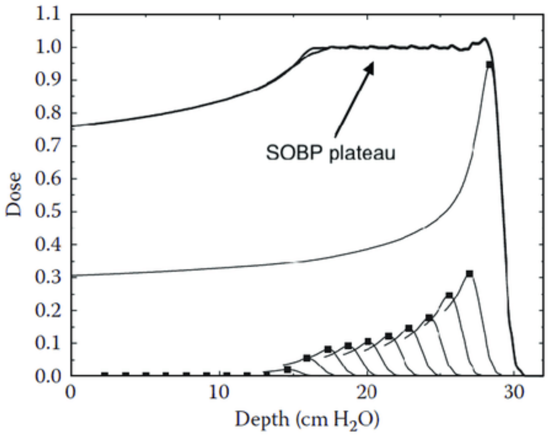

Figure 1.3: Proton SOBP in water, showing the individual Bragg curves that make up the SOBP [10].

The SOBP allows for a precise dose conformation in-depth, maintaining a uniform dose throughout the entire thickness of the target volume. The disadvantage is that the curves are summed up, including in the proximal zone of the tumor, resulting in an increased dose to the healthy tissues.

Despite this, the SOBP technique still achieves a significant dose reduction in the proximal region compared to photon irradiation, as illustrated in Figure 1.4. The SOBP does not exhibit any 'side effects' in the distal region, where the curve maintains a rapidly decreasing trend toward the end of the target volume.

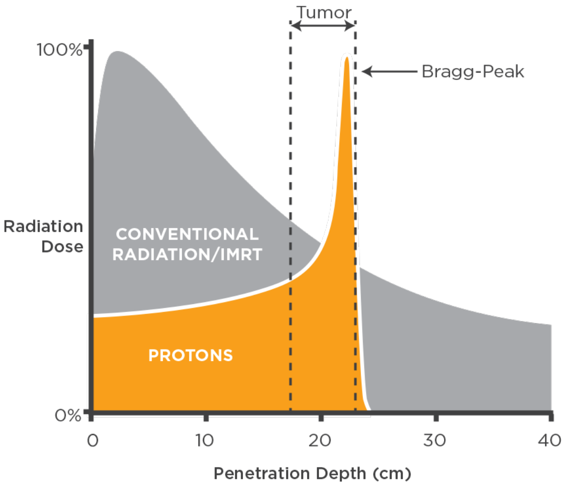

Figure 1.4: Comparison of dose profiles for proton and x-ray radiotherapy

1.3 Biological effects of radiation

Radiobiology is the science that evaluates the effects of radiation on living organisms. In addition to absorbed dose curves, it is important to observe how different types of projectile particles interact from a radiobiological standpoint with the traversed tissue cells, causing different consequences in their biological cycle. The biological effects of radiation primarily depend on the ionization and excitation of tissue molecules with which the interaction occurs.

Biological systems are highly radiosensitive. DNA, the molecule that contains the cell's genetic information, is the vulnerable part of the cell to radiation damage. DNA contains the instructions for making enzymes and proteins, which are crucial for the cell's survival. DNA has a diameter in the order of nanometres, typically ranging from 2 to 3 nm. It assumes the typical double helix structure and consists of four bases: adenine (A), guanine (G), cytosine (C), and thymine (T). DNA plays a crucial role during cell replication. Any alteration in its sequence caused by an external mutagenic agent can lead to the proliferation of cells that are different from the parent cell if the DNA reparation mechanism is not efficient enough. In the case of cancer cells, the aim is to target the DNA of these cells, causing death and interrupting uncontrolled proliferation.

1.3.1 Direct and indirect Interaction

When radiation interacts with biological tissue, it can lead to various forms of DNA damage.

The first type of damage involves alterations to the building blocks, or bases, of the DNA molecule, for which low Linear Energy Transfer (LET) radiations are mainly responsible (X-rays, electrons).

The second type of damage involves the breaking of either a single-strand or both strands of the DNA molecule, a scenario more likely induced by high LET radiations. Double-strand breaks are particularly challenging for DNA repair mechanisms and frequently result in cell death. Inducing this type of damage will be preferred to achieve effective treatment outcomes.

As mentioned above, low LET radiation primarily affects the DNA bases. This interaction mechanism is indirect: since cells consist of over 70% water, most of the energy absorbed by the cellular tissue leads to ionization and excitation of H_2 molecules, resulting in the formation of highly reactive free radicals (such as $OH-$ and O_2- ions). These radicals then attack the DNA bases in the tissue molecules. This chemical interaction between free radicals and DNA is responsible for the damage, as the radiation does not directly affect the DNA of the cells. Instead, the damage is caused by an intermediate 'agent'.

On the other hand, when single or double-strand breaks occur in the double helix, there is a direct interaction mechanism between the incident radiation and DNA. The ionization produced along the radiation track directly causes the breakage of the DNA chain in the cells encountered.

In general, direct interactions are closely related to the LET of the incident particle. Protons and, particularly, carbon ions generate more direct interactions compared to photons. Photons, with their lower LET, are more likely to interact indirectly with DNA.
Additionally, particles with higher LET lead to a higher density of ionization produced along their trajectory, making the induction of double-strand breaks in DNA chains more likely. Because of their high LET, all light ions are excellent candidates for effective radio-therapeutic treatments.

1.3.2 RBE: Relative Biological Effectiveness

The biological effects induced by radiation on the cells of a living organism do not depend solely on the LET of the incident radiation but on a complex set of factors. These factors include the administered dose, the type of particle, the type of cell affected, and the phase of the cell cycle at the time of irradiation. The effectiveness of a particular type of radiation in causing cell death is measured in relation to the effect produced on populations of irradiated cell cultures. The obtained results are illustrated through survival curves, where the logarithm of the fraction of surviving cells is plotted against the administered dose.

The initial shoulder observed primarily in low LET radiation curves indicates the cell's ability to repair, at least in an initial phase, the DNA damage caused by radiation. The subsequent linear region represents an exponential decrease in the cell population, indicating that the damage inflicted is now too extensive (e.g., multiple double-strand breaks) to be repaired by the cell itself, leading to certain cell death.

To account for all the factors that contribute to the varying effectiveness of different types of radiation, radiobiology uses a quantity called Relative Biological Effectiveness (RBE). This quantity compares the biological effect of a given type of radiation to that of standard radiation, typically X-rays or gamma rays. It provides a measure of how much more or less effective a particular type of radiation is in causing biological damage compared to standard radiation.

The RBE is defined as follows:

$$RBE = \frac{D_{\text{ref}}}{D} \tag{1.3}$$

Where D refers to the dose administered by the radiation field under investigation, which is necessary to achieve the same biological effect as the reference dose (D_{ref}) delivered by a reference field of photons (usually assumed to be 150 kV X-rays). In general, the RBE value is provided to produce a fraction of cell death equal to 90%. The greater the slope of the curve, the higher the relative biological effectiveness (RBE) of that particle.

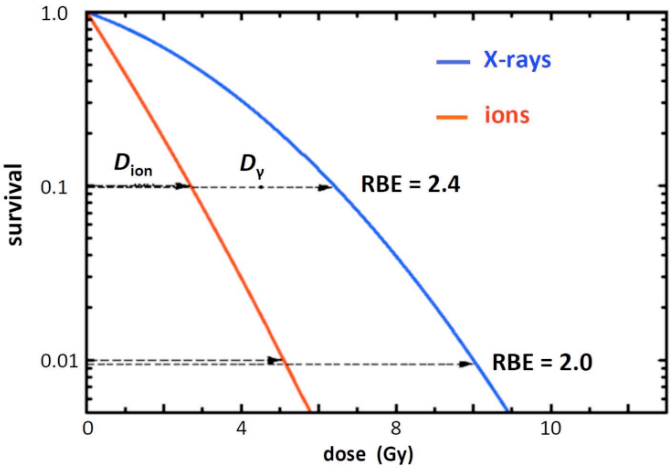

Figure 1.5: Example of calculation of two RBE values from cells irradiated with a photon beam and a carbon ion beam [11].

This implies that the particle is significantly more effective at causing cell death compared to photons. To achieve an equivalent biological effect, a lower dose is required compared to the dose delivered by the reference field. Light ions typically exhibit a relatively high RBE value within the Bragg peak (averaging around 3) and a much lower value in the proximal region of the curve (around 1). It is precisely due to this difference in RBE along the depth dose profile, that hadrons can deliver a low dose at the entrance and a much higher dose at the target volume to be treated, as it can be seen in Figure 1.6. Therefore, hadron therapy proves to be more advantageous than X-ray radiotherapy not only in terms of physical dose distribution but also in terms of biological effectiveness, as depicted in Figure 1.5.

1.3.3 OER: Oxygen Enhancement Ratio

The presence or absence of oxygen within cells during irradiation is a crucial factor to consider as it can modify their biological response. Oxygen significantly sensitizes cells to radiation: in the presence of well-oxygenated tissue, the same radiation produces much greater biological effects compared to irradiating the same tissue under hypoxic conditions. This is due to the fact that oxygen is required to generate molecules called free radicals, that, at high concentrations cause a phenomenon called oxidative stress, process that can damage cell structures [12].

To evaluate the extent of the effect due to oxygen presence, the Oxygen Enhancement Ratio (OER) is used:

$$OER = \frac{D}{D_{\text{ox}}} \tag{1.4}$$

Here, D represents the dose required to produce a specific effect in the analyzed tissue, and D_{ox} is the dose that would produce the same biological effect if the tissue were completely oxygenated in the air at normal pressure.

For Low Linear Energy Transfer radiation, such as photons, the oxygen effect is very pronounced (this can be seen in Figure 1.6.). This poses a challenge in treating hypoxic tumors, such as salivary gland tumors, as the dose typically delivered in X-ray radiotherapy sessions is no longer sufficient. A much higher dose would be required to achieve good radiobiological effectiveness, especially for radioresistant tumors.

On the other hand, for high LET particles like carbon ions and other light ions, the oxygen effect is less pronounced (OER around 1), making the dose to be administered almost independent of the amount of oxygen present in the tumor cells to be irradiated. This independence allows for the treatment of even incurable, radioresistant tumors with particle therapy, overcoming the limitations of conventional radiotherapy

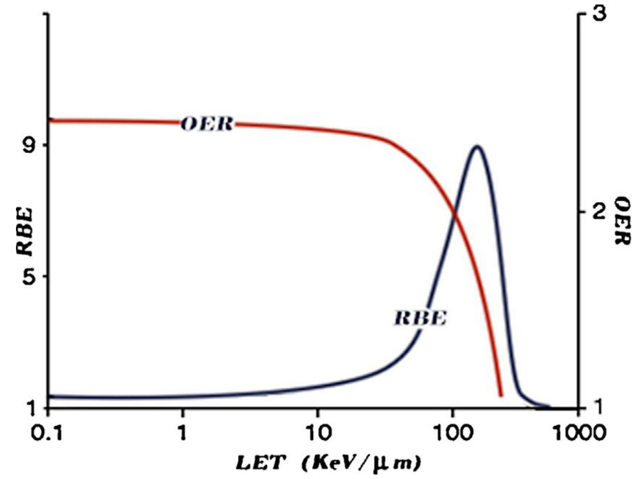

Figure 1.6: In this figure it can be seen that OER is very pronounced for low LET values, while it decreases for higher LET values. It can also be seen that for hadrons RBE delivers a low dose at the entrance, while delivering a much higher dose at the target volume.

1.4 The advantages of Hadrontherapy

In the previous paragraphs, some of the techniques used in radiotherapy were introduced. Among them, one of the most promising ones is undoubtedly hadrontherapy, which has rapidly developed and spread in recent years due to the advantages it offers over X-ray radiotherapy.

X-rays have been the standard radiation therapy for cancer treatment for a long time. However, recent scientific advancements and increasingly powerful particle accelerators have popularized the use of protons and light ions for treating specific types of tumors. A summary of the previously outlined strengths of hadron therapy will be provided to offer a comprehensive overview of this therapeutic modality.

The advantages over conventional radiotherapy are as follows:

- Selective and effective energy deposition in the planned target volume, utilizing the Bragg peak and the Spread-Out Bragg Peak (SOBP) profile. This approach allows for a relatively modest dose to be delivered to the surrounding healthy tissues, especially in the distal part of the tumor, while delivering a high dose within the target volume. The aim is to maximize the destruction of cancer cells and minimize damage to healthy tissues.
- The treatment beam remains collimated even deep within the biological tissue. This provides the opportunity to treat tumors near vital and critical organs (such as the spinal cord and the brainstem) or highly radiation-sensitive critical organs

(for example optic nerve, lens, optic chiasm, gonads etc.). Treating these types of tumors is possible with hadron therapy due to the reduced energy straggling and positional uncertainties, the high ballistic precision of ions and the ability to conform the dose to the target volume even at depth. This level of precision cannot be achieved using X-ray radiotherapy.

- Enhanced overall radiobiological effectiveness of ions (especially the carbon ions) compared to photons. This is possible thanks to two factors. The first is the varying RBE values depending on the density of ionization produced (high BRE values within the Bragg peak and low values in the proximal region of the curve). The second one is the double-strand breaks in DNA, which are more likely to occur in the former case, leading to highly probable cell death. This allows an effective destruction of the target cells with a relatively low administered dose.

  Additionally, since the effect of oxygen enhancement is significant for carbon ions and high LET particles in general, hypoxic and radioresistant tumors can also be treated effectively, overcoming the limitations of traditional therapy.

The combination of these advantages results in remarkable effectiveness in treating various types of tumors, including those in which conventional radiotherapy is not applicable or does not provide significant benefits.

It is also important to note that the clinical use of these particles, especially carbon ions, is still limited worldwide due to their young age and limited availability. This limitation arises from the fact that hadrontherapy needs to be conducted in dedicated centers. Protons and ions, being heavy particles, require powerful and large-scale accelerators to reach the necessary energies. Currently, there are 127 specialized centers worldwide that enable the treatment of tumors using hadrontherapy and a lot more under construction [13]. The peculiarity of CNAO is that, unlike other centers that are designed to accelerate a specific type of particle, together with the other 5 centers, it can accelerate not only protons but also carbon ions inside the same facility (the other centers being: *MedAustron* in Wiener Neustadt (Austria), *SPHIC* in Shanghai (China), *HIT* in Heidelberg and *MIT* in Marburg (Germany), and *HIBMC* in Hyogo (Japan)).

Chapter 2

CNAO

CNAO (Centro Nazionale di Adroterapia Oncologica) located in Pavia, has been a prominent presence in the Italian and global healthcare landscape since its clinical activities commenced in 2011.
CNAO is the only center in Italy and one of the six worldwide in which it is possible to treat patients with both protons and carbon ions.
In 2023, the number of patients treated at the center exceeded 4700, and these numbers have shown a steady increase due to continuous development, allowing for shorter treatment times and improved therapy outcomes.

2.1 History

The initial concept of establishing an Italian centre for hadrontherapy was born in May 1991, with the publication of the report "*Per un centro di teleterapia con adroni*" (For a centre of teletherapy with hadrons) authored by Ugo Amaldi and Gampiero Tosi. In 1992 the idea received its first funding from the National Institute for Nuclear Physics (INFN) to study the development of an accelerator capable of accelerating both protons and carbon ions. This project was named ATER (AdroTERapia).
In 1995, Ugo Amaldi proposed the European project for the development of a synchrotron optimized for hadron therapy, leading to the initiation of a collaborative effort, called the Proton Ion Medical Machine Study (PIMMS), which involved multiple European centers and universities. The study aimed to optimize the accelerator design and laid the foundation for the construction of the accelerator by CNAO.
In 2000, the study was successfully completed, and the Italian Ministry of Health made the decision to fund the construction of CNAO, established in 2001 with Erminio Borloni as its

president. He played a crucial role in establishing a network of national and international collaborations, which was vital to CNAO's success.

On March 5, 2005, the foundation stone was laid, symbolizing the start of the centre's construction in Pavia. The construction phase was completed in 2009 and on February 15, 2010, the centre was officially inaugurated, marking the transition from the construction phase to the experimental phase.
In this phase, which lasted approximately three tears, the centre conducted scientific research and treated a sample of several hundred patients, providing valuable data and validating the efficacy of hadrontherapy within the Italian hospital setting.

Following this successful phase, CNAO transitioned into full-scale operation, which began in late 2012 and continues to this day. The center has experienced a steady increase in the number of patients treated annually, showcasing the growing acceptance and recognition of hadrontherapy as a leading-edge treatment modality.

2.2 CNAO's high-technology complex

The CNAO complex is located in Pavia, in a strategic location that permits collaborations with the nearby hospital facilities and the scientific hub of the University of Pavia. Within the building, different functional areas can be distinguished: the outpatient area for specialized visits, the imaging and nuclear medicine department, the section dedicated to the delivery of the treatment (which includes patient preparation, immobilization rooms, and the three treatment rooms), the administrative department and the technological areas.
The heart of the center is the particle accelerator (Figure 2.1), a 25-meter diameter synchrotron that enables the treatment of patients with accelerated protons ranging in energy from 60 to 250 Mev and carbon ions ranging from 120 to 400 MeV/nucleon.

Once accelerated to the required energy, the beam is extracted and transported to one of the three treatment rooms, where it is delivered in a controlled manner to the patient who has been precisely positioned using three different position monitoring systems with millimeters accuracy. The beam is transported from the synchrotron ring to the treatment room through four branches (three horizontal and one vertical) of the high-energy transport line.

The dose administered to the patient is carefully monitored at the end of each high-energy line using the *Dose Delivery System* (DDS), which measures the number of particles delivered and the beam position in real-time. The synchrotron room and treatment rooms are located in an underground bunker to take advantage of the natural radiological barrier

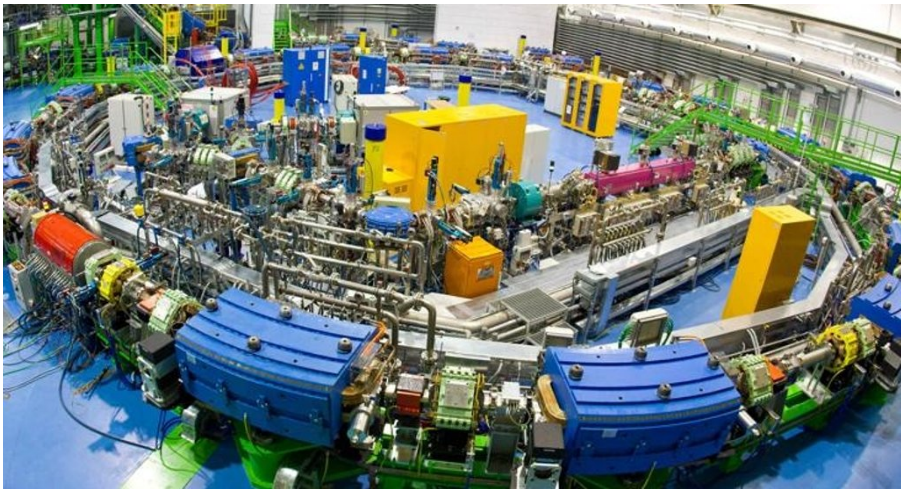

Figure 2.1: The synchrotron at CNAO

provided by the terrain, in addition to the thick cement shielding constructed around the rooms to comply with the radioprotection limits imposed by law.

2.2.1 The accelerator and the transport lines of the beam

The principal components of the machines and the transport lines that constitute CNAO's high technology are:

- Sources for the production and a first acceleration of ions
- LEBT line (Low-energy Beam Transport)
- RFQ (RadioFrequency Quadrupole)
- LINAC (LINear ACcelerator)
- MEBT line (Medium-Energy Beam Transport)
- The synchrotron ring;
- HEBT line (High-Energy Beam Transport).

The acceleration chain schematic is depicted in Figure 2.2. The initial components, from the sources to the MEBT, are situated within the synchrotron ring, ensuring a more compact layout. The beam originates from one of the two identical Electron Cyclotron Resonance (ECR) sources. By simply altering the enclosed gas, radio frequency (RF) settings, and high voltages, each source can yield various types of ions, thereby allowing for the variation of the accelerated particle type. Should one source malfunction or be absent, the other can compensate by changing the gas and the outgoing ion type. During

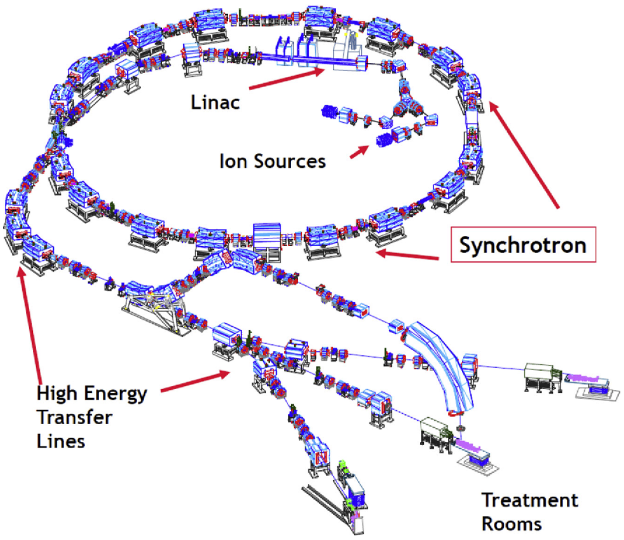

Figure 2.2: The acceleration chain schematic at CNAO

source operation, the gas contained within is heated until it reaches a plasma state. Once partially ionized, the plasma is extracted and introduced into the Low-Energy Beam Transport (LEBT). Currently, at CNAO, both a carbon ion source and a proton source are operational, aiming to generate $^{12}C^{4+}$ ions and H^{3+} ions from CO_2 and H_2, respectively.

Upon leaving the sources, the particles enter the LEBT, which is the low-energy beam transport line, connecting the sources to the Radiofrequency Quadrupole (RFQ). The LEBT's role is to spectrally separate the desired species, to select the beam portion suitable for acceleration using a chopper, and to appropriately match the incoming beam characteristics to the RFQ.
The RFQ is positioned just before the LINAC in the acceleration chain. It pre-accelerates the beam from 8 keV/nucleon to 400 keV/nucleon, preparing it for entry into the LINAC, a Radiofrequency Linear Accelerator, where particles attain energies of 7 MeV/nucleon. Within the LINAC, the most significant acceleration step before the synchrotron ring takes place. It can accelerate all incoming particles with a charge-to-mass ratio equal to $(q/A) \geq 1/3$, with q representing the ion charge and A the mass number. Downstream from this component lies the stripping foil, which removes the last remaining electrons, achieving complete ionization of beam particles (C^{6+}, ions, and protons).

At this juncture, the Medium-Energy Beam Transport (MEBT) line carries the beam to the synchrotron entrance. It also manages emittance control, adjusts optical functions, optimizes momentum dispersion, and intentionally varies the injected current intensity into the synchrotron. This is typically set at 0.7 mA for protons and 0.15 mA for carbon ions.

The primary component of the chain is a 25-meter-diameter synchrotron, a ring-shaped accelerator where particles travel along a closed circular orbit. The particles enter the synchrotron with an energy equal to that reached in the LINAC. As they cyclically traverse the ring, they undergo acceleration and are extracted directly at the desired energy, ranging from a minimum of 60 MeV for protons to a maximum of 400 MeV/nucleon for carbon ions. The electromagnetic field within the accelerator varies periodically in sync with the energy of the beam to keep the particles in their nominal orbit while they gain speed.

The extraction process is the most critical phase, as the beam intended for the treatment rooms must exhibit good characteristics of spatial and temporal distribution uniformity. The beam exits the synchrotron ring in discrete spills, each lasting about 1 second. This is achieved through a slow extraction mechanism[1]. Consequently, the particles start oscillating around the nominal orbit with increasing amplitude until they encounter the electrostatic extraction septum, which deflects their trajectory, directing them into the High-Energy Beam Transport (HEBT). The beam, which within the machine is a packet lasting less than 1 μs, is extracted by slowly pushing it in energy towards the unstable zone via the betatron core, to distribute it temporally to achieve a 1-second extracted spill.

After being extracted from the ring, the beam is transported to the treatment rooms through the HEBT, the High-Energy Beamline. One of the main components of the HEBT is the chopper, consisting of 4 fast dipoles in series, which allows the beam to be stopped when patient irradiation in the room is not required. Under normal conditions, the magnets of the chopper are turned off, and the beam impacts an obstacle (dump) designed to stop and absorb it. When the magnets are activated, the beam is deflected to avoid the obstacle and continues its path to the treatment rooms. The chopper's response time is less than 200 μs, ensuring rapid beam on-off switching with the delivery of less than 2.5% [2] of the planned dose for a treatment spot[3].

---

[1] As it will be explained in the following chapters, in the slow extraction mechanism a betatron core is used to induce an additional accelerating potential that pushes the beam within the ring towards an unstable region of the phase space created by the resonance sextupole.

[2] The prescription on the dose uniformity is $\leq 2.5\%$

[3] The dose distribution system at CNAO employs an active system with a spot scanning mechanism. In essence, the dose is administered discretely at specific points, known as *spots*.

After the chopper, the HEBT diverges into four fixed beamlines: three horizontal and one vertical. These beamlines transport the beam to the treatment rooms where it is ultimately delivered to the patient. Treatment rooms 1 and 3 are equipped solely with a horizontal beamline, whereas in treatment room 2, irradiation can be performed both horizontally and vertically. To establish the vertical irradiation line, four 22.5° magnets were employed to elevate the beam to about 6 meters above the synchrotron support plane, and finally, a large 90° magnet was used to bend the beam vertically over the patient. To direct the beam into the desired beamline, switching magnets, that enable the beam to be deflected in the desired direction, are utilized. Initially, a first switching magnet selects between the vertical line and the horizontal lines. When the magnet is activated, the beam is directed upwards along the vertical line leading to treatment room 2. When the magnet is deactivated, the beam continues horizontally to the second switching magnet. This second magnet enables the selection of the horizontal beamline for one of the three treatment rooms. If both switching magnets are inactive, the beam continues straight along its trajectory, entering the horizontal beamline of treatment room 2.

Each of the four branches of the HEBT is equipped with a safety system known as a 'beam stopper'. This device is constructed from tungsten and is responsible for halting the beam in the event that it remains active even when not required. Typically, all beam stoppers are fully inserted, effectively occupying the entire cross-section of their respective transport lines. When a beam is needed in one of the treatment rooms, the beam stopper for the selected line is lifted using a compressed air pump system. This action clears the path for the beam, allowing it to be accurately delivered to the intended room. In case of a blackout (partial or total power loss), the pump shuts off, causing the beam stopper to return to its inserted position.
Throughout the entire acceleration and transport chain through which the beam travels, a vacuum is maintained to minimize particle loss due to interactions with air molecules.

At CNAO, protons are accelerated with energies ranging from 60 MeV to 250 MeV and a maximum number of particles per spill of about 10^{10} (approximately 2 nA).
Carbon ions, on the other hand, are accelerated with energies between 120 MeV/nucleon and 400 MeV/nucleon, and each spill contains around 4×10^8 particles (approximately 0.4 nA).

The extraction energies of these particles have been designed for the clinical application of tumor treatment. The beam can cover a range of up to 27 cm in water (which closely approximates and simulates the density of biological tissue) with 1 mm steps. This configuration allows for the treatment of tumors located at greater depths as well.

A comprehensive description of additional medical and physical parameters of the beam can be found in Table 2.1.

Table 2.1: Main medical and physical beam parameters

Types of particles accelerable by design	$p, \mathrm{He}^{2+}, \mathrm{Li}^{3+}, \mathrm{Be}^{4+}, \mathrm{B}^{5+}, \mathrm{C}^{6+}, \mathrm{O}^{8+}$
Accelerated particle species	p, C^{6+}
Acceleration energies [protons]	60-250 MeV
Acceleration energies [carbon ions]	120-400 MeV/u
Beam range	from 3 g/cm^2 to 27 g/cm^2
Energy step	0.02 MeV
Bragg peak modulation step	0.1 g/cm^2
Range adjustment	0.1 g/cm^2
Modulation/adjustment accuracy	$\leq \pm$ 0.025 g/cm^2
Average dose rate	2 Gy/min
Dose administration precision	$\leq \pm$ 2.5%
Beam axis height	120 cm
Beam size	from 4 to 10 mm to the FWHM
Beam size step	1 mm to the surface of the patient
Beam size accuracy	$\leq \pm$ 0.2 mm
Beam position step	0.1 mm
Beam position accuracy	$\leq \pm$ 0.5 mm
Maximum number of particles per patient spill	10^{10} protons and 4×10^8 carbon ions
Minimum number of particles per spill	10^8 protons and 4×10^6 carbon ions
Nominal number of spills and treatment time	60 spills in 2/3 minutes

2.2.2 Dose Distribution System

Tumors treated with hadrontherapy can reach significant sizes, with lateral and deep extensions of several centimeters. On the other hand, the accelerated particle beam has much smaller dimensions, it is called pencil beam and is typically a few millimeters in diameter. Once the beam is extracted and transported to the designated treatment room it is necessary to have a system that adapts and properly distributes it to treat the entire target volume.

At CNAO, an active beam delivery system is utilized: the final part of each branch of the HEBT (High-Energy Beam Transport) is equipped with a pair of scanning magnets that deflect the charged particles in the x-y plane, orthogonal to the irradiation direction, allowing for distribution across the entire transverse section of the tumor volume. The two magnets are rotated 90 degrees relative to each other, enabling separate control of scanning along x and y directions.

Regarding depth distribution, the Spread-Out Bragg Peak (SOBP) is achieved by varying the extraction energy of the particles from the ring, ensuring that they have different ranges (depending on their energy) and deposit along the entire thickness of the tumor, resulting in the characteristic SOBP profile.

To achieve efficient irradiation, the volume to be treated is divided into isoenergic slices, and slice by slice, the pencil beam 'paints' the targeted area using the scanning magnets. Along the transport line, there is a horizontal deflection magnet followed by a vertical deflection magnet. The minimum speed at which the beam can be moved is 20 m/s.

The treatment starts from the proximal slice of the tumor, which requires the lowest energy to be reached, and progresses to the distal slice, gradually increasing the energy of the particles extracted from the accelerator. The target is irradiated using spot scanning, where the beam is discretely delivered in points within each slice. These points are defined in the treatment plan to achieve an overall uniform dose profile.

The delivery of particle therapy can happen using two different delivery systems: a passive and an active system [14].

A passive distribution system (similar to those used in conventional radiotherapy) does not dispose of magnets for the beam scanning: it employs a fixed pencil beam that is enlarged and conformed, with different techniques, to the tumor thanks to physical devices put along the beam trajectory.

On the other hand, the employment of an active system is extremely advantageous as it prevents the loss of beam quality that would occur with a passive distribution system. At the same time, it offers high precision and scanning flexibility due to the incorporation of magnets. This approach enables tailored treatment for every patient, by building a specific treatment plan for each patient, without the need for personalised systems like collimators which are indispensable in passive systems. In Figure 2.3 the difference between an active and a passive system can be seen.

To monitor the administered dose in real-time during a therapy session, the Dose Delivery System (DDS) is employed. It is situated in the terminal end of each branch of the HEBT and is composed of two independent systems to control the exiting beam characteristics (Box1 and Box2). They measure the profile of the beam, the position, and the number of particles directed to the patient.
The DDS detector system directly controls the scanning magnets, automatically guiding the beam distribution. After delivering the planned amount of particles to the current spot the DDS shifts the beam to the next spot and so on until all the spots in the same energy slice are completed. Then the extraction energy of the beam is increased, and the process proceeds to the next slice at a slightly higher energy.

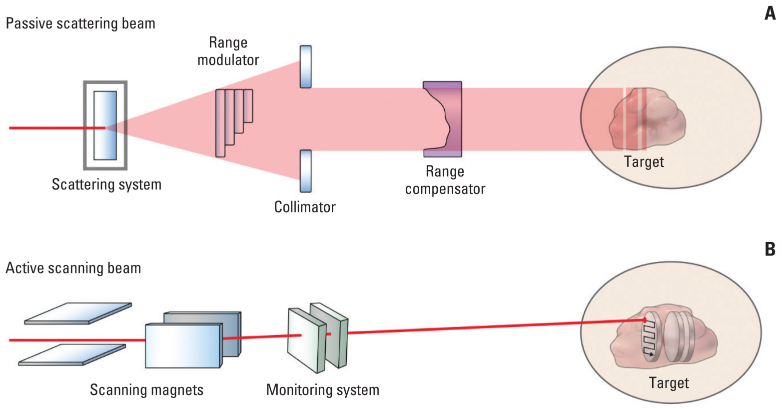

Figure 2.3: Difference between a passive and an active scanning system, A depicts a passive scanning system while B depicts an active scanning beam that includes scanning magnets and a monitoring system [14].

The beam is designed to meet specific optic and physical parameters, and the point where the nominal beam characteristics are fixed is called the treatment room isocenter [4]. The patient needs to be positioned in the treatment room so that the isocenter of the room is located inside the target volume to be irradiated.

2.2.3 Patient positioning systems

To fully harness the high precision that is achievable through the use of charged hadrons, precise patient positioning in the treatment room must be guaranteed.
At CNAO, a physical patient immobilization system and an in-room imaging system, referred to as CAPH (Computer Aided Positioning System in Hadrontherapy), are in place for patient positioning in the treatment room.

The first step involves the immobilization of the patient, a process conducted in specialized rooms and once the patient is correctly fixed to the carbon plate, he can be conducted to the treatment room to commence therapy. This is done to optimize the timing of the treatment. The patient is secured to the carbon plate thanks to a custom-fitted, rigid plastic mask. In each treatment room, the CAPH system is available. It integrates optical tracking and in-room imaging to achieve the required positioning precision. The CAPH system consists of three distinct components:

1. **PPS** (robotic pantographic Patient Positioning System): a numerically controlled mechanical arm that guides patient support in six degrees of freedom, ensuring high

---

[4] The point within the patient's body where the radiation beam is focused.

precision.

2. **PVS** (Isocentric in-room imaging system): an X-ray-based imaging system that involves four robotic arms with X-ray tubes and corresponding flat panels. They create 2D stereographic patient images, compared to CT-based Digitally Reconstructed Radiographs (DRRs) for position verification. If any discrepancies are noted, the PPS computes a correction vector for repositioning before each beam delivery.
3. **OTS** (infra-red optical tracking system): utilizing three cameras, this real-time optical tracking system monitors patient surface points, enabling precise 3D localization of markers on the mask. It compensated for organ motion during treatment due to breathing.

By combining the patient immobilization system with the CAPH technology, precise patient positioning is achieved and maintained throughout the entire treatment session. This approach allows for the accurate replication of the setup in subsequent sessions, ensuring effective therapy delivery.

2.2.4 Clinical-Therapeutic pathway at CNAO

To access hadron therapy treatment at CNAO, an initial evaluation of the clinical case is performed. This assessment is necessary to determine if the patient is eligible for this type of therapy, to only select patients with suitable characteristics. Upon a positive assessment, the process begins with an initial visit by the medical staff and a preliminary phase for the evaluation of the most appropriate treatment for the clinical scenario. The tumor's location is initially approximated by the radiation oncologist to identify the bodily region that will be the focus of the therapy. The patient is positioned on the carbon plate and a personalized immobilization device is created using a rigid thermoplastic material, heated in a 70 °C water bath to make it pliable. It is shaped directly on the patient's skin to conform to their anatomy, the material cools and hardens in a few minutes, creating a rigid mask specifically designed for the patient.

During the preparatory phase of treatment, the process continues with a series of diagnostic tests based on the requirements of the clinical case. CNAO has an imaging department equipped with the following machines:

- **CT** (Computed Tomography), which provides a sequence of images, each depicting a slice into which the volume is divided. Images can be combined to create a 3D reconstruction of the volume displaying anatomical information of the scanned portion.

- **PET/CT**, where CT is combined with positron emission tomography (PET), performed through the injection of a radio-pharmaceutical into the body. The latter allows the study of functional information, for example, allowing the identification of evolving neoplasms observing a higher proliferative activity. It is used to integrate and enhance the anatomical images from CT.
- **MRI** (Magnetic Resonance Imaging),is a diagnostic technique that utilizes a strong magnetic field and radiofrequency electromagnetic waves to excite the resonances of atomic nuclei, providing clear visibility of soft tissues and their various densities.

During the preparation phase for treatment a series of diagnostic exams are performed, these include CT scans, PET/CT scans, and MRI scans. These images help outline the patient's anatomy and permit the identification of the areas of interest. To assure an accurate positioning the patient undergoes the previous exams while being immobilized with the previously mentioned mask.

After obtaining these images, a team of medical professionals creates customized treatment plans that involve the outlining of critical organs and the setting of dose limits to ensure the patient's safety. The dose limit (also called dose constraint) is imposed in some organs to avoid exceeding toxicity risks during treatment. These organs are of two types: the ones with serial behavior, in which exceeding the constraint even at a single point within the organs leads to toxicity, and those with parallel behavior, in which toxicity is induced with a certain probability only if more than a specific fraction of the organ receives a dose exceeding the limit set by the constraint.

To visualize the treatment plan's impact, Dose-Volume Histograms (DVHs) are used, showing the relation between the absorbed dose and the volume of tissue affected.

In radiotherapy planning, alongside critical organs, the patient's skin contour and various volumes are marked on the CT scan. The target volume for radiation treatment is not the exact tumor size but includes an extended area to cover potentially cancerous cells that are not visible, including a safety margin for treatment consistency (it has to be noted that the margin should be minimized to spare healthy tissue while sufficiently encompassing the target volume).

Key definitions used in radiotherapy include:

- **GTV** (gross tumor volume): visible tumor region.
- **CTV** (clinical target volume): tissue volume containing the GTV and subclinical microscopic malignancies.

- **PTV** (planning target volume): geometric concept determining beam dimensions that account for geometric variations and uncertainties to ensure that the prescribed dose reaches the CTV.
- **Treated volume**: volume enclosed by an isodose[5] surface containing the PTV. In this region, the treatment goals must be fulfilled.
- **Irradiated volume**: the tissue volume that receives a significant dose relative to the tolerance dose of healthy tissue.

During the planning of the treatment, the organs and target areas are manually outlined on CT scans creating 3D volumes. This is done by doctors and medical physicists. Using a Treatment Planning System (TPS) software, the medical physicist designs the treatment plan by optimizing radiation fields based on organ constraints and target doses. Different parameters are defined by the TPS software, such as the type of particle (carbon ions or protons), session count, field count, beam energies, delivery positions, and particle count for each spot in each energy slice. The plan also establishes the isocenter, a reference point inside the patient that provides the coordinates for the spots to irradiate. The radiation oncologist later reviews and approves the complete plan ensuring that the proper dose was chosen and the correct distribution to each region is given.

After the plan approval, a Quality Assurance (QA) check is conducted in the treatment room. The beam and dose characteristics are measured to ensure that the parameters fall into a specific tolerance range. If QA is successful, the patient can begin the treatment cycle.

At the start of each session, the patient is positioned and immobilized on the carbon plate with their personalized mask, the plate is attached to the main support in the treatment room. The alignment is achieved using the CAPH systems as described before. The planned isocenter from the TPS must be aligned as closely as possible with the room isocenter, ensuring that the actual radiation delivery matches the plan. The beam is requested for the desired treatment room and as soon as it becomes available the delivery of the first treatment begins, lasting only a few minutes, the treatment is then repeated for each field of the treatment plan. All the previously mentioned steps: alignment, position verification, and beam delivery, take up to 45 minutes in total.

The total treatment can last up to a month or more and therefore the anatomical evolutions of the patient must be monitored during this temporal arch. The patient could be

---

[5] An isodose refers to a line connecting points that receive the same dose of radiation during medical treatment. It helps visualize the distribution of radiation within the treated area.

subjected to remarkable weight changes and the tumoral mass could also change significantly. Therefore, a follow-up CT scan, called reassessment CT, is performed on average every 2 to 3 weeks. Exceptions include more urgent situations where visible anatomical changes occur that are noticeable even without imaging.

During the follow-up CT scan, new contours of organs and targets are drawn, and the parameters of the initial treatment plan are recalculated on the new CT. If the parameters remain within acceptable ranges (called tolerance ranges[6]), the treatment continues with the existing plan, if not, a new treatment plan is developed. In situations in which a dose boost is needed a short sequence of additional treatment sessions, called boost, is administered to critical tumor regions. The boost can be done with the same particle as the main treatment or a different particle type, and those sessions are strategically integrated into the overall treatment plan.

After the completion of the treatment cycle, the patient continues to be monitored with both short-term and long-term follow-ups. This ongoing observation contributes to building a clinical database containing treatment cases and statistics but also aids in gradually standardizing the treatment procedure.

---

[6] For the planned target volume, an acceptable coverage is typically achieved when the delivered dose falls between 95% and 107% of the desired dose. However, for organs at risk, the tolerance range is determined based on their associated constraints.

Chapter 3

Dose verification systems in hadrontherapy

In particle therapy, large safety margins around the tumor are employed. However, this approach may not be optimal for the patient and could potentially compromise the beneficial effects of charged particle therapy.

In this chapter, the key issues related to patient dose monitoring in the context of proton therapy and the potential solutions for enhancing dose distribution verification will be explored. Additionally, an analysis of a specific tool designed for this purpose, the PRR (Proton Range Radiograph) will be provided.

3.1 Range

In Chapter 1, the Bethe-Bloch equation was introduced as a model for describing the energy deposition of charged particles in a medium, excluding nuclear interactions. This approximation suggests that a beam of charged particles passing through a medium doesn't attenuate until the particles have completely spent their energy and come to a stop, causing the beam intensity to decline to zero. The range of a charged particle represents the maximum depth it can reach within the medium.

However, for stochastic phenomena like nuclear scattering, the depth reached varies among particles, leading to fluctuations and challenges in the determination of the range. Nevertheless, utilizing the Bethe-Bloch equation, a theoretical definition of range can be established with disregard to stochastic energy deposition effects.

This theoretical range can be defined as:

$$R = \int_0^R dx = -\int_0^R \frac{dE}{\frac{dE}{dx}} = \int_0^{E_{max}} \frac{dE}{\frac{dE}{dx}} \tag{3.1}$$

Where R is the range of the particle, while E_{max} is the initial energy of the particle. Therefore a residual energy equal to zero corresponds to a depth equal to the range, while the maximum energy corresponds to a depth equal to zero.
Recalling the Bethe-Bloch equation (Equation 1.1):

$$-\frac{dE}{dx} = k^2 \cdot NZ \cdot \frac{4\pi \mathrm{e}^4 \mathrm{z}^2}{\mathrm{m_e v}^2} \cdot \left(\ln \frac{2m_e \mathrm{v}^2}{I} - \ln(1-\beta^2) - \beta^2 \right) \tag{3.2}$$

The whole term in brackets can be written as $B(v)$ and the range can be written in the following way:

$$R = \frac{m_0}{NZ4\pi e^4 z^2} \cdot \int_0^{E_0} -\frac{v^2}{B(v)} dE \tag{3.3}$$

Equation 3.3 represents the Continuous Slowing Down Approximation (CSDA) a method that allows range calculation by simplifying the process by disregarding the statistical fluctuations typical of the discrete nature of energy deposition, commonly associated with charged particles.

3.2 Uncertainties in dose distribution

As discussed in previous chapters, hadrontherapy enables more precise and efficient dose distribution to patients, presenting the peculiar Bragg peak, which indicates that most of the energy is deposited when the charged hadrons are about to stop inside the tissue.

Charged hadrons, as they propagate through a medium, tend to follow a nearly straight path until they come to a complete stop, and they are known for exhibiting minimal straggling both in position and energy.

In physics, straggling refers to a slight variation or spread in the distances traveled by particles that started with the same amount of energy. This variation occurs because the particles lose energy in discrete steps, leading to a natural statistical fluctuation around an average. Therefore straggling is just the natural variation in how far the particles can travel in the medium before they stop due to complete energy loss. The higher the particle mass, the lower the straggling effect, meaning that heavy ions are subjected to less straggling, resulting in a sharper decrease of the curve.

The precision of this distribution implies that even minor errors during delivery could cause an imbalance in dose distribution. Charged particle therapy is highly sensitive to anatomical variations, requiring more advanced verification systems compared to those used in X-ray or photon radiotherapy.

Errors in the dose delivery phase stem from different sources of uncertainty, ranging from physical factors to potential issues that can arise during the patient's positioning. These uncertainties are generally considered in the treatment planning process by applying margins leading to the concept of the Planning Target Volume (PTV) [15].

3.2.1 Sources of uncertainty

The main sources of uncertainty, that can lead to an incorrect dose administration to the patient are listed below.

Delivery system

These uncertainties arise from errors in beam positioning or fluctuations in intensity during its extraction. It is therefore common practice to set a threshold for which intervening will be necessary, in cases of spatial fluctuations in the extracted beam. The sources of uncertainty linked to the delivery system may include the imprecise knowledge of the isocenter's position when using a gantry[1] configuration, and uncertainties arising from beam modeling blocks when the beam modeling system is of passive nature.

Beam model

The beam exiting the accelerator has a finite spatial dimension, therefore when the beam is directed into a heterogeneous medium (for example a patient's body), different portions of the beam pass through different materials. This leads to a different range, for different particles, within the same beam. In addition to that, the dose calculation algorithm used to define the treatment plan assumes that the cross-sectional dimensions of the beam remain constant.
When using carbon ions, it is very challenging to have algorithms that account for the many fragments produced, and these fragments, depositing dose mainly after the Bragg

---

[1] The gantry supports the radiation source and rotates around the patient to direct the beam at different angles.

peak, introduce additional uncertainty.
The required accuracy for dose distribution in a patient must be kept below $\leq 2.5\%$ of the total dose, although it is recommended to aim for less than 2% [16].

Hounsfield unit and range correlation

In general, the results of a CT scan are represented using a parameter known as the CT number or Hounsfield unit, which was named after Sir Godfrey Hounsfield. A Hounsfield unit is defined as:

$$HU = 1000 \cdot \frac{\mu - \mu_{air}}{\mu_{water} - \mu_{air}} \tag{3.4}$$

Where:

- μ represents the photon's linear attenuation coefficient in the medium.
- μ_{air} represents the linear attenuation coefficient of the photons in air.
- μ_{water} represents the linear attenuation coefficient of the photons in water.

Combining these coefficients together, a map that represents the CT image is obtained, and the CT images will be used to define the treatment plan. However, a source of uncertainty arises from the fact that it would not be accurate to use the CT number (based on photon attenuation) to represent the interaction of charged hadrons (better represented by stopping power).
When constructing a correlation curve between the CT number (based on which the treatment plan's range and therefore the beam energy is adjusted) and the actual range of hadrons, it is observed that the conversion is not exactly linear and is characterized by a change in slope at high CT numbers. Differences have been documented between the CT range (predicted from the CT image) and the range measured, ranging from 5% (for low HU values) to 11% (for high HU values) [17].

Target Identification

During the definition of the treatment plan, it is necessary to delineate the target. As mentioned in Section 2.2.4, the Gross tumor Volume (GTV) is delineated starting from CT, MR, and PET imaging. Following this, the other target volumes need to be identified. Understandably, there is a degree of arbitrariness in defining the target volume. To try to standardize this procedure, new 3D diagnostic techniques such as CT+PET and

PET+MRI [2] are significant.

Organ Movement

Respiration, heartbeat, and the functioning of the digestive system can lead to significant movements and displacements of internal organs. In many types of cancer treatments involving hadron therapy, it is essential to correct these movements to prevent unintentional organ shifts during radiation, which could lead to delivering the dose to healthy tissues rather than the tumor.
Various techniques are available to address this issue, and in many cases, these techniques can be combined:

- *Multipainting*: every point in the target is hit many more times than usual, reducing the individual dose deposited. This permits to statistically average any potential error.
- *Gating*: the respiratory cycle of the patient is monitored and irradiation occurs only during the exhalation or inhalation phase.
- *Gating + TAC 4D*: an innovative technique involving the acquisition of computed tomographies during both inhalation and exhalation phases to obtain a 4D map (3D in space plus the temporal dimension) of the lesion's position for treatment. This allows for precise treatment gating, by monitoring the actual internal tumor position.

Figure 3.1: In this image an example of motion compensation and its effects can be seen. If the motion is not compensated the outlines appear unclear, while the compensated case leads to defined outlines, like in the static case.

Active scanning of the beam yields better results when motion correction is applied (Figure 3.1). In this scenario, real-time adjustments of the beam during its delivery become possible.

---

[2] CT+PET stands for Computed Tomography (CT) combined with Positron Emission Tomography (PET), while PET+MRI stands for Positron Emission Tomography (PET) combined with Magnetic Resonance Imaging (MRI).

3.3 Techniques for patient dose verification

To overcome some of the previously mentioned uncertainties and enhance the verification of the administered dose, different techniques are currently being studied. These studies aim to provide insights into the patient's actual morphology and the treated volume, offering real-time feedback to ensure that the delivered dose aligns with the expected one.

The two main types of techniques are:

- Secondary-radiation imaging.
- Ion-based imaging.

3.3.1 Secondary-radiation imaging

Firstly, primary radiation is the radiation that impacts on the patient, while secondary radiation is created when the primary beam interacts with the matter.
Secondary radiation utilizes radioactive ions, injected into the patient, to perform a PET similar to the one performed in diagnostics. The most exploited method belonging to this technique is the *In-beam PET*.

In the diagnostic PET, a radio-pharmaceutical (^{18}F-FDG, composed of unstable nuclei of ^{18}F) is injected inside the patient and will be subject to β^+ decay, emitting a positron and a neutrino. The positron will annihilate with electrons in the matter and produce two anti-parallel 511 keV photons, as can be seen in Figure 3.2.

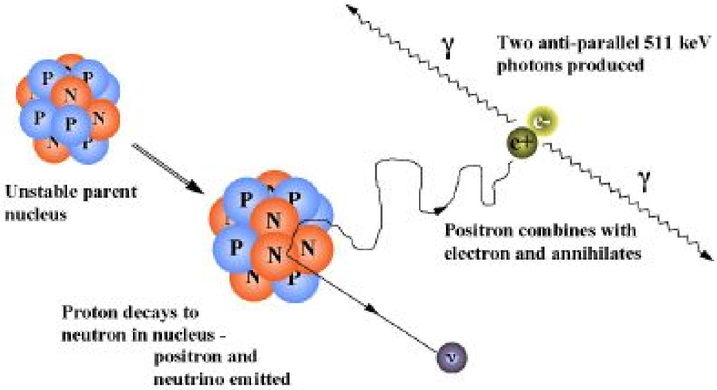

Figure 3.2: Positron emission and annihilation, starting from an unstable parent nucleus and leading to the creation of two anti-parallel photons [18].

In In-beam Positron Emission Tomography (PET), the production of β^+ particles occurs through the activation of the surrounding material via inelastic scattering with the particles in the beam.

Alternative imaging strategies are needed because of the presence of two significant drawbacks in this imaging method:

- Low coincidence events resulting in poor signal.
- Low decay time of the emitters requiring little time between radiation and measurement.

3.3.2 Ion-based imaging

The main idea behind ion-based imaging revolves around utilizing the same particle source employed during treatment.
To be effective, ions must cross the medium entirely while maintaining sufficient energy to generate a radiographic image of the patient. This image will be derived from the residual range of the particles that crossed the patient, necessitating beam energies significantly higher than those employed for treatment.

As of now, research has focused on imaging based on ions, yet there is a growing interest in heavier ions such as carbon, helium, and neon. It is however necessary to acknowledge that, implementing this imaging technique for heavier ions demands the availability of extremely high beam energies, a requirement that may not always align with the capabilities of pre-existing machinery.

Ion-base imaging: Rinaldi et al

An example of ion-based imaging can be found at the Heidelberg Ion Beam Therapy (HIT) center, based on the work carried out by Rinaldi et al. [19]. A stack of 61 ionization chambers has been assembled to create a prototype detector system, to investigate its applicability to ion-based imaging. The results of the previously cited work support the potential to use it as an efficient set-up to perform heavy ion radiography and tomography at HIT [19]. The sketch of the experimental set-up, including the 61 ionization chamber stack and the read-out electronics for the range evaluation, can be seen in Figure 3.3. The primary objectives of the work were two. Firstly to establish the relationship between the energy of the beam and the position of the Bragg peak. Secondly, to relate the detected peak position to the thickness of the physical target. For the last one, Polymethyl Metacrylate (PMMA) stacks were placed in between the IC, to add a difference in terms of the path the particles had to travel. This system possesses the capability to capture

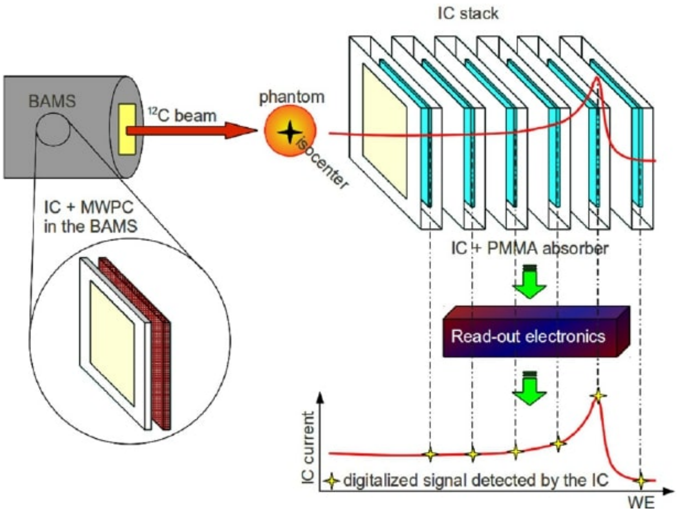

Figure 3.3: View of the IC stack crossed by the beam and the read-out electronics for the range evaluation, the yellow stars on the Bragg curve show the digitized signal detected by the IC stack [19].

signals emanating from a scanned area measuring 100×100 mm^2, with a 1 mm step, within a 2-second interval. The system is capable of providing sufficient signal by administering a dose (to the patient) of 0.4 mGy for each scanned beam position [19].

Ion-based imaging: Telsemeyer et al

A second example is the experiment conducted by Telsemeyer et al. [20] at the HIT center. This experiment is similar to the previous one, but instead of using the IC stack, a commercial Si (silicon) panel (typically used with X-rays) was employed. Information about the traversed object was obtained through measurements at different energies. A schematic drawing of this experiment can be seen in Figure 3.4.

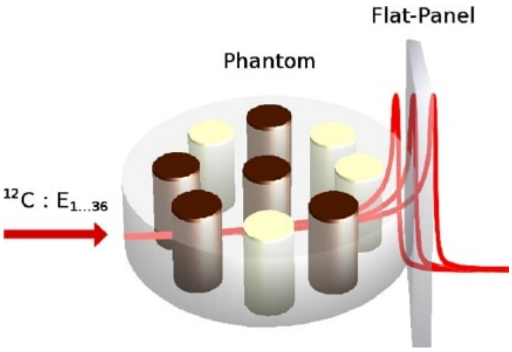

Figure 3.4: Schematic drawing of the detector, which is placed behind the imaging object and irradiated with ions of several energies [20].

The range of ions in water can be accurately estimated after applying an empirical correction parameter. It exhibits similar issues related to dose and duration as described in the previous system

Ion-based imaging: Parodi et al

The third example is the setups developed at NIRS (National Institute of Radiological Sciences) institute in Japan [21].

The first system (Figure 3.5, a) gathers information about the range by analyzing the acquired signal for five different thicknesses of the range shifter for each radiographic projection.
The second system (Figure 3.5, b) records the individual residual energy of the single ion in combination with the position before and after the target (PSD in the figure) only when there is a signal coincidence between the two scintillators placed before and after the target (this is done to exclude energy deposition from fragments).

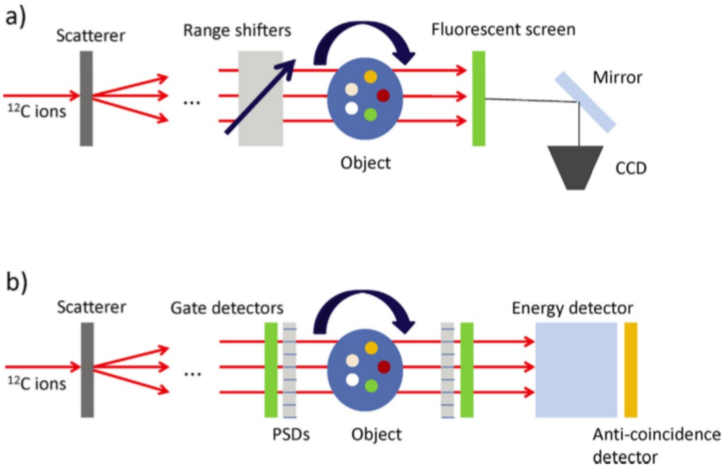

Figure 3.5: Schematic drawing of the experiment conducted at NIRS, [21].

Referring to a) in Figure 3.5, it possesses a spatial resolution in the order of 2 mm and a relative electronic density resolution better than 0.07 compared to that of water. However, it necessitates measurements with various range shifter thicknesses, which results in a requirement for up to 8 Gy of absorbed dose and a measurement duration of around one hour, both of which are clinically unacceptable.
b) in Figure 3.5, generates tomographic images with a spatial resolution on the order of 1 mm. However, this system can be quite expensive when extensive coverage areas are required.

3.4 Proton Range Radiograph (PRR)

In this section, the Proton Range Radiograph (PRR) will be analyzed and described in more detail. The PRR is an instrument designed to address issues such as the challenge of the range-CT number conversion. This instrument was developed during the Advanced Quality Assurance (AQUA) project (TERA).

This instrument can also be used for:

- *Patient Positioning*: the use of proton radiography can be considered instead of X-ray radiography for patient positioning. This approach could minimize the radiation dose to the patient because the high-energy protons used would deposit less dose compared to stereoscopic X-ray radiography
- *Treatment Pan Verification*: being able to detect protons, the PRR could be employed to verify a treatment plan before administering it to the patient.

3.4.1 Working Principle

The fundamental concept behind the Proton Range Radiograph involves measuring the coincidence of the residual range and the position of a monoenergetic proton beam after it has passed through the target, for which a radiograph is desired. When considering a proton with an initial energy E_0 directed at a target, one can evaluate the energy it will lose while traversing the target (ΔE as follows:

$$\Delta E = E - E_0 = \int_0^L \left(\frac{dE}{dx}\right)_l dl = \int_0^L \rho(l) S(l, E_l)\, dl \tag{3.5}$$

Where L is the length of the traversed medium, $(dE/dx)_l$ is the linear stopping power referred to the traversed medium, $\rho(l)$ is the density of the medium, and $S(l, E_l)$ is the mass stopping power. By measuring the residual range and knowing that the stopping power depends on the electronic density, it is possible to reconstruct the energy loss that occurred in the target, and therefore its density.

3.4.2 The Detector

The detector has an effective area of $10x10cm^2$, divided into 10^4 pixels, each measuring $1mm^2$. The structure of the PRR is composed by two Gas Electron Multiplier (GEM) designed for the reconstruction of the particle trajectory. This setup is followed by a series of 30 plastic scintillators, each 3 mm thick, employed for range verification.

The detectors are composed of three cascaded GEM foils with $400\mu m$ thick x and y readout strips. Strips of this thickness ensure a high event readout rate. The GEM cameras operate under a continuous flux of a mixture of Ar and CO_2 and use voltages ranging from 3.9 to 4.2 kV. Electronics include a commercial 128-channel pre-amplifier.

Each scintillator is optically coupled with a wavelength shifter and a Multi-Pixel Photon Counter (MPPC), followed by an 80 ns pulse shaping pre-amplification system. Data acquisition is performed through a programmable FPGA (Field Programmable Gate Arrays) board. Voltage adjustments are made to ensure consistent responses across modules, compensating for variations in thickness and optical coupling.

The GEMs and scintillators work well up to radiation fluxes of $10^4 mm^{-2} s^{-1}$. However, the current electronics is limited to 10 kHz. To handle higher particle rates, a revision of the electronics is required.

When a particle coincidentally passes through the first two scintillators, it triggers range acquisition by the others. Energies deposited in each scintillator are saved and linked to an event number. The event's position is read from the two GEMs and associated with the event number, facilitating radiograph reconstruction.

Chapter 4

Principles of Optics

In this chapter, the fundamental principles of optics will be discussed delving into the core concepts of lenses and optical systems. Lens approximations and the essential parameters that define the behavior of optical systems will be explored.

4.1 Lens approximations and equations

The optical characteristics of most systems can be analyzed by employing a limited set of parameters, and by using simplifying assumptions.
In this work, two main approximations are employed: the paraxial approximation and the thin lens approximation.

The paraxial approximation considers only rays that enter the system at small angles relative to the optical axis, allowing for easier mathematical calculations and providing a reasonable approximation for most optical systems.

On the other hand, the thin lens approximation states that a lens is considered to be thin if its thickness **t** is much less than the radii of curvature of both surfaces. An important characteristic of thin lenses is that light rays pass through the center of the lens undeviated.

If the object and image spaces are situated within the same medium (e.g., air), the following fundamental equation can be applied:

$$\frac{1}{s'} + \frac{1}{s} = \frac{1}{f} \tag{4.1}$$

In this equation, s stands for the position of the object with respect to the lens, while s' denotes the position of the image with respect to the lens, and f is the focal length of the system.
These parameters can also be seen represented in Figure 4.1.

The distance between the object and the front lens is known as the working distance (or focus distance d_0), while the distance between the rear lens and the sensor is called the back focal distance.

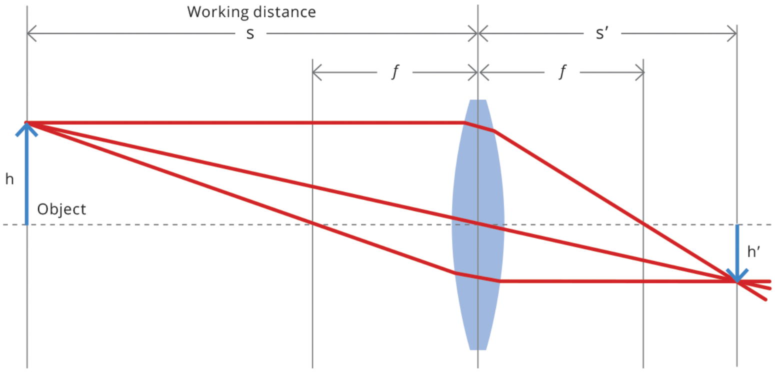

Figure 4.1: Basic parameters of an optical system. The dimension of the framed object is represented by h and h' is the dimension of the framed object when projected on the sensor.

4.2 Optical Systems

In the following sections, the basic parameters of optical systems will be discussed.

4.2.1 Focal Lengths, Apertures and F/ Numbers

Any optical system can be described by a few basic numbers.

The **aperture** is the main lens or mirror that gathers the light to a focus. The aperture diameter (D) is commonly measured in inches or millimeters. The larger the aperture, the more light the system gathers, meaning that the finer details can be seen.

The **focal length** is the distance between the center of the aperture and the point in space where distant light rays converge or appear to converge to a single point. It measures how the system refracts and focuses light.
When a lens brings parallel rays together at a physical point it is referred to as a positive (convex) lens and on the other hand, a negative (concave) lens causes parallel rays to diverge, in this case the focus point is virtual. In machine vision applications, the optics employed are typically positive lenses that direct incoming light onto the sensor plane.

The **F/ number** is a measure of the speed and clarity of the optical system. It is the ratio of the focal distance to the aperture size. In photography these are also called F-stops.

$$F/ = \frac{f}{D} \tag{4.2}$$

The smaller the F/ number, the larger the aperture, allowing more light to pass resulting in a brighter image. Conversely, higher F/ numbers indicate a smaller aperture, restricting the amount of light that enters the camera, leading to a darker image.

4.2.2 Magnification ratio

The magnification ratio is often denoted as **M** and is a measure of how much larger or smaller an object appears compared to its actual size.

$$M = \frac{\text{size of the image}}{\text{size of the object}} = \frac{h}{h'} \tag{4.3}$$

Given M, a relationship can be defined between the working distance (s), the magnification ratio (M), and the focal length (f) of the system:

$$s = \frac{f(M-1)}{M} \tag{4.4}$$

Fixed focal lenses, as used in this work, are designed to image objects that are located at a distance much greater than their focal length. This configuration is known as infinite conjugates. Classifying these lenses by their magnification is convenient for selecting an appropriate lens based on the sensor and object size.

Classifying lenses by their focal length is useful for the selection of lenses in the case of infinite conjugates. The previous equation can be used to calculate the required focal length based on the desired magnification and working distance or to determine the necessary working distance given parameters such as sensor size, field of view, and focal length.

4.2.3 Angular field of view and Field of view

The Field of View (FOV) refers to the extent of the observable region that is captured by an optical system. It represents the angular size of the area that is visible through the lens. The FOV can be defined starting from the Angular Field of View (AFOV), or viewing angle (α), which can be written in the following way:

$$\alpha = 2\arctan\left(\frac{h}{2f}\right) \tag{4.5}$$

Where f is the focal length and h is either the vertical or horizontal dimension of the sensor. The AFOV is commonly specified as the full angle (in degrees) corresponding to the horizontal dimension (width) of the sensor that the lens is used with.

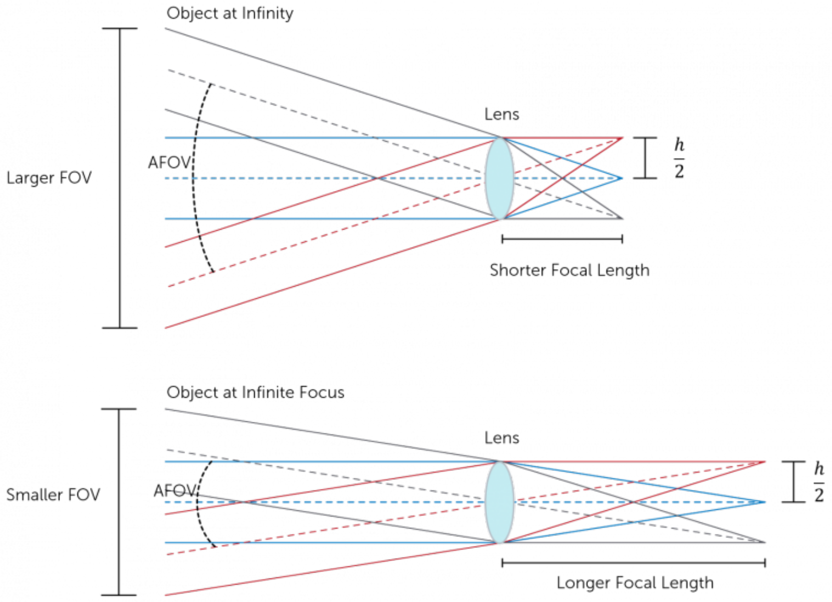

Figure 4.2: Schematic depicting how focal length has an impact on the angular field of view (AFOV).

The FOV is influenced by various factors, including the focal length of the lens (f), the size of the image sensor (h), and the distance between the lens and the object (d_0). The relationship can be expressed as:

$$FOV = d_0 \frac{h}{f} \tag{4.6}$$

From this, it can be deduced that a shorter focal length results in a wider AFOV, while a longer focal length leads to a narrower AFOV. This relationship is illustrated in Figure 4.2.

4.2.4 Depth of field

The depth of field (DoF) refers to the range of distances along the optical axis over which objects appear acceptably sharp in an image. It is determined by a combination of the values of the lens aperture, focal length, circle of confusion (see 4.2.5), and the distance between lens and subject (focus distance).

If an object is placed in front of a lens at a distance d_0 and is brought into focus, the DoF will extend from a distance d_p, which is called the near limit of DoF, to a distance d_d, which is called the far limit of DoF, from the lens.

It is possible to define the DoF value according to the rules of geometric optics:

$$d_p = \frac{d_0 \cdot f^2}{f^2 + F \cdot c \cdot (d_0 - f)} \tag{4.7}$$

$$d_d = \frac{d_0 \cdot f^2}{f^2 - F \cdot c \cdot (d_0 - f)} \tag{4.8}$$

Where:

- F is the diaphragm aperture, defined as the ratio between the focal length f and the diameter through which the light enters;
- C is the circle of confusion;
- f is the lens focal length;
- d_0 is the focus distance.

The DoF is affected by the aperture. A wider aperture (lower F/ number) creates a shallow depth of field, where only a specific part of the image appears in focus, while the rest appears blurred. A narrower aperture (higher F/ number) increases the depth of field, resulting in more of the image being in focus.

4.2.5 Circle of confusion

When a point-like object is positioned outside the depth of field (DoF), it results in a blurred image on the camera's sensor. Instead of appearing as a sharp point, the object is enlarged and forms a disk-like shape, the diameter of which is referred to as the circle of confusion (c). The specific value of the circle of confusion depends on the object's position in relation to the focal plane. At the focal plane itself, the circle of confusion has a value of zero, and as the object moves away from the focal plane, its size increases.

In practical terms, all imaging systems tolerate a certain non-zero circle of confusion. This implies that a specific diameter of c is permissible without noticeably degrading image quality. The diameter of c plays a crucial role in determining the resolution and definition of the resulting image.

4.2.6 Focal length

The focal length of a lens significantly influences both magnification and the depth of field (DoF) in an image. A shorter focal length, commonly associated with wide-angle lenses, facilitates a wider field of view and a larger DoF. This means that a greater range of distances in the scene will appear in focus.

Conversely, longer focal lengths result in narrower angles of view and a shallower DoF. With longer focal lengths, only a narrow range of distances will be in focus.

Additionally, the aperture setting plays a role in determining the DoF. Wider apertures (lower F-numbers) create a shallower DoF, while narrower apertures (higher F-numbers) produce a deeper DoF. In summary, the focal length directly influences both magnification and the depth of field in an image

4.2.7 Sensor size

The size of a sensor plays a crucial role in determining the DoF capture in an image. As the sensor size increases, the depth of field decreases for a given aperture.
This phenomenon is known as the equivalent focal length: when a lens of a certain focal length is used on a smaller sensor the resulting image appears closer, however, the image is cropped because the smaller sensor captures only a portion of the scene that would be otherwise captured by a full-frame sensor.

This phenomenon can be understood by considering the crop factor, which is the ratio between the diagonal of a full-frame sensor (typically 24x36 mm) and the diagonal of the sensor under consideration. The crop factor indicated how much smaller the sensor is in relation to a full-frame sensor.

Chapter 5

He-Check: Feasibility study

In this chapter, the work and results previously presented by Mazzucconi et al. [22], by Landini et al. [23], and Cantù et al. [24] will be discussed.

5.1 He-check system concept

The techniques relying on charged particles employ the same particle both for treatment and range verification. This implies that the treatment needs to be temporarily interrupted to be able to perform dose verification, as the latter requires a higher energy to traverse the patient. The He-check system is designed to address this challenge, by enabling simultaneous treatment and dose verification.

The underlying concept of this work is based on the possibility of accelerating carbon ions (C^{6+}) together with helium ions (He^{2+}), given that they share the same magnetic rigidity[1], meaning that the particles have the same energy per nucleon.

In this way, a mixed beam that can exploit the difference in the range of the two particles can be obtained. By leveraging these two concepts - same magnetic rigidity, and different range - it is possible to think about a system in which a beam, composed of helium and carbon ions, is administered to the patient.

As mentioned before, the possibility of extracting both ions simultaneously relies on the fact that, at the same momentum per nucleon, they have very similar magnetic

---

[1] Magnetic Rigidity R=Bρ=pc/q is the measure of the momentum of the particle (B is the magnetic field, ρ is the gyro radius, p is the particles momentum, c is the speed of light, and q its charge). A particle with a higher momentum will have a higher resistance to deflection caused by a magnetic field.

rigidity. $^{12}C^{6+}$ has a rest mass-to-charge ratio of 12/6 a.m.u., while $^{4}He^{2+}$ has a ratio of 4.0026033/2 a.m.u. (atomic mass unit).

The small difference in these two ratios is due to the fact that the rest mass of the helium is not exactly 4 a.m.u. because of the different binding energy of the two nuclei. As a result, they have slightly different momentum distributions and orbit radii in the accelerator, and due to the configuration of the extraction phase at CNAO, they will have slightly different slow extraction timings.

This means that in the initial phase, only helium ions will be extracted, while in the final phase, only carbon ions will be extracted. This issue can be resolved by discarding the initial and final portions of the extracted beam, retaining only the central portion where both ions will be present.

Once the particles are extracted with the same value of energy per nucleon, they will be sent to the patient. The range of a particle will be calculated with the Bethe-Bloch equation (Equation 1.1) and under the assumption of the Continuous Slowing Down Approximation (CSDA). Considering the CSDA means that the statistical fluctuation of energy losses will be neglected, and assuming that the slowing down in the medium occurs continuously along the projectile's track, and not discretely as it happens.

Considering two particles, a and b, with atomic numbers z_a and z_b, both having the same energy per nucleon and traversing the same medium, the range of one of the two particles as a function of the other can be calculated using the Continuous Slowing Down Approximation (CSDA), as follows:

$$R_a(v) = \frac{m_a \cdot (z_a)^2}{m_b \cdot (z_b)^2} \cdot R_b(v) \tag{5.1}$$

If a is a helium particle and b is a carbon particle, the ratio between the product of masses (m_a and m_b) and the atomic numbers (z_a and z_b) will be equal to 3 as the carbon is three times heavier and has three times the charge of the helium.

In this way, by exploiting the same magnetic rigidity and the different ranges of the two particles, it could be possible to develop a system in which the patients are irradiated by the two particles to perform both treatment and dose verification simultaneously.

Having three times the range of the carbon ions, the helium ions will be able to traverse the patient, and their range could be measured to reconstruct both the density and thickness of the crossed medium. At the same time, through the carbon ions, the correct dose will be distributed to the tumor.

At CNAO, it is not yet possible to accelerate helium ions. Therefore, to study the detector's response, protons are currently being used. The $\frac{Z^2}{A}$ ratio of protons is the same as that of helium ions. In a first approximation, a proton with a certain energy has the same range as a helium ion with the same energy per nucleon. This ratio provides a simplified way to compare the stopping power of different particles in a medium and offers a reasonable estimate of the behavior of particles with similar charge and mass in a given medium.

Using the SRIM software to evaluate the range of carbon and helium particles in water, and noting that the range of helium particles in water is almost the same as the proton range (particles that will be effectively used during the study of the He-check), it is possible to evaluate the expected range of the particles given a certain energy. For example, a beam of carbon ions with an energy of 350 MeV/u has a range in water of 22 cm, while a beam of helium at the same energy per nucleon has a range of 66 cm (as illustrated in Figure 5.1).

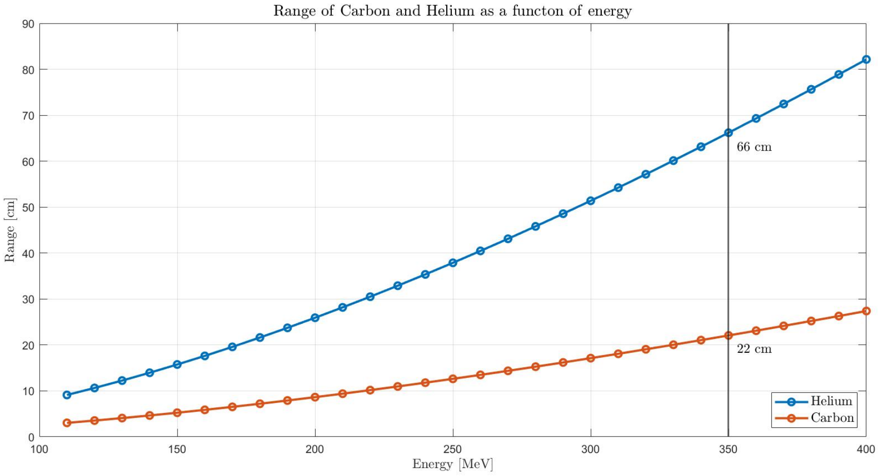

Figure 5.1: Range of Carbon and Helium particles as a function of energy. The data is obtained from SRIM software. The different Range of the particles at energy 350 MeV is highlighted.

An illustration of the system under consideration is provided in Figure 5.2. In this visualization, it can be observed how carbon deposits dose into the tumor, while helium is utilized as a probe to measure the differences in the crossed medium.

The amount of helium must be sufficient to be detectable, considering the presence of carbon fragments that generate an unwanted signal, but also sufficiently low to avoid giving an excessive dose to the patient. The energy loss is proportional to $\frac{1}{Z^2}$, and since the charge of helium is equal to $\frac{1}{3}$ the charge of carbon, each helium ion deposits

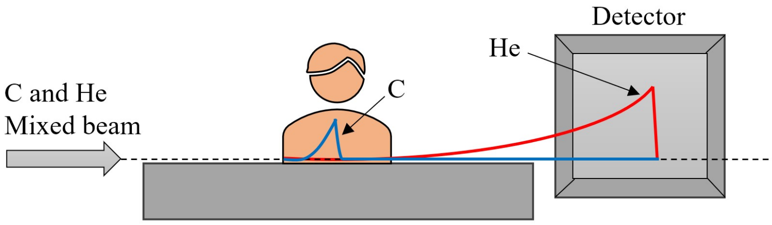

Figure 5.2: Scheme of the proposed He-check system

approximately $\frac{1}{10}$ of the dose compared to carbon.

To ensure a negligible amount of dose deposited into the patient, it has been calculated that the number of helium ions would need to be 10% of the number of carbon ions.

In this thesis work, a FLUKA simulation was performed by Mazzucconi [22] to compare the dose between helium and carbon (Figure 5.3). A certain quantity of helium was added to the carbon so that, for each energy, there would be 10% of helium in respect to the carbon particles. From the simulation, it can be assumed that the absorbed dose in the patient, given by the fraction of 10% of helium, is almost negligible in respect to the sum of the Bragg peaks of the carbon.

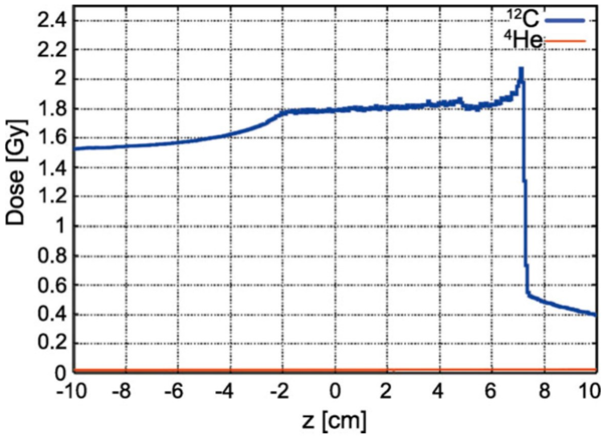

Figure 5.3: Comparison of the dose deposited by carbon in the patient with a SOBP and the corresponding dose deposited by helium. Simulation errors are less than 5% [22]

5.2 Previous studies on the He-check system: Mazzucconi

The first work was proposed by Mazzucconi et al. [22] and had as its fundamental objective the accurate assessment of the number of photons generated by charged particles in the scintillator. The work was divided into two phases.

The first phase involved the validation of two Monte Carlo models [2] (FLUKA [3]) and the second phase consisted of experimentally validating the setup to perform a proper range evaluation.

The first model exploited the FLUKA capability in the generation and propagation of optical photons, while the second model used FLUKA to simulate the energy deposited in the scintillator. In this way, it is possible to simulate and transport to the sensor the fraction of photons that are generated in the scintillator and are seen by the optical system.

5.2.1 Residual range with a plastic scintillator

The range measurement is dependent on the chosen setup. For the preliminary evaluation of the possibility of measuring the helium exiting the patient, a system composed of a plastic scintillator and a CCD camera was used.

5.2.2 Results

The scintillator was irradiated with several pencil beams. The setup was tested with both protons and carbon fragments to assess the capability of the scintillator to discriminate the Bragg peak of the probe particle from the signal coming from the carbon fragments exiting the patient. To simulate the combined signal that would arise from helium and carbon at the same energy per nucleon a water thickness of 20 cm was placed in front of the detector. The carbon beam was set to an energy of 226.5 MeV/u (104 mm range in water) and a proton beam with corresponding energy (range of 320 mm). The particles that were used for protons and carbon were respectively $5\text{x}10^5$ and $5\text{x}10^6$. The results can be seen in Figure 5.4, where protons are 10% in number with respect to carbon.

---

[2] The Monte Carlo method is a computational technique that refers to all those mathematical methods based on probability calculations from which one aims to extract useful information. The fundamental principle of this method is to use random sampling to approximate solutions to problems that would be difficult to solve analytically.

[3] FLUKA (FLUktuierende KAskade) is a Monte Carlo code used for calculations related to the transport of particles in matter and their interaction with it.

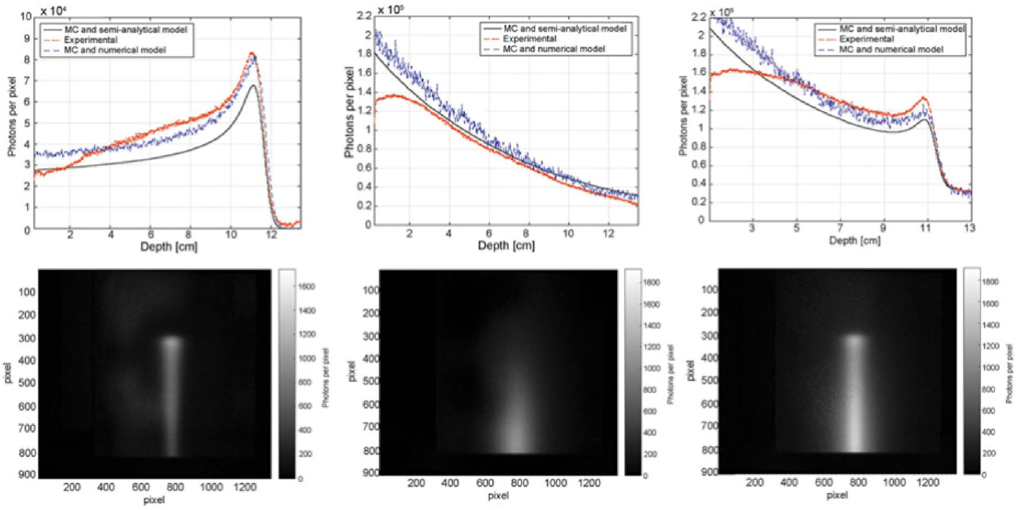

Figure 5.4: Comparison between simulated and measured photons per pixel for a proton and a carbon ions beam. The image shows the protons (up-left), C-ions (up-center), and the protons superimposed to the C-ions (up-right) [3].

To determine the particle range using the acquired images, the number of measured photons was integrated along the x-pixel axis. The resulting distribution has the same shape as the Bragg peak allowing particle range determination.

5.2.3 Range evaluation

Additionally, the system's ability to determine the beam position and the residual range of the particles was assessed. For this evaluation the setup was different, the CCD sensor was substituted with a CMOS sensor because the latter has the potential to acquire at a higher frame rate. To enable range assessment at various points, a depth of field of approximately 200 mm is required, and thus, the optics were replaced.

Of fundamental importance is the distance between the camera and the scintillator because the relative distance between the two influences the parameters of the optical system. The focus of the image must be preserved throughout the thickness of the scintillator to produce a clear image. The region where the image is in focus is called depth of field; an object positioned outside the depth of field produces an out-of-focus image.

It was necessary to account for optical phenomena such as perspective, refraction, and the presence of internal reflections within the scintillator. This required a parametric formula to correctly assess the range of the particles in the scintillator.

With the coordinate system shown in Figure 5.5, multiple images were acquired. In these images, the beam was moved within the scintillator to analyze the capability of range

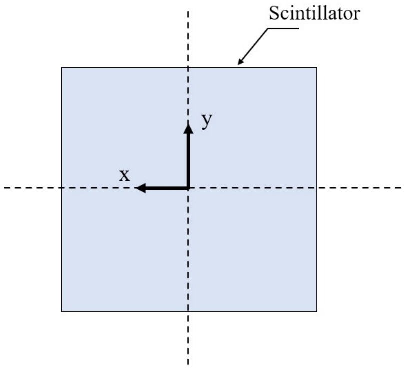

Figure 5.5: The coordinate system used, seen from the sensor's perspective.

measurement and correct the previously mentioned optical effects. The light signal of the acquired images (expressed in ADU) was integrated along the y-direction to obtain the usual Bragg peak shape used for range determination.

$$R = \left[\frac{K_{x=100} - K_{x=-100}}{L_s} \cdot (x - \frac{L_s}{2}) \cdot \frac{n_a}{n_s} + K_{x=100}\right] \cdot \Delta N - \frac{H_r}{L_s} \cdot (x - \frac{L_s}{2}) \tag{5.2}$$

Where K is the proportionality constant indicating the physical dimension occupied by the framed object (scintillator) onto the sensor. ΔN is the number of pixels corresponding to the length of the emitted light in the image and can be expressed as the difference between $N_{threshold}$ and N_{edge}, which are respectively the last pixel beyond a certain luminous threshold and the pixel that frames the edge of the scintillator from which the beam enters. L_s is the dimension of the scintillator (200 mm).

To correct the optical effects different parameters were introduced. The refraction indexes of the air and the scintillator, are respectively n_a and n_s.
H_r is a factor that takes the reflection of the inner walls of the scintillator (in mm) into account. To consider the perspective it must be noted that K depends on the potions of the light along x (unit of measurement: mm/pixel). This is because, from a perspective point of view, if the framed light is farther from the optics, the individual pixel will encompass a larger dimension. Therefore, the values of K must be calculated with respect to the chosen setup

Resolution tests were performed, placing slabs of different dimensions (1 and 2 mm) between the beam and the entrance window. The beam was scanned along the y direction while maintaining the x coordinate. The system's resolution was found to be sufficient to distinguish a 1 mm variation, considering only a pencil beam.

5.3 Previous studies on the He-check system: Landini

In the work proposed by Landini et al. [23], the performance of the He-check system was tested. The work involved a numerical simulation of patient irradiation, followed by the analysis of the hypothetical range of the particles exiting from the volume. Unlike the He-check work proposed by Mazzucconi et al. [22], this study didn't take into account complex geometrical shapes and objects made up of materials with different thicknesses or compositions.

Understanding real anatomical modifications is fundamental since the objective is to irradiate a patient and analyze the hypothetical range of the particles exiting the volume. The simulations were performed using real CT of patients treated in CNAO, using the preliminary CT and the re-evaluation CT, done some weeks after the preliminary one to monitor the evolution of the patient over time. The two CTs were compared in terms of Water Equivalent Path Length (WEPL, in mm).

WEPL is a concept used in the field of radiation therapy and medical physics to quantify the distance that charged particles travel through a medium in terms of the equivalent distance they would travel through water. It standardizes radiation path lengths, making it easier to compare and plan radiation therapy treatment for different tissues and patients.

The WEPL was calculated along the beam direction passing in each planned spot, each time integrating over the encountered patient's thickness, to generate a 2D transmission map of the target volume. The purpose of this study was to analyze the geometry and the treatment plan of specific patients treated at CNAO and to assess whether He-Check can adequately detect certain types of undesired anatomical variations during subsequent sessions. The ultimate goal of He-Check is to provide an innovative in-beam monitoring technique that allows real-time visualization of changes during the treatment, helping to prevent incorrect dose administration without the need to wait for period CT scans to detect such variations.

5.3.1 Results

This work was able to highlight some anatomical variations, leading to the re-planning of the treatment. ΔWEPL maps were compared to existing CT scans to verify if the differences in terms of WEPL corresponded with real anatomical or tumoral variations. It was possible to evaluate variations in the order of at least 5 mm, as smaller variations were difficult to assess due to approximations and uncertainties in both the simulation procedure and the CT images.

Therefore, an indicative threshold of ±5 mm was set to distinguish between significant and insignificant differences in WEPL calculated from the two patient CT scans. It must be noted that the chosen threshold is only indicative, and it cannot be said that the ΔWEPL that surpasses this threshold can be univocally associated with anatomical variations of the patients.

When evaluating some real clinical cases, many of the key hot spots shown in the ΔWEPL maps have been confirmed in the CT images and available data concerning the clinical evolution. On the other hand, other hot spots have revealed misalignments of patient portions that led to overdosing or underdosing in the target volume or surrounding tissues. The simulation method has shown positive results, especially when treating head and neck tumors. Implementing the He-check system and the computational method depicted above could enable direct monitoring after every fraction, potentially preventing critical issues related to a non-correct dose distribution over time.

5.4 Previous studies on the He-check system: Cantù

The work of Cantù et al. [24] partly focuses on the characterization of the new Zyla 5.5 sCMOS camera, a key component that finds application in the present research as well. The Zyla 5.5 sCMOS camera is coupled with a new optical system and brings with it a dedicated software, the Andor Solis Software, suitable for image storing and processing.

The Zyla sensor offers the possibility of both Rolling and Global shutter modes, with the first one providing the lowest noise and the fastest frame rate and the second one offering simultaneous exposure of all pixels in the sensor. For the present work, the camera was used in global shutter mode at the highest possible read-out rate [4].

5.4.1 Setup and characterization

The sensor was initially placed at a distance of 516 mm from the proximal wall of the scintillator and the diaphragm value was initially set to F/28 to achieve a depth of field of 200 mm with a 25 mm focal length.

Subsequently, for a thorough evaluation of the various trigger modalities that the *Zyla* camera offers and the different noises they cause in the images, the camera was set to external start trigger mode. This modality commands each acquisition by exploiting the beam-on timing signal, which operates in synchrony with the treatment administration

---

[4] The read-out rate is the rate at which the collected charge is converted into signal and sent to the amplifier

and, therefore, with the DDS system.

It was then determined that the aperture setting was inadequate as the integral shape is almost indistinguishable from the background noise collected during the acquisition phase. It was also crucial to determine the distance between the camera and the scintillator because it influences various parameters of the optical system.

The reasons why the distance needs to be carefully evaluated are the following: firstly, moving the optics away from the sensor reduces the solid angle subtended by the aperture of the diaphragm; secondly, to have a constant depth of field, varying the distance d_0 brings with it the need to vary the aperture of the diaphragm.

A distance of 633 mm was chosen in consideration of the available space in the setup. This choice was made to maximize the signal while maintaining a Depth of Field (DoF) of 200 mm. Initially, the aperture value was set to F/20. Binning, a process that involves combining nearby pixels into larger pixels, in this case, in a 2x2 grid format, was applied. This binning process helps improve the signal-to-noise ratio but comes at the cost of reduced resolution. After this, the aperture value was adjusted to F/10.

It's important to note that there are two types of binning methods: hardware binning, which is applied before image acquisition and configured in the Andor Solis (software of the Zyla 5.5 camera) properties, and software binning, which is applied after the image has already been captured.

5.4.2 Range Modifications

Given that the range formula used by Mazzucconi et al. was formulated by using a different camera and only in specific cases, the formula was updated. The parameters corresponding to the K(x), the H_r and N_{edge} needed to be calculated again for the specific setup, while $N_{threshold}$ needed further consideration. This parameter denotes the pixel at which the peak ends, identified as the last pixel in which there is an intensity value above a certain threshold. The use of a less specific setup brought forth the need to better define the meaning of this parameter, since with a binning different than 1x1 the variation of only a pixel can lead to errors in the order of millimeters.

In addition to this an average conversion coefficient of 1.02, which takes into account that the density of the scintillator is higher than the density of water (in which ranges are normally calculated), was introduced.

5.4.3 Results

An operational configuration for the optical system was established, by carefully excluding binning and diaphragm settings that might lead to saturation and compromise signal interaction. The system has been configured with a 2x2 binning setting and F/10 diaphragm value.

A modification to the equation proposed in the previous work [22], referred to as Equation 5.2, has been introduced. This modification involves an adjustment to the threshold pixel, defining a calculation method aimed at ensuring a maximum error that doesn't exceed 2%.

Chapter 6

Generalities on image sensors and scintillators

In this chapter, the fundamental aspects of image sensors and scintillators are explored. The choice and characterization of these two components are crucial. Particular attention is dedicated to understanding the noise sources in image sensor design.
Towards the conclusion of this chapter, a description of the chosen setup will be provided, outlining the key characteristics that influenced the selection of the sCMOS camera.

6.1 CCD and CMOS image sensors

In today's camera systems, technologies such as Charged Coupled Device (CCD) and Complementary Metal Oxide Semiconductor (CMOS) sensors are employed to convert incoming optical images into electronic signals using light-sensitive cells known as photodiodes. These cells capture light and transform it into electrical signals, with the sensor's resolution per pixel being directly proportional to the number of photodiodes [25].

CCD sensors, invented in 1969, capture the photons coming from the light source and collect them in cells called photocells, where they are counted and stored along with their coordinates. These sensors are based on MOS (Metal Oxide Semiconductor) capacitor technology, which comprises three different materials: a metallic gate, a silicon oxide insulator, and a substrate of *p-doped* Silicon.

The process begins by applying a voltage to the capacitance, inducing the formation of a depletion zone in the semiconductor layer. This region is highly sensitive to incoming photons. When the photons interact with the depletion zone, electrons are produced, and therefore a voltage difference across the capacitance is generated. This voltage difference leads to the creation of a positive electrical field, which causes the electrons to be gathered towards the gate. Consequently, each sensor pixel registers an amount of electrons proportional to the quantity of incident photons, and hence, to the intensity of the incoming light.

The positive voltage is then applied to each gate in sequence, as illustrated in Figure 6.1. The charge is transferred from one pixel to the next one until it reaches a horizontal shift register, which is made out of a series of capacitors that read the sensor's pixel matrix row by row. An RC circuit is placed at the base of the shift register and converts the charge signal into a voltage signal, which is then converted into a digital signal by an A/D converter.

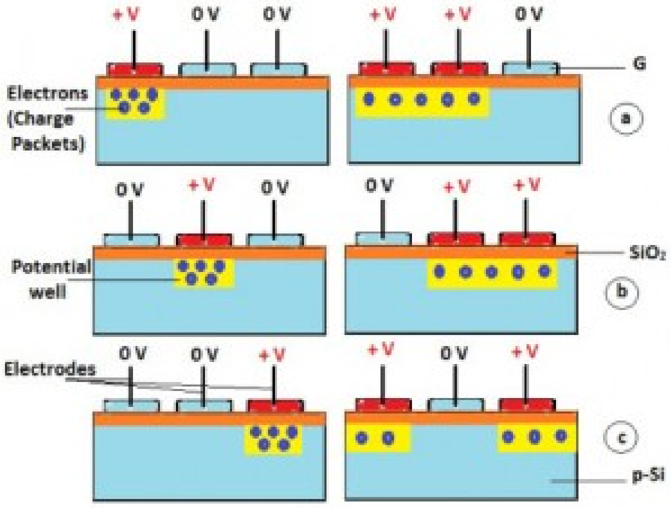

Figure 6.1: Working principle of CCD in which a positive voltage is applied to allow the charge transfer. The three regions that constitute the CCD can be seen: the metallic gate (G), the silicon oxide insulator (SiO_2), and the p-doped substrate (p-Si).

Each sensor has its unique characteristics and the main parameters are:

- Quantum Efficiency (QE): it quantifies the relationship between the number of photon-electrons generated and the number of incident photons.
- Full well capacity: the maximum number of electrons that each pixel can hold.
- Number of electrons per logical unit [e^-/ADU]: the number of electrons collected on a single pixel corresponding to a variation of a unit in the A/D converter.
- Dark current: thermal agitation may generate a gap electron pair, that collects at

the gates. These electrons produce a signal even when the sensor is not exposed to light and they inevitably form a source of noise.

CMOS sensors differ from CCD sensors because they integrate the charge collection, amplification, and A/D conversion functions into each pixel through an integrated circuit. This unique design results in the fact that the CMOS sensor provides a digital output value for each pixel.

Key advantages of CMOS sensors over CCD sensors encompass:

- Higher image acquisition speed (meaning that it has a greater frame rate) due to the swifter transfer of digital signals in CMOS, as compared to the transfer of charge in CCD sensors.
- Enhanced compactness since it doesn't necessitate external devices for the read-out of the charge.
- Cost-effectiveness.

In Figure 6.2 the operational distinctions between CMOS and CCD are illustrated.

However, it should be noted that CCD sensors generally exhibit lower noise levels compared to CMOS sensors, because the presence of a greater number of semi-conductive elements generates a large amount of dark current. CCD sensors also possess higher light sensitivity [25].

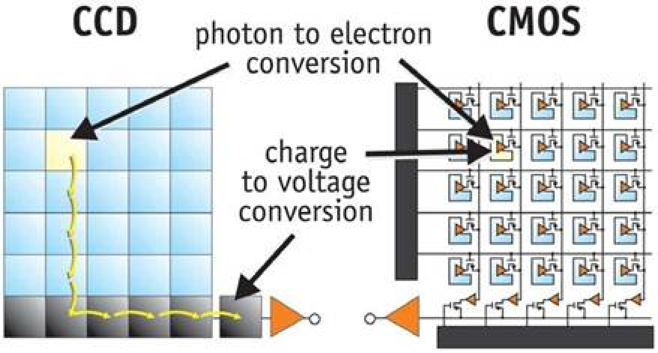

Figure 6.2: Working differences of CMOS and CCD. In the CCD sensor, there is a unique circuit for amplification and conversion whereas in the CMOS sensor, there is an amplification circuit for every sensor [25].

6.2 Scintillator

Scintillators are known for their ability to emit photons when exposed to ionizing radiation. This category of materials includes both organic and inorganic structures [26].

Focusing on organic scintillators, which are of primary interest, and referring to Figure 6.3, when radiation interacts with an organic molecule, it leads to the elevation of an electron from the molecule's ground state (S_{00}) to a singlet excited state (S_1, S_2, etc.), a triplet state (T_1, T_2, etc.), or to one of the molecule's various vibrational states (S_{11}, T_{12}, etc.).

For molecules of interest in organic scintillators, the separation between singlet and triplet energy levels is typically around 3-4 eV, while the separation between vibrational levels is approximately 0.15 eV. The energy associated with thermal agitation is on the order of 0.025 eV. Therefore, before excitation, it can be assumed that all electrons reside in the S_{00} level.

After the radiation has induced excitation, all singlet states de-excite rapidly through non-radiative processes to the S_{10} state. The consequence is that, shortly after excitation, the result is an electron population in the excited S_{10} state.

The light primarily emitted is characteristic of radiative de-excitation from the S_{10} state to one of the vibrational states of the ground state. This process is called prompt fluorescence and is characterized by times on the order of nanoseconds (for organic scintillators). Prompt fluorescence is not the only process for the de-excitation of the molecule.

As mentioned, from the ground state, triplet states can also be populated, and by de-exciting from S_{10} to a vibrational state of the ground state, they contribute to the emitted light. This latter process is called phosphorescence and is characterized by longer characteristic times (on the order of milliseconds) compared to fluorescence. Finally, through the process called inter-system crossing, some triplet states can be thermally excited to a singlet state, resulting in delayed fluorescence compared to the main light emission (delayed fluorescence).

The most important parameter of scintillators is the efficiency of scintillation, defined as the fraction of energy of the incident particles converted into light. This value should be as high as possible but, not all the excitation energy is emitted as visible light because there are other mechanisms of de-excitation present.

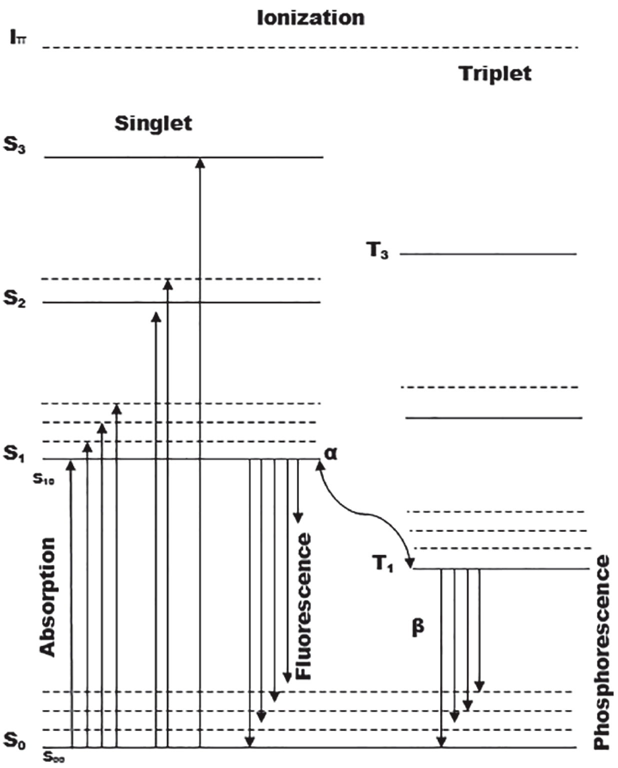

Figure 6.3: 3 Typical energy level of pi-electron organic molecules [27].

6.2.1 Plastic scintillators and Birks formula

The term plastic scintillator commonly refers to a scintillating material where the primary fluorescent emitter, known as *fluor*, is embedded within a solid polymer matrix called *base*. The advantage of these types of scintillators is that they provide a relatively high light output and a quick signal response. Another advantage of these types of scintillators is their high malleability, they can be easily produced in various shapes and sizes.

Only a small amount of the energy deposited by charged particles in the scintillator produces fluorescence photons while the remainder is dissipated as other forms of energy. For plastic scintillators, several formulas and parameters are essential for the understanding and characterization of their performance. One of them is the scintillation efficiency, usually quantified in terms of photons emitted per MeV deposited and depends on the particle and its energy.

If the scintillator's response were linear, the emitted light (L) could be expressed in terms of the number of photons per unit path length as follows:

$$\frac{dL}{dx} = S\frac{dE}{dx} \tag{6.1}$$

Where:

- L is the scintillation light output.
- S is the scintillation light yield, which represents the average number of photons produced per unit of energy deposition.
- dE/dx is the rate of energy loss per unit length along the path of the ionizing particle.

However, the response of the scintillator to charged hadrons is not perfectly linear; it significantly depends on the ionization density of the incident particle.
Birk's Law is a formula used to describe the non-proportional scintillation response of some scintillators at high particle energy or high energy deposition rates.

The non-linear relation between energy deposited per unit length and the emitted light is described by *Birk's Law*:

$$\frac{dL}{dx} = \frac{S\frac{dE}{dx}}{1 + kB\frac{dE}{dx}} \tag{6.2}$$

In which kB is Birk's constant, a parameter that quantifies the non-proportional response, and that depends on the material and is therefore specific to every scintillator.
This last relation is based on the assumption that a high ionization density along the particle's path leads to a quenching phenomenon due to damaged molecules, resulting in a reduction of the emitted light.

Assuming that the density of the damaged molecules along the path is $B\frac{dE}{dx}$, and only a fraction k undergoes quenching, Equation 6.2 is obtained.
This formula suggests that the attenuation of the response is higher as the ionization density of the incident charged particle increases. For example, heavier carbon ions will have a greater impact than protons

The quenching coefficient (kB) of the plastic scintillator used in this setup (*Saint Gobain BC408*) was estimated to be 0.0101 $g/(MeV cm^2)$.
From this, it can be deduced that the quenching effect will be particularly significant, especially in coincidence with the Bragg peak, as the denominator assumes values that strongly impact the light response.

6.3 Noise sources

In this section, various noise sources encountered in image sensor design will be discussed. These sources of noise can significantly impact image quality and accuracy, emphasizing the importance of considering them in the design process.

6.3.1 Photon shot noise

The basis for creating an image from a CMOS sensor relies on the photoelectric effect. Photons follow Poisson statistics, signifying that there will be an average number of photons; however, the actual number will vary due to the discrete nature of the source [28].

This variation is the source of photon shot noise, which can be numerically described with the following formula:

$$\text{shot noise (e-)} = \sqrt{\text{signal(e-)}} \tag{6.3}$$

6.3.2 System noise

Even with no signal, noise can still be measured in electronic images and multiple factors can contribute to what can be referred to as read noise. This noise is generated within the electronics during the readout process when the electrons are converted by the A/D converter, amplified, and processed to produce an image.

Another variant is the reset noise which occurs when the capacitor is reset before the charge accumulation cycle.

6.3.3 Dark signal noise

The dark signal noise is temperature-dependent and accumulates at a steady rate at a given temperature. The noise arising from the dark signal has two components: dark shot noise and dark fixed pattern noise.

The dark shot noise resembles the photon shot noise:

$$\text{dark shot noise (e-)} = \sqrt{\text{dark signal(e-)}} \tag{6.4}$$

While the Dark Fixed Pattern Noise (DPFN) is caused by the non-uniform distribution of the dark leakage current.

$$\text{DPFN} = \text{DSNU} * \text{dark signal (e-)} \tag{6.5}$$

As long as there is no saturation, doubling the exposure time causes the doubling of the DFPN. This type of noise can be removed by 'dark subtraction' (meaning the subtraction

of a dark image from the acquired frame) [28].
The dark shot noise cannot be removed in this way, because it depends on the hardware being tied to the cooling system used in the sensor.

6.3.4 Fixed pattern noise (FPN)

In cases where a camera captures an image of a uniformly illuminated and featureless target, the ideal outcome should be an image without any distinguishable features. Any deviation from this ideal scenario can be attributed to Fixed Pattern Noise (FPN), a form of noise that can impact the precision of electronic images.

FPN typically arises from two primary sources: variances in the uniform delivery of focused light to the image sensor with a wide field of view and variances in the photo response of individual pixels across the image sensor. This latter variation is especially significant in the context of CMOS sensors.

6.3.5 Total noise

The total noise is the sum of the noise components described in the previous sections.

$$\text{Total noise} = \sqrt{\text{system noise}^2 + \text{shot noise}^2 + \text{dark shot noise}^2 + \text{FPN}^2 + \text{DFPN}^2} \tag{6.6}$$

Only the system noise is signal level independent. The other terms have either a dependence on exposure level, integration time, or temperature. Shot noise and FPN depend on exposure level while dark shot noise and DFPN depend on time and temperature

The dark noise component can be therefore reduced and minimized by reducing the exposure time and temperature of the sensor. Dark fixed pattern noise can be removed by dark subtraction, as mentioned before and fixed pattern noise can be removed via a process called flat fielding, which involves dividing the image frame by a pixel calibration image frame [1].

---

[1] The calibration frame is a high SNR (Signal to Noise Ratio) image of a uniformly illuminated background

6.4 Chosen setup

The system consists of a plastic scintillator (Table 6.1) coupled with a scientific CMOS (sCMOS) camera (Table 6.2). As described in [24], the camera was chosen for its characteristics, including a sensor with low noise and high spatial resolution, which is crucial for accurate range evaluation.

Table 6.1: Characteristics of the plastic scintillator

Producer	Saint Gobain Crystals
Model	BC-408 Plastic Scintillator
Dimensions [cm]	20 x 20 x 20
Light yield [% Antracene]	64
Emission wavelength [nm]	425
Main component decay constant [ns]	2.1
Attenuation length [cm]	380
Refraction index	1.58
Density [g/cm^2]	1.032
H:C ratio	1.101

Table 6.2: Characteristics of the optical system

Producer and Model	Andor Zyla 5.5 sCMOS
Sensor dimensions	2560×2160 pixel, 16.6 mm × 14 mm
Pixel size (W x H)	6.5 μm × 6.5 μm
Full well capacity	30000 e^-
Dark current	0.1 e^-/pixel/s at 0 °C
A/D converter	Dual amplifier stage: 16-bit and 12-bit
Electrons per digital unit	0.45 e^-/ADU
Read-out noise	2.5 e^- RMS
Cooling	Thermoelectrical
Producer and Model of the lens	Azure photonics 2520MX5M

The scintillator and sCMOS camera are placed inside a box with black walls to minimize as much as possible the amount of external light that reaches the sensor and would otherwise be a noise source. A schematic view of the setup can be seen in Figure 6.4.

A thin entrance window is located on one side of the box. Through this window, the beam passes, reaching the scintillator. This entrance must be designed to allow the passage of a non-degraded beam, while adequately shielding the inside of the box. For this purpose, a thin aluminum foil has been applied to the entrance window, offering a suitable balance between maximizing shielding and preserving beam quality without degradation

The choice of the distance between the camera and scintillator is a crucial aspect of range

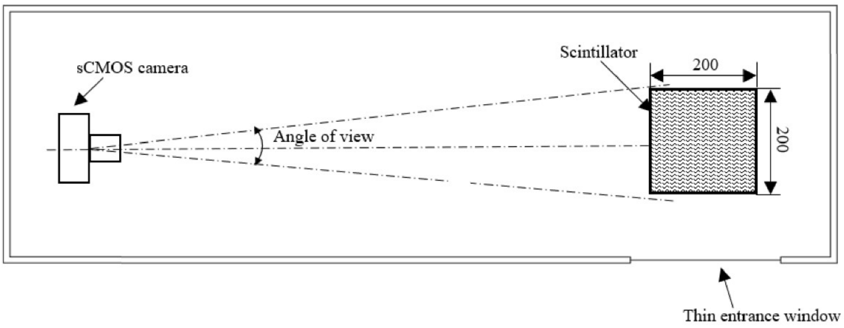

Figure 6.4: Schematic view of the setup (top view), with the thin entrance window [24].

evaluation; the initial distance is chosen with regard to the work previously done [24] and is later modified to suit the purpose of the present work.

The camera must be aligned with the center of the scintillator, while the latter must be aligned to the entrance window; for this purpose two supports (both shown in Figure 6.5) were designed and printed using a 3D printer and inserted in the box.

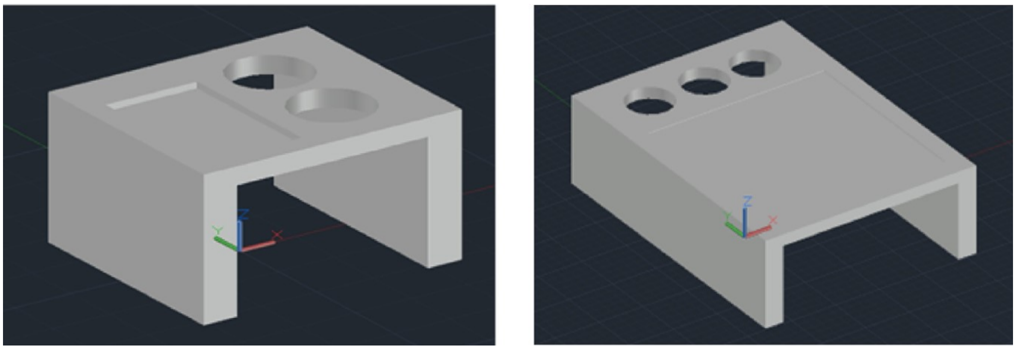

Figure 6.5: 3-D view of the camera support (left) and the scintillator support (right) [24].

6.5 sCMOS camera

The sensor used for the previous work [24] and the present one, is the Zyla 5.5 sCMOS camera (Figure 6.6). The main characteristics of the optical system are summed up in Table 6.2.

The camera is equipped with scientific CMOS (sCMOS) technology, specifically developed for scientific cameras and microscopy applications. This technology ensures extremely low noise, rapid frame rates, a wide dynamic range, high quantum efficiency, high resolution, and a large field of view, all in a single image [29]. The introduction of this new hardware is complemented by dedicated software (Andor Solis Software), designed for image storage and processing.

Figure 6.6: Image of the Andor Zyla 5.5 sCMOS camera used for the He-check.

6.5.1 Sensor shutter modalities

The Zyla 5.5 sCMOS sensor offers the flexibility of both Rolling and Global shutter modes, providing versatile applications. These modes describe two different sequences through which the image is read off an sCMOS sensor.

In the rolling shutter modality, the charge is transferred from each row in sequence during readout (adjacent rows of the array are exposed at slightly different times). This modality offers the lowest noise and fastest frame rate but has the potential downside of spatial distortion resulting from the described exposure mechanism.

On the other hand, the global shutter mode, often referred to as ’snapshot’ exposure mode, ensures that each pixel in the sensor effectively ends the exposure simultaneously. Before the exposure begins, the pixels are held in a ’keep clean state’, and at the start of the exposure, each pixel simultaneously begins to collect charge. At the end of the exposure, each pixel transfers charge simultaneously. This modality provides a 100% duty cycle, resulting in optimal time resolution and photon collection efficiency [29].

For the present work, the camera was used in global shutter mode.

6.5.2 Read-out modes

The camera offers users the flexibility to choose from two distinct acquisition modes that influence its read-out process and, consequently, its response to any input signal. These modes are as follows:

- *Non-Overlap Read-Out Mode*: In this mode, the camera responds to both the rising and falling edges of the input signal. A new exposure cannot commence until the previous one has completed its read-out process, which begins as soon as the falling edge of the trigger signal is detected. This mode's acquisition sequence is entirely contingent on the duration of the high period of the incoming signal.

- *Overlap Read-Out Mode*: In this mode, the camera exclusively detects the rising edges of the input signal. Each detected rising edge initiates a new exposure phase, which can also commence during the read-out phase of the preceding one. This arrangement optimizes the acquisition frequency. Here, the exposure duration spans the entire signal period, including both the high and low phases.

6.5.3 Trigger modes

The Global Shutter acquisition offers various trigger modes, each defining how the start and stop of the acquisition are set and how exposure times are commanded.

To provide a clear understanding of these trigger modalities, it is essential to introduce the following key Global Shutter signals:

- *Acquisition Start*: internal pulse that indicates when the camera receives a command to start the acquisition sequence.
- *FIRE*: the FIRE output indicates the exposure period, being identical for all the pixels.
- *ARM*: the ARM output is used for external and software triggering modes to indicate when the camera can accept another incoming trigger.
- *Global Clear*: it is used to begin a new exposure. A HIGH pulse means that the charge is drained from every pixel, and a LOW pulse means that any photon-electrons generated are accumulating in the pixel. The falling edge indicates the start of exposure.
- *Charge Transfer*: it indicates that the charge in the pixel is transferred to the measurement node (when the pulse is HIGH), and it ends the exposure.
- *Frame Read Out Phase*: indicated when reference and signal frames are read out of the sensor.

The trigger modalities for the Global Shutter acquisition mode are outlined below:

- *Internal/Software Trigger*: exposure time and acquisition start are set by the user and a new exposure cannot start until the previous one has ended. This modality doesn't require any external trigger but is not viable for the purpose of the present work. The reference frame is read out before the Global Clear is performed, with the negative edge of the Global Clear the exposure begins (exposure time defined by the user). In Figure 6.7 the Internal Trigger in non-overlap mode can be seen, while in Figure 6.8 the Internal Trigger in overlap mode is represented.

- *External Trigger*: the acquisition phase starts when the camera detects an external pulse. The exposure time is set by the user via software. In Figure 6.9 the External Trigger in non-overlap mode is represented, while in Figure 6.10 External Trigger in overlap mode can be seen.
- *External Start*: the camera waits for an external trigger to start the acquisition process. Following the trigger detection, the camera switches its work modality to the internal trigger mode, becoming insensitive to any further triggers. In Figure 6.11 the External Start Trigger is depicted.
- *External Exposure Trigger*: Operation mode in which both exposure time and acquisition phase are controlled by an external trigger event in non-overlap mode. In Figure 6.12 the External Trigger in non-overlap mode can be seen, while in Figure 6.13 the External Trigger in overlap mode is represented

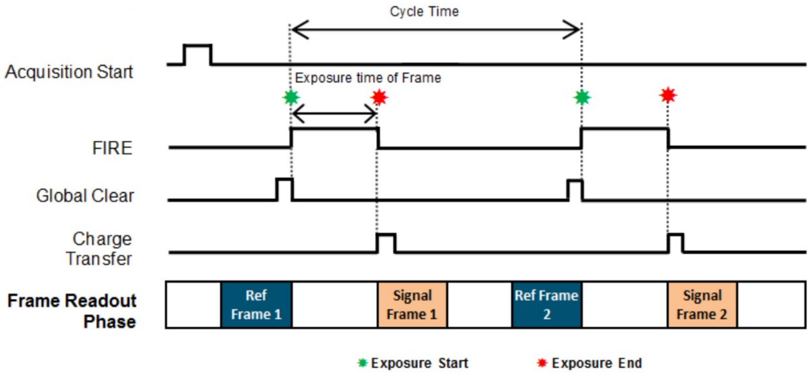

Figure 6.7: Global Shutter Internal/Software Triggering (non-overlap mode).

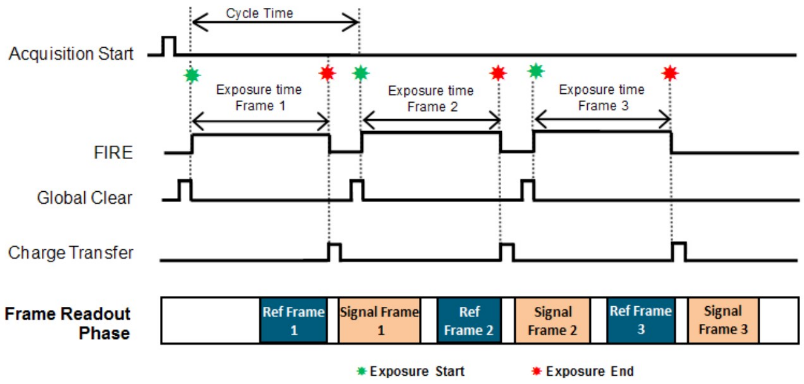

Figure 6.8: Global Shutter Internal/Software Triggering (overlap mode).

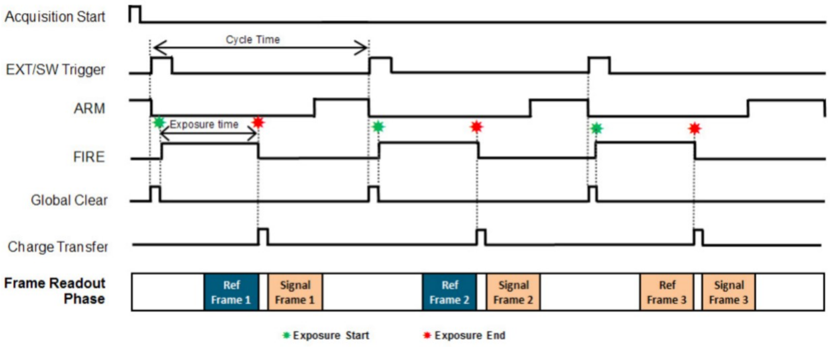

Figure 6.9: Global Shutter External Triggering (non-overlap mode).

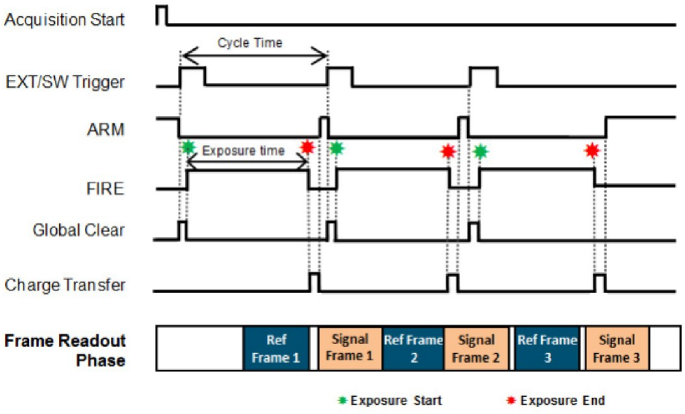

Figure 6.10: Global Shutter External Triggering (overlap mode).

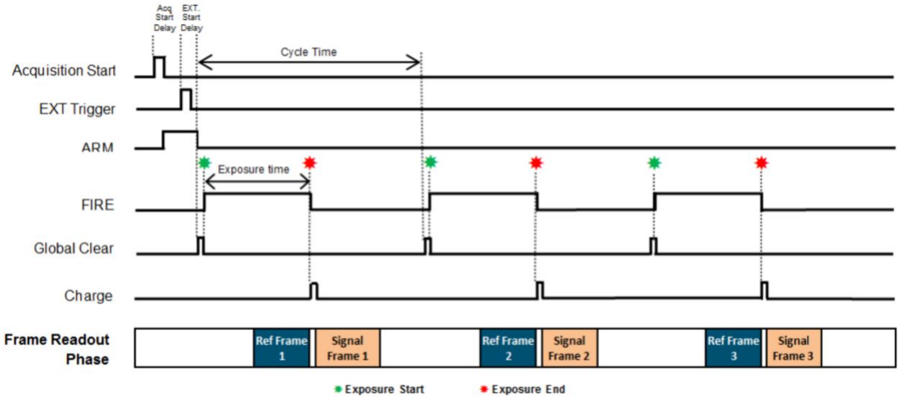

Figure 6.11: Global Shutter External Start Triggering (non-overlap mode).

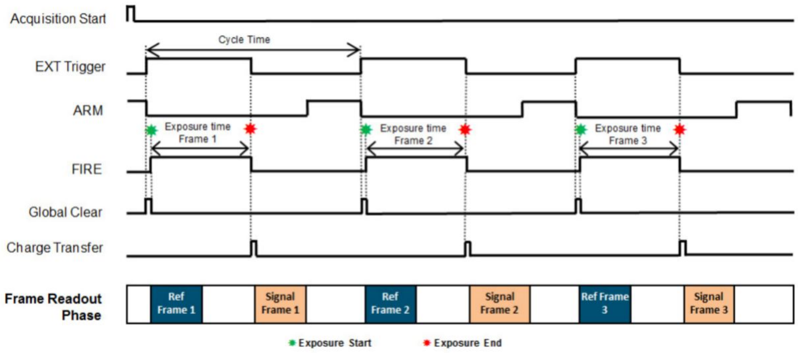

Figure 6.12: Global Shutter External Exposure Triggering (non-overlap mode).

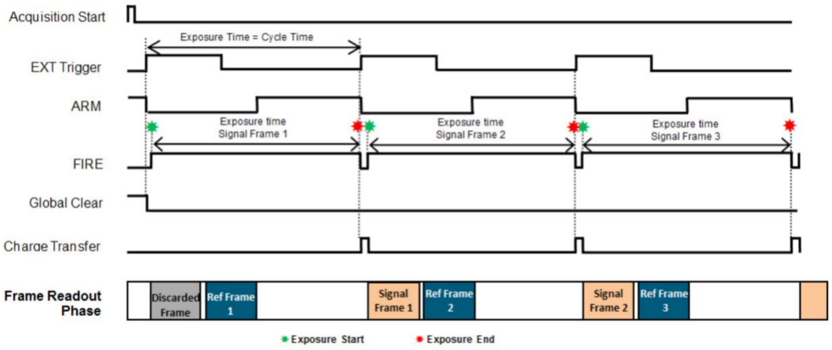

Figure 6.13: Global Shutter External Exposure Triggering (overlap mode).

6.5.4 Acquisition modes

The possibility to select between different acquisition modes is provided.

- *Single scan*: refers to an acquisition in which only a single user frame, after receiving a valid trigger, is transmitted from the camera.
- *Kinetic Series*: refers to an acquisition in which a finite number of user frames, defined by the user, are transmitted from the camera.
- *Accumulate*: refers to an acquisition in which a number of frames in a series is accumulated into a single image.
- *Run Till Abort Acquisition*: an infinite number of user frames can be transmitted from the camera and the acquisition will continue to run until it is aborted.

Chapter 7

Image acquisition

The purpose of this part of the work was to further test the performance of the optical system, continuing the characterization started in the previous works. The setup and parameters of the system are described, including the distance between the camera and scintillator, focal length, binning, and the trigger modality used by the sCMOS camera.

The accuracy and repeatability of the system were verified. Different filtering techniques, such as median filtering and re-binning, were explored to reduce noise and improve image quality through post-processing. Finally, the resolution capabilities of the imaging system are discussed.

7.1 Setup

The setup deployed during the initial measurements can be seen in Figure 7.1, together with the coordinate system. The box containing the camera and the scintillator is placed in front of the DDS of the chosen treatment room (a horizontal line is needed which is present in all the three treatment rooms in CNAO), as depicted in Figure 7.2.

The sensor is placed at a distance of 633 mm from the proximal wall of the scintillator, following the characterization of L. Cantù [24]. The focal length of the lens is 25 mm, the F/ number is set to F/10 and the binning is imposed to 2x2.

It has to be noted that the distance between the camera and the scintillator is crucial and must be carefully evaluated because it influences the various parameters of the optical system.

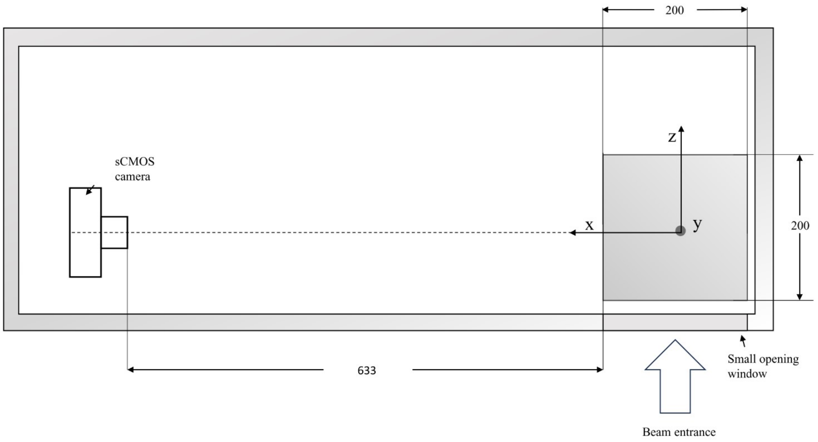

Figure 7.1: Schematic view of the used setup (not in scale). The sCMOS camera and the scintillator with its coordinate system can be seen.

Figure 7.2: Image of the experimental setup in front of the DDS of treatment room number one.

Recalling the equations that define the region in which the image is focused (Equation 4.7 and Equation 4.8) it is possible to establish the following relationship:

$$F/ = \frac{f^2\sqrt{{d_0}^2 + (d_d - d_p)^2} - f^2 d_0}{c(d_d - d_p)(d_0 - f)} \tag{7.1}$$

With a fixed focal length (f) and a constant value of c that depends only on the binning, the F/ number depends solely on the parameters of the imposed depth of field and the focusing distance (d_0).

It will be necessary to evaluate the distance to maximize the amount of light incident on the sensor, considering the following:

- Shifting the optics farther from the sensor results in a decrease in the solid angle covered by the diaphragm's aperture concerning the light source. The light source can be conceptualized as a point source situated at a distance d_0.
- To maintain a constant depth of field of 200 mm, adjustments must be made to the diaphragm's aperture by changing the distance d_0.

Given the available space in the setup, to maintain a depth of field of 200 mm and to maximize the amount of collected signal, it is necessary to position the optical system at 633 mm.

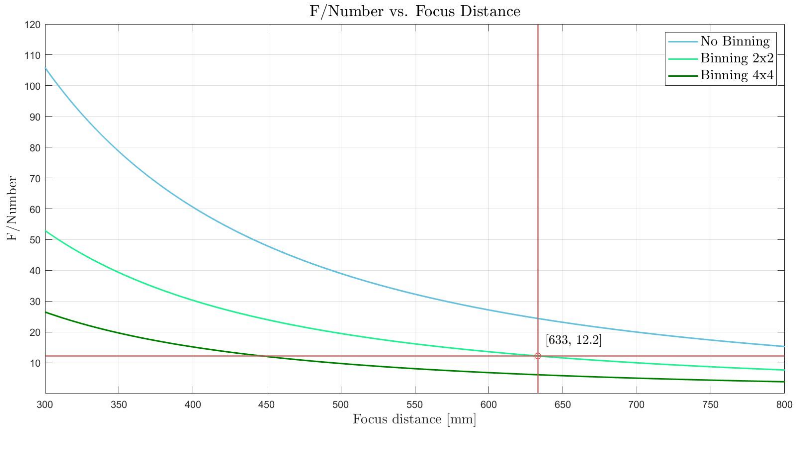

Figure 7.3: Trend of the F/ number at different values of binning (no binning, 2x2, 4x4). At increasing binning values the c value will linearly increase. The chosen focus distance is highlighted and the corresponding F/ Number at 2x2 binning. Would it be with no binning a diaphragm value of F/20 should chosen instead.

Figure 7.3 depicts the curves relative to the F/ number for values of c corresponding to no binning, 2x2 binning, and 4x4 binning. The values of c are respectively equal to 6.5 µm, 13 µm and 26 µm.

7.2 Used Trigger Modality

The primary objective of the setup is to identify the irradiated volume by generating a residual range map of helium particles as they pass through the patient. The optimal approach involves the acquisition and range verification of every single spot.

Due to potential changes in the beam intensity, the time required to deliver a spot changes every time the treatment is delivered, preventing the determination of a specific spot's duration in advance.

The acquisition system will be coupled with the DDS, which is the only system that knows the evolution of the delivery in real-time and can provide both *start-of-spot* and *end-of-spot* signals.

By configuring the camera in external exposure mode, where the exposure time corresponds to the high period of the input signal, it would be ideally possible to acquire the image spot by spot, minimizing the blind period between two consecutive frames (2 µs) with the 'overlap read-out' mode.

However, a common challenge across various acquisition techniques is that the maximum frame rate of the camera is less than 50 Hz, which is insufficient given the number of spots delivered in a second (ranging from a few hundred up to a few thousand). As a result, it becomes impossible to resolve a single spot.

To address this limitation, the image could be divided into slices rather than into spots, obtaining the timing signal that represents the start and stop of a slice. Between two slices a time of 2 seconds is typically needed, corresponding to the time required to accelerate a new beam.

However, this approach cannot be used because of the magnitude of noise introduced by the external exposure modality, which increases with the exposure time. In contrast, the noise level in acquisition modes other than external exposure remains constant, as it will be discussed in the section below.

For these reasons, the camera is set to *External Start* mode. This modality is chosen because it utilizes the first *start-of-spill* signal (timing signal) as the trigger signal. Upon receiving the signal, the camera captures a specified number of frames without interruption. Both the exposure time and the number of frames belonging to the kinematic series must be manually set by the operator.

The main challenge with this approach stems from the unknown duration of a spill. Consequently, it is not possible to accurately define a priori the number of frames or the exposure time, potentially leading to the loss of part of the signal.

To overcome this challenge, the following chapters will employ the *External Trigger* mode. This modality exhibits similar noise characteristics with the External Start Trigger mode while introducing additional interesting possibilities. These functionalities open up the possibility of synchronizing the treatment with the camera acquisition process. This alternative will be explored in greater detail in the following chapters and will not be implemented in the current chapter.

7.2.1 Noise caused by binning

In the previous study, the noise levels in different trigger modalities were assessed for cases where no binning was applied. In this study, binning was taken into consideration, and the noise level was evaluated in the external start modality, employed in the initial measurements. As shown in Table 7.1, when the binning is modified and set to 2x2, both the mean value of the noise and its standard deviation increase.

Table 7.1: The noise levels were calculated for two scenarios: one where no binning was applied and another where a 2x2 binning was employed (external start modality). The values were calculated for increasing exposure time.

	No Binning	Binning 2x2
Exp Time [ms]	Mean Value [ADU]	Mean Value [ADU]
100	117.8 ± 9.5	171.9 ± 23.9
200	117.9 ± 9.5	171.3 ± 24.0
300	117.8 ± 9.6	171.1 ± 24.1
400	117.8 ± 9.7	171.2 ± 24.2
500	117.8 ± 9.8	171.2 ± 24.3
600	117.8 ± 9.9	171.2 ± 24.5
700	117.9 ± 10.0	171.0 ± 24.8
800	117.8 ± 10.2	171.0 ± 25.1
900	117.9 ± 10.3	171.3 ± 25.3
1000	117.8 ± 10.5	170.7 ± 25.7

With no binning applied, the noise value was 118 ± 10 ADU. However, when the binning was set to $2x2$, the noise increased to 171 ± 25 ADU.
The values appear to be constant, which is why this trigger modality was chosen over the external exposure modality.

7.3 Repeatability

The term 'repeatability' refers to a feature or characteristic that remains consistent even when the image is acquired multiple times using the same image acquisition methods [30]. If a system is deemed repeatable, systematic errors can be assessed and potentially compensated, although this is not the case for random errors.

The initially acquired background image serves as a baseline reference and is subtracted from subsequent images. This subtraction process is a crucial step aimed at eliminating certain noise components.

Particular attention should be given to the image data type. Initially, the image is encoded as uint16 (unsigned integer). However, to ensure accurate image subtraction it must be converted to int16 (signed integer).

The post-processing phase involves a series of steps. Firstly, hot pixels were eliminated by imposing a threshold and removing those that exceeded said value. Additionally, a filtering method was applied to remove the hot pixels further.

Hot pixels, common defects found in many cameras, appear as individual bright dots in images. CMOS sensors typically exhibit more hot pixels than CCD sensors under similar conditions. Factors that promote the occurrence of hot pixels usually include long exposure times, high gain settings, and elevated sensor operating temperature [31].

At this stage, the threshold to eliminate hot pixels needs to be set manually depending on the type of image and the depth reached in the scintillator. This aspect requires further refinement.

Additionally, two filtering methods have been evaluated. The first one is the median filter with different kernel sizes, and the second one is a re-binning process that downsizes the image by a certain value, depending on the chosen kernel size.

It is important to note that the images have a peculiar coordinate system, as represented in Figure 7.4. The y-axis starts from the top and not from the bottom, as typically expected. It has to be noted that this coordinate system is not the same as the one represented in Figure 7.1.

7.3.1 First Post-processing

To assess the repeatability of the setup, multiple repetitions, each consisting of five images of paints at different energies, were captured. From those images, a Region Of Interest (ROI) was defined, comprising the area representing the scintillator.

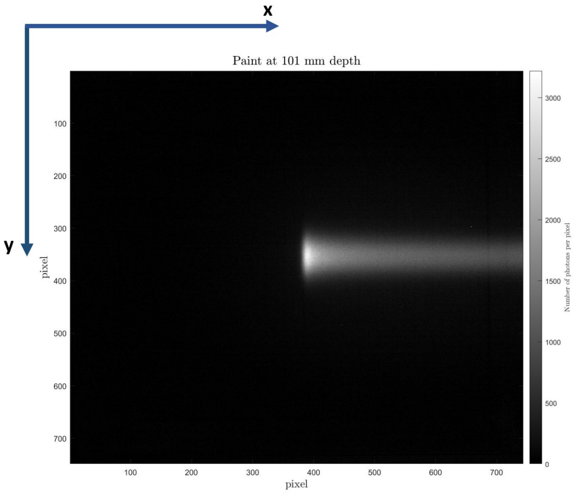

Figure 7.4: In this image the coordinate system of the resulting images can be seen. The y.axis starts from the top, while the x-axis starts from the left.

The scintillator was irradiated with a paint of protons, a small grid, composed of 7x7 spots, with a step of 2 mm. Each spot contained 2e6 particles, resulting in a total of about 100e6 particles. Different paints were employed, each with varying energies (MeV) corresponding to different depths in water. Specifically, energy levels of 80.98 MeV corresponding to a depth of 50 mm, 118.19 MeV for 101 mm, and 163.59 MeV for 181 mm.

Hot pixels were eliminated by applying a threshold based on the mean signal value. Figure 7.5 illustrates the removal of hot pixels for the five images taken at a depth of 101 mm. The hot pixels that were removed are shown in blue, while the filtered signal is represented in yellow. It's important to note that, despite the removal of hot pixels, there may still be some outliers persisting below the chosen threshold value.

7.3.2 Range consideration

After completing the initial post-processing, the repeatability of both the maximum value of the peak and its position was assessed.

For clarity, the formula for calculating the range (Equation 7.2) is presented again. To enhance accuracy, the formula was multiplied by an average correction coefficient, calculated using SRIM. This coefficient takes into account not only the scintillator's density but also considers the fact that the traversed material has a different density than water, along with other material characteristics such as the ionization potential. The selected average correction coefficient has a value of 1.02.

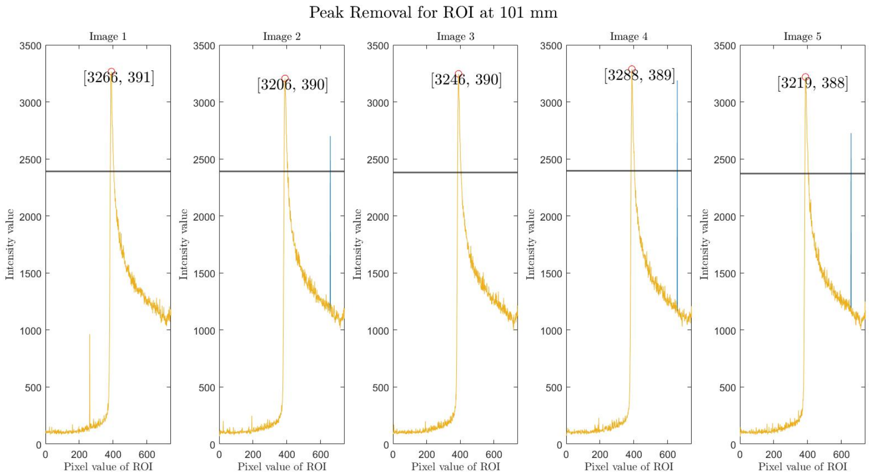

Figure 7.5: The image showcases the initial manual removal of hot pixels, where a row of five images taken at a depth of 101 mm is depicted. The process involved detecting and marking the value and position of the peak in each column, effectively removing hot pixels.

What was, in the previous work [24], labeled as $N_{threshold}$, will now be referred to as N_{peak}. The process of determining the range involves calculating the peak value utilizing the *findpeaks* function.

While this approach may differ from the methodology presented in [24], it is chosen to ensure a robust selection of specific points. This decision is made with the primary goal of enhancing repeatability, which is the central focus of this chapter.

$$R = \left[\left(\frac{K_{x=100} - K_{x=-100}}{L_s} \cdot \left(x - \frac{L_s}{2} \right) \cdot \frac{n_a}{n_s} + K_{x=100} \right) \cdot (N_{edge} - N_{peak}) - \frac{H_r}{L_s} \cdot \left(x - \frac{L_s}{2} \right) \right] \cdot 1.02 \tag{7.2}$$

7.3.3 Mean Values and standard deviations at different depths

The mean value and standard deviation of the peak values of the five images at various depths were calculated, and the results are presented in Table 7.2.

In each image, the peak value was determined by identifying the maximum value within the region of interest that defines the scintillator. This calculation was performed after the removal of hot pixels that could potentially bias the result. The position of the peak is defined as the index of the pixel where the maximum value is found. The peak values are represented with red dots in Figure 7.6.

This process was applied to each of the five available images at different depths, and the results were then averaged.

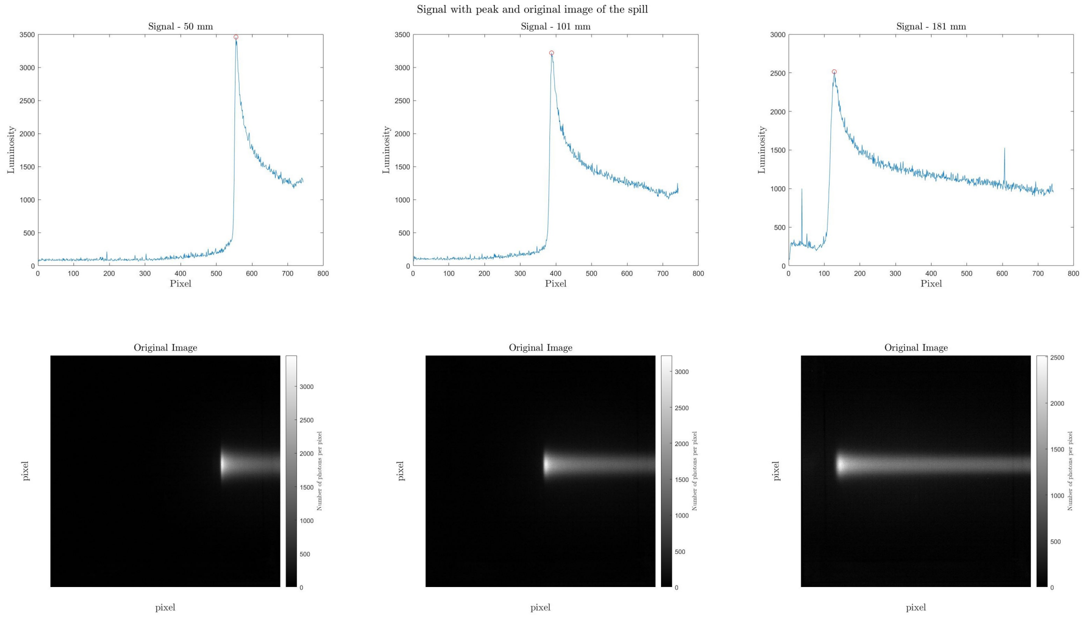

Figure 7.6: In this image the signal at different depths can be seen and the value of the peak is highlighted by a red dot. The original image is also shown.

Table 7.2: Mean Value and standard deviation of the paint for different depths.

Depth [mm]	Mean value and std of the peak [ADU]	Mean value and std of the position [pixel]	Calculated range [mm]
50 mm	3418 ± 41	556 ± 1	52.1 ± 0.2
101 mm	3245 ± 34	390 ± 1	96.7 ± 0.3
181 mm	2527 ± 29	128 ± 2	173.7 ± 0.5

From the data, it can be observed that as the depth increases, the mean value of the peak decreases. It's important to note that the number of particles is consistent for every measurement. However, the greater depth introduces a larger distance for the particles to travel, resulting in increased dispersion. This dispersion contributes to a reduction in the mean value of the peak as depth increases.

Additionally, the results indicate that range measurements become less precise as the beam penetrates deeper into the scintillator. A potential explanation for this phenomenon is the use of an average correction factor. It may be more accurate to adjust the correction factor based on the depth of beam penetration.

Different approach

For a more precise measurement, an alternative approach can be considered. This method involves defining a region of interest (ROI) around the peak and calculating the maximum value as the average of the values within the chosen ROI, instead of just taking the maximum.

The ROI was defined as follows: first, the signal was integrated along the columns to identify the Bragg peak. This process was repeated for each of the five images, and the resulting curves were averaged to obtain an average Bragg peak for each depth. The same was done along the rows.

The maximum peak value was then calculated for the averaged curve, and values between the maximum and 80% of the maximum were selected.

In Figure 7.7, the defined Region of Interest (ROI) for a depth of 101 mm is illustrated, with the curve representing the integrated Bragg Peak. Figure 7.8 displays the ROI calculated using the explained methodology, outlining the selected area of the original image.

What occurs is that the obtained ROI expands as the beam penetrates deeper into the scintillator due to the widening of the Bragg peak. Subsequently, each image is cropped using the obtained indices for the respective depths.

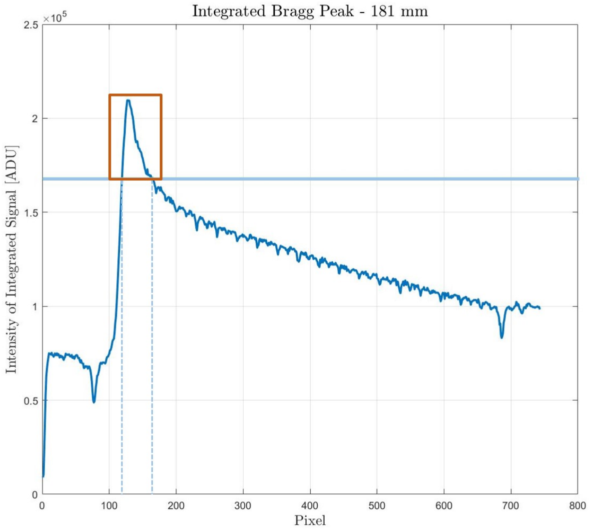

Figure 7.7: In this image, the columns were integrated to identify the Bragg peak. This process was repeated for each of the five images, and the resulting integrated curves were averaged. The values within the red rectangle will be average to obtain the average peak value of the ROI.

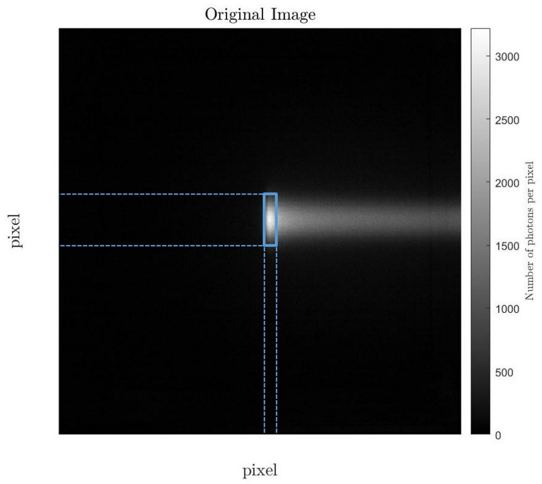

Figure 7.8: In this image, the ROI calculated with the explained methodology can be seen. The values in the chosen ROI will be averaged to obtain an average peak value.

The main difference between the two methods lies in the fact that the mean value represents a lower intensity since it is an average. It also demonstrates higher repeatability, as evidenced by the reduced standard deviation across measurements.

Table 7.3 presents the mean value of the ROI identified through the previously explained method and the peak value of the unfiltered image. The mean values and standard deviation are calculated on the five images at different depths.

The third and last columns illustrate the percentage difference between the standard deviation and the mean value. The proposed method guarantees better repeatability.

It is crucial to consider the specific ROI under discussion. In the first method, a comparison is made between a single value (the maximum value present in the subtraction as noise) and the single value of the peak. In this method, a comparison is made between a single value (noise) and an average over a ROI.

Table 7.3: Mean value of the chosen ROI (different approach) and peak value (original approach), the mean value, and the standard deviation compared in percentage.

Depth [mm]	Mean Value ROI different approach [ADU]	Diff. %	Peak Value original approach [ADU]	Diff. %
50	2665 ± 11	0.4 %	3418 ± 41	1.3 %
101	2453 ± 11	0.5 %	3245 ± 34	1.1 %
181	1821 ± 11	0.6 %	2527 ± 29	1.2 %

7.4 Noise evaluation

To assess the repeatability of these images, subtraction was performed on images obtained at the same depth, aiming to isolate and quantify the intrinsic noise present within the images. Accurate measurement and characterization of this noise are essential, as they offer crucial insights into the overall image fidelity and the reliability of the data.

Initially, the images were subtracted without filtering. As mentioned before, some hot pixels were successfully eliminated by imposing a threshold and removing those above it. However, inevitably, some hot pixels weren't eliminated from the image because they were below the chosen threshold value.

The decision was taken to evaluate the noise starting from the highest luminosity value present in the subtraction.

The images were post-processed using two distinct strategies:

- *Median Filter*: A median filter is a nonlinear filter where each output sample is computed as the median value of the input sample [32]. Primarily used for noise reduction, the median filter is particularly effective at removing salt-and-pepper noise, a type of noise that introduces random white and black pixels in the image (also called hot pixels). The median filter replaces these pixels by processing the median value of the neighboring pixels. // Since the median value is less sensitive to extreme values, this process effectively reduces noise. Notably, the median filter is less likely to blur or smooth out edges and fine details present in the image, preserving edges and sharp transitions.
- *Re-binning with a kernel*: each image is divided into non-overlapping blocks. Each block is averaged, and the pixels are replaced with the average value of that block. This process reduces the image size.

Results without any type of filtering

Before assessing the results obtained with the two proposed filtering methods, the images were initially subtracted without any filtering or re-binning. The outcome is presented in Table 7.4 and visually depicted in Figure 7.9.

In Figure 7.9, the presented scenario represents the worst-case situation and is not indicative of every occurrence. When no hot pixels are present near the peak, the maximum values of the image subtraction typically hover around 350 ADU. This configuration is not optimal and highlights the necessity for additional post-processing, to guarantee accurate image comparisons.

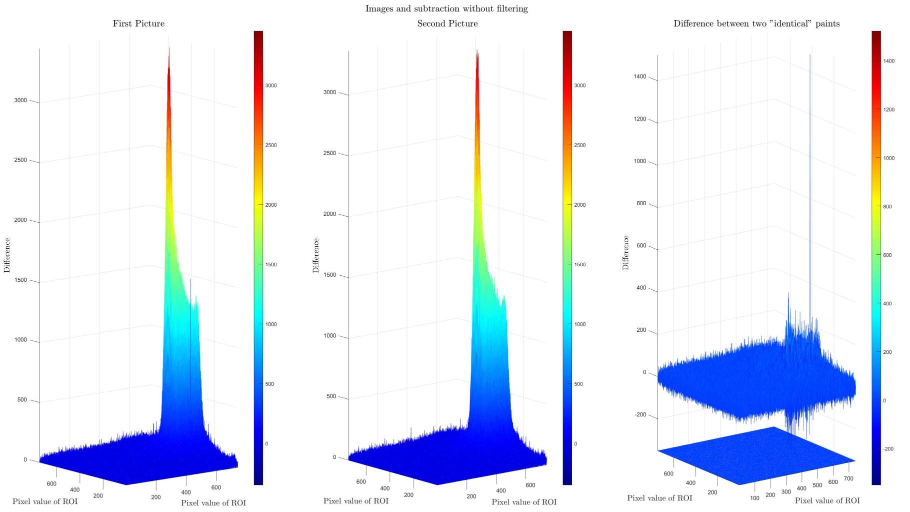

Figure 7.9: In the presented image, two paints taken at 50 mm depth are shown along with their relative subtraction. The presence of a hot pixel near the peak that couldn't be eliminated is evident, resulting in a notably high value in the subtraction.

Table 7.4: In this table the peak value of the unfiltered image is presented and the maximum and minimum values of the subtraction between what should be similar images without any post-processing applied.

Depth [mm]	Original Image Peak Value [ADU]	Difference Image Maximum Value [ADU]	Minimum Value [ADU]
50	3418 ± 41	814 ± 590	-633 ± 456
101	3245 ± 34	890 ± 450	-449 ± 297
181	2527 ± 29	1117 ± 290	-780 ± 316

Results with median filter

To further eliminate outliers in the images, a median filter was applied with different kernel values, a common technique in image processing with several advantages. These values are compared in Table 7.5.

Image subtraction was then performed, and the minimum and maximum results of the resulting images are shown in Table 7.6, indicating the outcomes for both a [3x3] and a [5x5] kernel. It is crucial to consider that as the kernel size increases, the resulting image becomes progressively smoother, leading to lower peak values.

To assess noise levels, image subtractions were conducted and the maximum value within this subtraction process was isolated. Subsequently, this maximum value was compared with the peak values derived from the filtered images. This approach allows for the quantification of the noise present in the data.

In Figure 7.10, a visual representation of two images after median filtering with a [3x3] kernel and their subtraction is presented. In this case, the presence of hot pixels was mitigated by the filtering method.

Table 7.5: Mean and standard deviation values for the peaks for the unfiltered image and the filtered image with [3x3] and [5x5] kernel.

Depth [mm]	Peak value (Unfiltered)	Peak value [3x3]	Peak value [5x5]
50 mm	3418 ± 41	3287 ± 14	3212 ± 38
101 mm	3245 ± 34	3115 ± 39	3077 ± 27
181 mm	2527 ± 29	2415 ± 17	2372 ± 25

Table 7.6: Maximum and minimum values (val) of the subtraction between what should be similar images. The subtraction was performed on images filtered with a median filter using both a [3x3] and a [5x5] kernel.

Depth [mm]	Filtered [3x3]		Filtered [5x5]	
	Max val [ADU]	Min val [ADU]	Max val [ADU]	Min val [ADU]
50	187 ± 38	-199 ± 30	156 ± 36	-153 ± 21
101	221 ± 40	-167 ± 22	175 ± 39	-146 ± 18
181	168 ± 16	-146 ± 29	126 ± 17	-99 ± 19

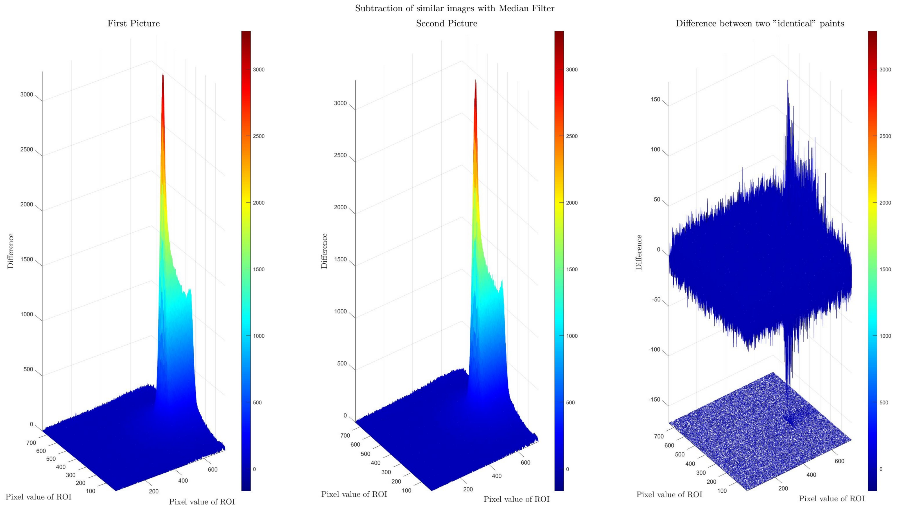

Figure 7.10: In this image, two paints taken at a depth of 50 mm are presented along with their relative subtraction. The applied filtering method is a median filter with a [3x3] kernel.

Results with re-binning

The results of the re-binning on the peak values can be seen in Table 7.7, while the maximum and minimum values calculated after the subtraction of two images that should be identical can be seen in Table 7.8.

In Figure 7.11, a comparison between two images at 50 mm depth in water and their subtraction is presented.

Table 7.7: Mean and standard deviation values (val) for the peaks for the unfiltered image and the filtered image (re-binning) with [3x3] and [5x5] kernel.

Depth [mm]	Peak val [Unfiltered]	Peak val [3x3]	Peak val [5x5]
50 mm	3418 ± 41	3218 ± 20	3092 ± 24
101 mm	3245 ± 34	3080 ± 31	2974 ± 16
181 mm	2527 ± 29	2385 ± 21	2366 ± 19

Table 7.8: Maximum and minimum values (val) of the subtraction between what should be similar images, the subtraction was done with images filtered with re-binning with both a [3x3] and a [5x5] kernel.

Depth [mm]	**Filtered [3x3]**		**Filtered [5x5]**	
	Max val [ADU]	Min val [ADU]	Max val [ADU]	Min val [ADU]
50	124 ± 42	-107 ± 16	52 ± 13	-58 ± 13
101	136 ± 29	-105 ± 27	76 ± 24	-49 ± 9
181	170 ± 49	-124 ± 42	83 ± 30	-56 ± 24

Comparison between the two methods

This re-binning method has proven to be less effective than the median filter for the removal of hot pixels. As illustrated in Figure 7.12, this image exhibited a hot pixel near the peak, which couldn't be removed with the manual method without affecting a portion of the peak. The contrast in effectiveness between the two methods is evident; the hot pixel appears nearly completely removed in the median filtering (Figure 7.13), whereas it persists for the [3x3] re-binning kernel and is reduced in the [5x5] kernel.

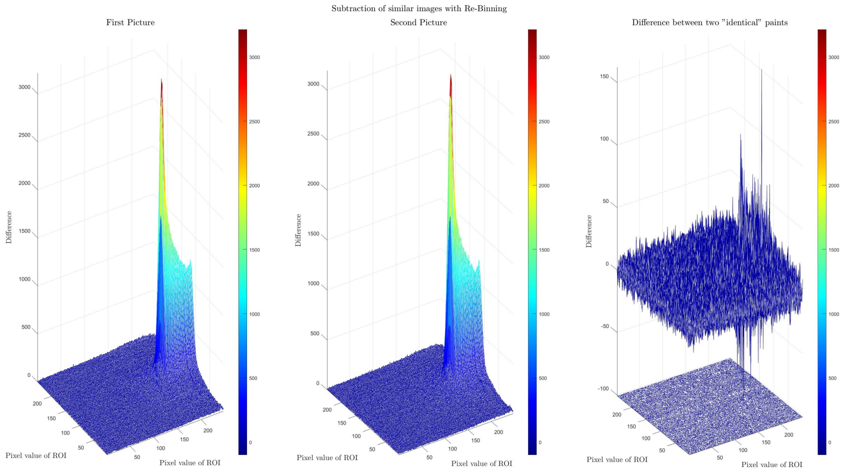

Figure 7.11: In this image, two scans taken at a depth of 50 mm are depicted, along with their relative subtraction. The applied filtering method is a median filter with a [3x3] kernel.

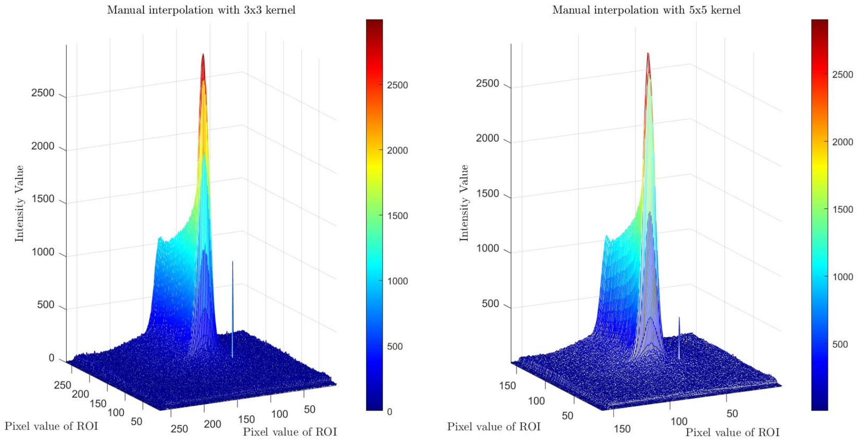

Figure 7.12: Results of the effect of re-binning applied to an image that presented a hot pixel near the peak, which couldn't be removed manually. Re-binning was performed with a 3x3 and a 5x5 kernel.

7.4.1 Results: Effectiveness of Filtering Techniques

Filtering techniques play a crucial role in post-processing the images. For this work, two filtering techniques were applied: median filtering and re-binning. These techniques were evaluated using similar images captured with the same setup, on the same day, and with the same energy.

The expectation is that the images should be identical (within the repeatability of dose

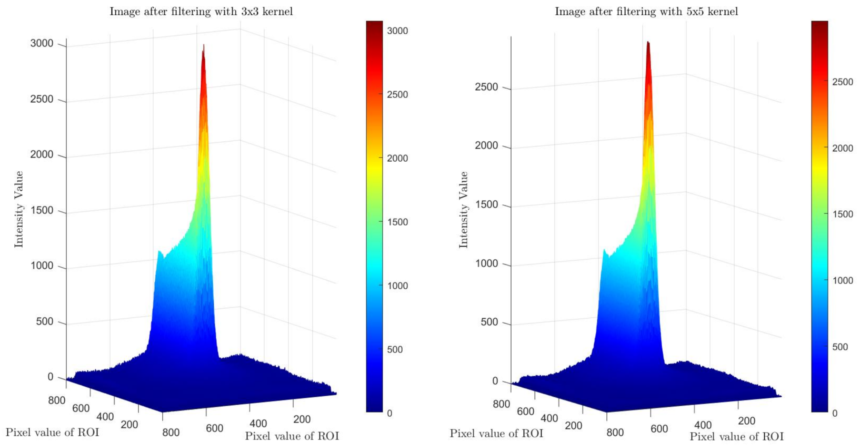

Figure 7.13: Results of the effect of median filter applied to an image that presented a hot pixel near the peak, which couldn't be removed manually. Median filtering was performed with a 3x3 and a 5x5 kernel. The hot pixel is completely eliminated.

delivery). The purpose of this section is to delineate a threshold beyond which it can be defined that two images can be considered the same.

The maximum and minimum values in Table 7.6, for the median filtering method, and Table 7.8, for the re-binning method, depend on the image that is subtracted first, therefore both the values where calculated and the biggest one in absolute value was the one confronted with the peak value, which can be found respectively in Table 7.5 and Table 7.7, to establish the difference.

When the median filtering method is applied, the difference in percentage, between the maximum value of the filtered peak and the maximum value of the image subtraction is 6.7 ± 0.6 % of the peak value for the 3x3 kernel and 5.3 ± 0.4 % of the peak value for the 5x5 kernel.

When the re-binning is applied, the difference in percentage between the filtered peak and the result of the image subtraction is around 5.1 ± 1.7 % for the 3x3 kernel and 2.7 ± 0.8 % for the 5x5 kernel.

Pixel binning, particularly re-binning, emerged as a valuable technique for mitigating artifacts in the subtraction process. The controlled grouping of pixels through re-binning helped reduce noise. Still, the possibility of having a hot pixel increases the risk of having a less accurate result and therefore a median filtering approach should be preferred.

7.5 Subtraction among different images

To quantify the resolution of the system, images at different depths were captured, specifically at 50, 52, and 54 mm as well as at 101 and 103 mm.
These images underwent the application of the two previously described filters, and the subtraction was performed (considering negative values).
Initially, the images were considered without filtering to evaluate the peak value and the range, as shown in Table 7.9. This was done to be able to compare the unfiltered peak with the one obtained from the filtered images.

What is apparent is that the calculated range for depths at 50, 52, and 54 mm is not accurate. This discrepancy arises from the imprecise alignment of the scintillator with respect to the camera axis. From the images taken in light conditions, it appears that the scintillator was not correctly positioned.
An exhaustive assessment of the positioning inaccuracies is necessary to prevent such errors initially and, subsequently, to implement a way of compensating them within a certain range.

Table 7.9: Evaluation of the mean value of the peaks and the position at different depths. The position was calculated in pixel and then in mm with the range formula

Depth [mm]	Peak Value [ADU]	Position [Pixel]	Range [mm]
50	3512 ± 36	547 ± 0	56.0 ± 0
52	3467 ± 149	541 ± 1	57.7 ± 0.2
54	3477 ± 128	534 ± 1	59.4 ± 0.3
101	3239 ± 123	380 ± 1	100.8 ± 0.2
103	3223 ± 235	373 ± 2	102.8 ± 0.4

Subtraction with Median Filter and re-binning

To subtract the images at different depths, the first step involved applying the filtering method to each image. Subsequently, the three images available at different depths were averaged, and the subtraction was performed.

In Figures 7.14 and 7.15, a 3D representation of the subtraction with the two filtering techniques is depicted. These figures illustrate the subtraction between images at depths of 52 and 50 mm, as well as 103 and 101 mm. In the first case, a median filtering method with a [3x3] kernel was applied, while in the second case, re-binning with a [3x3] kernel was employed.

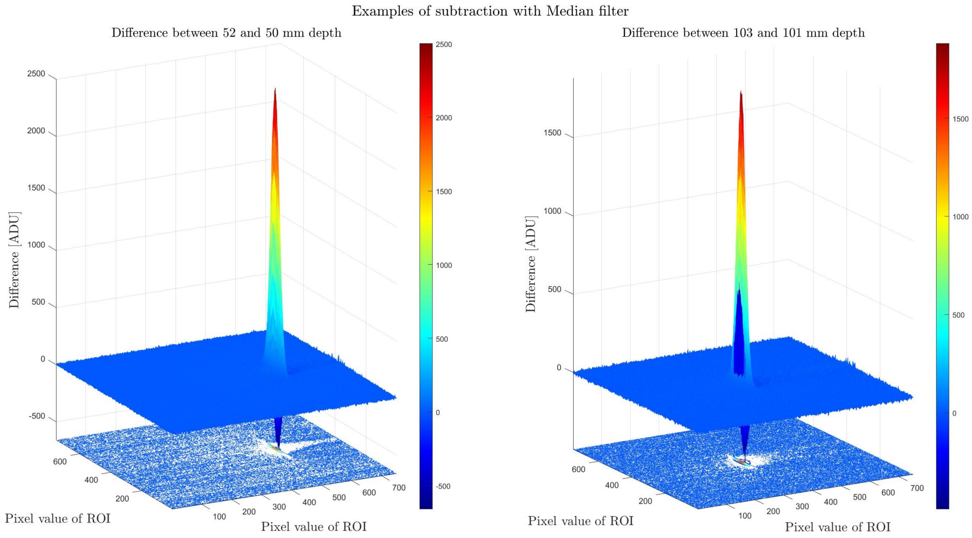

Figure 7.14: Median Filter: 3D representation of the subtraction of the 52 mm and 50 mm depth images (right) and the subtraction of the 103 mm and 101 mm images (left).

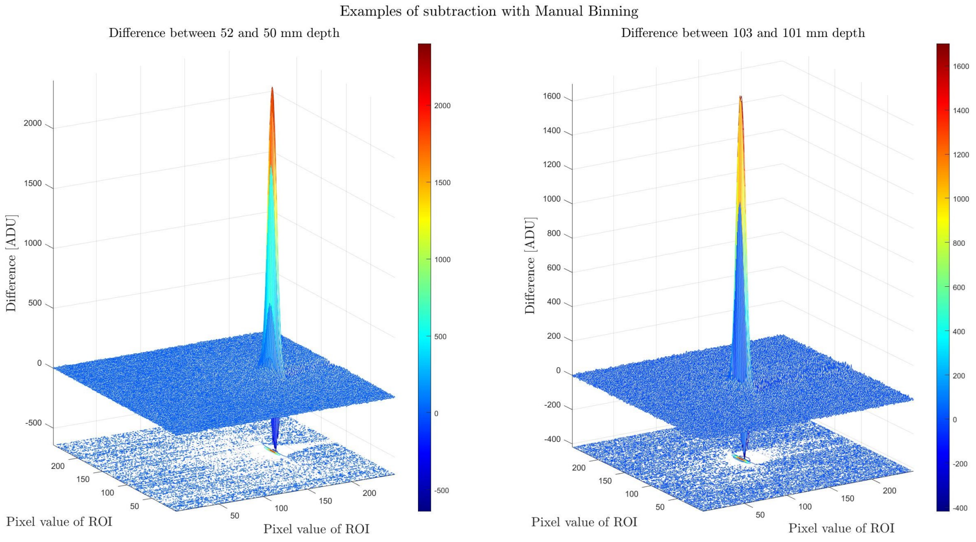

Figure 7.15: Re-binning: 3D representation of the subtraction of the 52 mm and 50 mm depth images (right) and the subtraction of the 103 mm and 101 mm images (left).

In the following tables, the average maximum and average minimum values of the subtraction of previously filtered images are presented. Table 7.10 displays the results of a median filter, while Table 7.11 shows the results of re-binning.

Table 7.10: *Median filter* [3x3]: Subtraction among the different images with their maximum and minimum values of the peak, along with their standard deviations.

Subtraction	Maximum Value [ADU]	Minimum Value [ADU]
52 - 50	2502	-660
54 - 52	2465	-637
54 - 50	3002	-1014
103 - 101	1881	-492

Table 7.11: *Re-binning* [3x3]: Subtraction among the different images with their maximum and minimum values of the peak, along with their standard deviations

Subtraction	Maximum Value [ADU]	Minimum Value [ADU]
52 - 50	2400	-641
54 - 52	2345	-606
54 - 50	2924	-983
103 - 101	1701	-418

7.5.1 Results

In this chapter, the objective was to assess the resolution of the imaging system by capturing images at different energies, followed by the subtraction of said images.

To enhance the clarity of depth differences, median filtering and re-binning with a [3x3] kernel were applied to the images. Tables 7.10 and 7.11 present the mean maximum and mean minimum values of the filtered image subtractions. Both filtering techniques seem to provide a clear visual representation of the differences between images.

The evaluation included images at depths of 50, 52, and 54 mm, as well as 101 and 103 mm. Despite challenges in alignment, the system exhibited the capability to distinguish a 2 mm difference in depth.

Figures 7.16, 7.17, 7.18, and 7.19 visually illustrate the impact of median filtering and re-binning on image subtraction. The distinct visual separation in the 2 mm depth difference is evident in both the 50 and 52 mm, as well as the 101 and 103 mm subtractions.

This assessment underscores the robustness of the imaging system, highlighting the effectiveness of the applied techniques in accurately resolving millimetric depth variations.

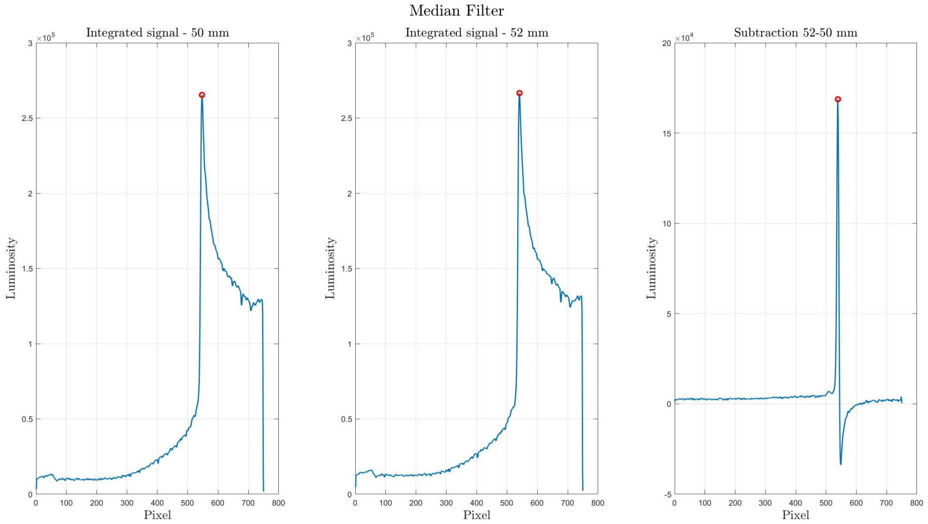

Figure 7.16: Median Filter: example of the Bragg Peak calculated from the 52 mm and 50 mm depth images. On the left, the integration of the subtracted image is displayed, with the red dot signifying the peak value on the x-axis (position).

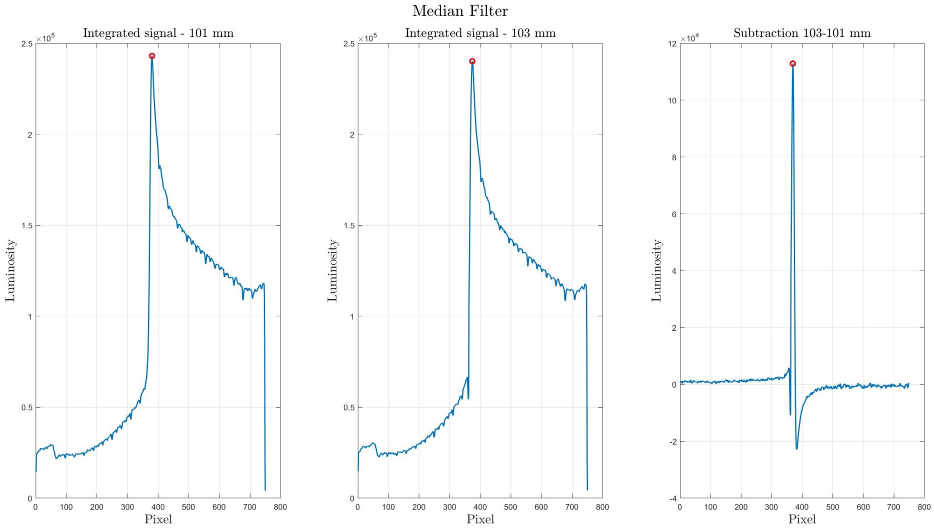

Figure 7.17: Median Filter: example of the Bragg Peak calculated from the 101 mm and 103 mm depth images. On the left, the integration of the subtracted image is displayed, with the red dot signifying the peak value on the x-axis (position).

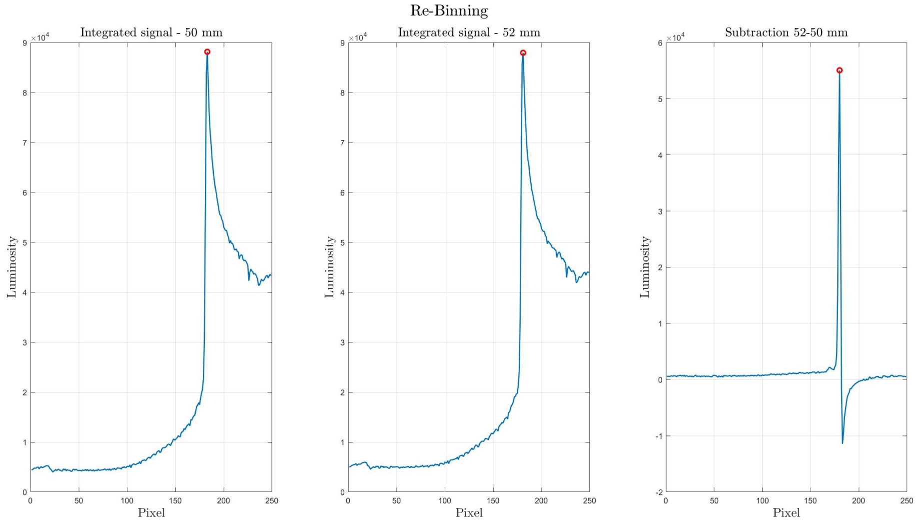

Figure 7.18: Re-binning: example of the Bragg Peak calculated from the 52 mm and 50 mm depth images. The integration of the subtracted image is displayed on the left, with the red dot signifying the peak value on the x-axis (position).

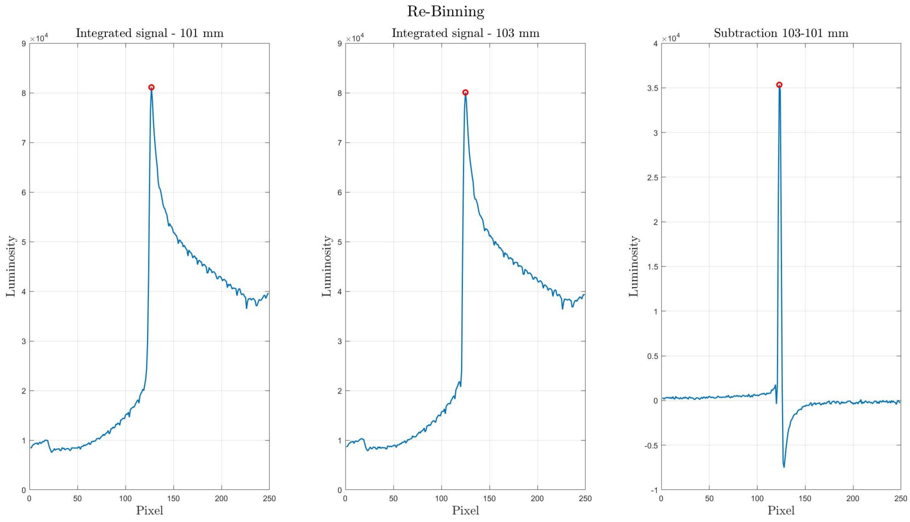

Figure 7.19: Re-binning: example of the Bragg Peak calculated from the 52 mm and 50 mm depth images. The integration of the subtracted image is displayed on the left, with the red dot signifying the peak value on the x-axis (position).

Chapter 8

Mirror Setup for 3D Measurement

In this chapter, significant modifications of the experimental setup are introduced by adding a mirror next to the scintillator. This adjustment has the purpose of achieving a three-dimensional measurement of the beam's characteristics, enhancing the two-dimensional assessment.

8.1 Introduction

The beam enters through an entrance window covered by a thin aluminum foil as previously described. The coordinate system is illustrated in Figure 8.1.

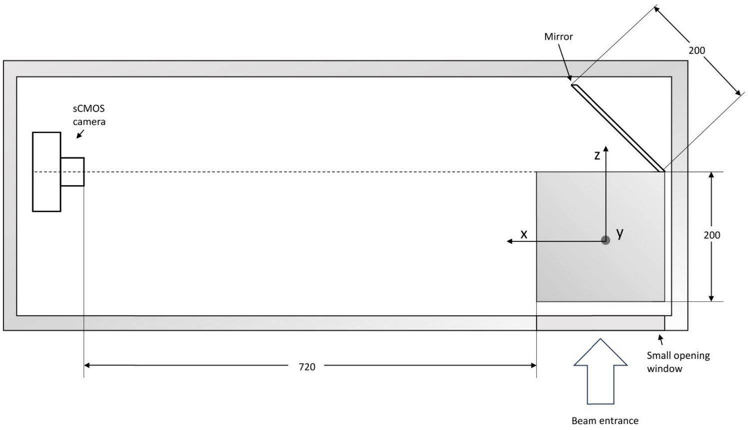

Figure 8.1: In this figure, the setup for the initial measurements with the mirror is displayed, along with its coordinate system.

The implementation of a mirror enables the measurement of the x-position (transversal position) of the Bragg peak. A detailed analysis of the new setup leads to the necessity to modify previously established parameters and considerations. For example, with the camera axis now aligned with the left edge of the scintillator, certain parameters in the range formula, such as the correction factors for the optical effects, need reassessment.

The mirror, measuring 200 x 200 mm, is positioned within the setup at a 45-degree angle relative to the scintillator. For a detailed representation of the mirror and its position, refer to Figure 8.2.

To optimize the visibility of both the scintillator and the mirror, the distance between the sCMOS camera and the scintillator has been adjusted from 633 mm to 720 mm. This modification ensures a clear view while allowing the maintenance of the aperture settings at F/10, as depicted in Figure 8.3.

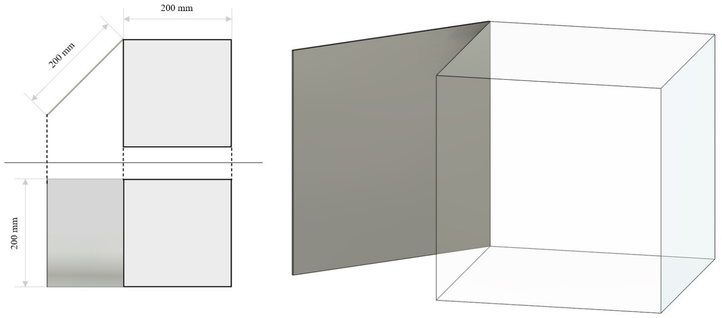

Figure 8.2: Image showcasing the mirror and scintillator, providing a frontal and top view on the left, accompanied by a 3D perspective on the right.

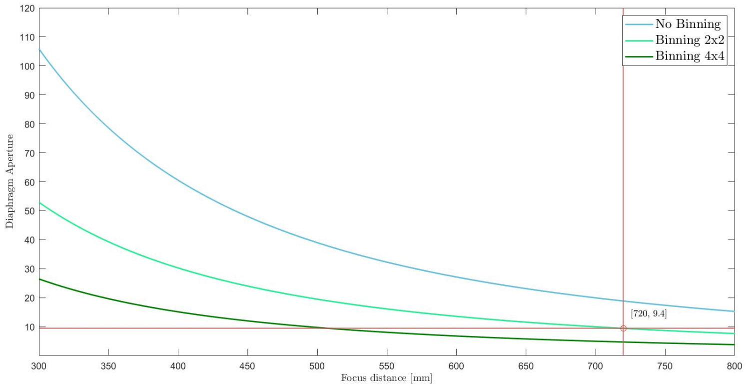

Figure 8.3: Trend of the diaphragm value at different binning settings. The selected focus distance (*720 mm*) is emphasized, along with the corresponding F/number at 2x2 binning (*9.4*).

8.2 Setup

An additional support structure for the mirror has been produced using a 3D printer (Figure 8.4). This support is positioned adjacent to the one accommodating the scintillator. The mirror is inserted into the guide and held vertically with the aid of another support applied to its rear side. The guide maintains a 45-degree angle with respect to the scintillator.

To evaluate the fidelity of the image reflected by the mirror, a series of characterizations have been performed using MATLAB. The objective was to determine whether the mirror faithfully reproduces the images without introducing artifacts, such as scratches or deviations from flatness. This evaluation focused on the reflective properties of the mirror, as any aberrations could potentially distort the reflected image and compromise overall image fidelity.

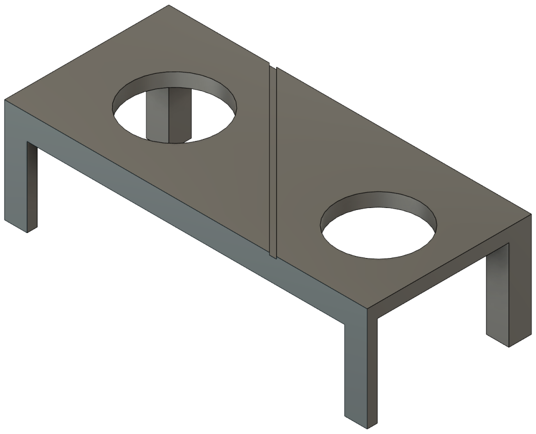

Figure 8.4: Image of the support for the mirror realized with Fusion 360.

In Figure 8.5 the mirror and the scintillator are depicted from the perspective of the sensor. The sensor is positioned at a distance of 720 mm from the proximal scintillator wall, and the camera is centered on the left wall. The mirror is inserted in the 45-degree guide, and graph paper is put on the corresponding wall of the scintillator to assess the positioning of the mirror.

Upon visual inspection of the image and considering the results from the previous evaluations, it can be affirmed that the mirror doesn't introduce any distortions. The lines remain straight, and the millimeter paper retains its accuracy in the reflection, as evidenced by the fidelity of the reflected graph paper. It is crucial to highlight that the absence of distortions in the mirror's reflection is contingent upon precise positioning.

The optical fidelity is maintained under the condition that the mirror is positioned precisely at a 45-degree angle relative to the scintillator and that it remains in a perfectly vertical position.

Figure 8.5: Image of the chosen setup. The scintillator and mirror are placed at 720 mm distance from the sensor. Graph paper was used to evaluate the position of the mirror.

The y-dimension of the scintillator is fully reflected, yet the x-dimension represented is 168 mm instead of the complete 200 mm. Consequently, visibility challenges arise, rendering portions with an x-coordinate equal to or greater than 68 mm imperceptible. To prevent the loss of crucial information it is important to consider employing a larger mirror that can fully accommodate the dimensions of the scintillator.

For the evaluation of the beam in the scintillator and the beam in the mirror, the two areas need to be identified on an image acquired in light conditions. This image needs to be taken before the measurements to prevent positioning errors.

In Figure 8.6 a paint at 101 mm depth can be seen, with the two segmented areas outlined.

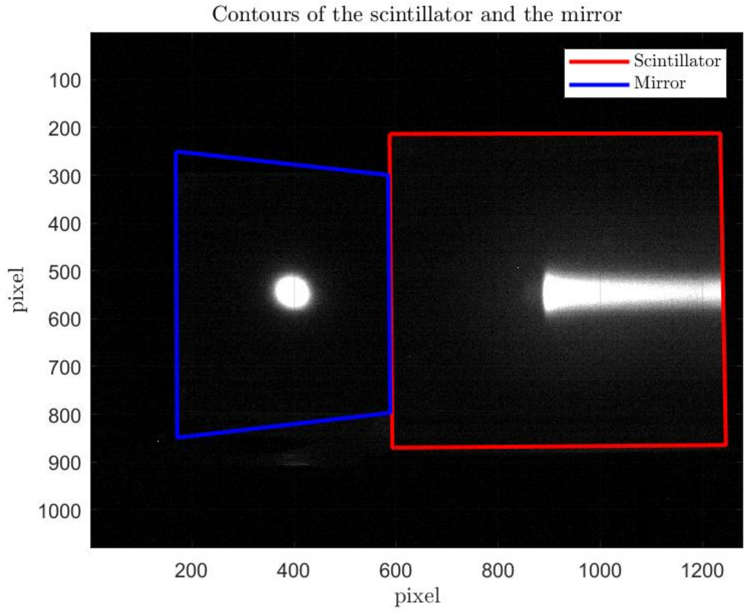

Figure 8.6: Image of the chosen setup with a paint at 101 mm depth, the image was saturated for visualization purposes. The scintillator and mirror were outlined to have a better understanding of the image.

8.3 Evaluation of the parameters

The distance of the sensor from the mirror and the scintillator was adjusted to 720 mm. Under these conditions, with a binning value of 2x2, the F/ number can be maintained at F/10. An algorithm developed in MATLAB is adopted to delineate the two distinct regions occupied by the scintillator and the mirror (Figure 8.6).

Due to the dimensions of the mirror (200 x 200 mm), the complete horizontal extent of the scintillator cannot be fully reflected. The obscured section of the scintillator spans a length of 32 ± 1 mm.

The K value in Table 8.1 indicates the mm/pixel correspondence. For the scintillator, it was determined by employing graph paper on its outer and inner faces, while for the mirror, it was calculated by placing the graph paper on the lateral face of the scintillator and observing its reflection in the mirror.

The K value for the mirror is determined to be 0.4 mm/pixel, indicating that each pixel corresponds to 0.4 millimeters.

Pictures of paints at different energy levels were captured, resulting in two distinct images. These images, one of the mirror and another of the scintillator, were obtained by cropping

Table 8.1: Table showcasing the K values of the scintillator and the mirror

K	Value [pixel/mm]
K_{prox} Scintillator	0.31 ± 0.01 mm/pixel
K_{dist} Scintillator	0.37 ± 0.01 mm/pixel
K Mirror	0.40 ± 0.01 mm/pixel

the original image. The cropping was based on the light image to define specific regions of interest.

Once these distinct images were obtained, the aim was to calculate the x- and y-coordinates of the center beam using the data from the mirror. By evaluating the integral of the mirror along both directions, it is possible to determine the index values corresponding to the maximum intensity. These index values, in turn, serve as the x- and y-coordinates of the center of the irradiated area. In Figure 8.8 a visual representation is provided.

In Figure 8.7 a representation of the beam in the mirror (left) and in the scintillator (right) can be seen. The coordinate system used for the evaluation is represented in red, while the lines represent the middle.

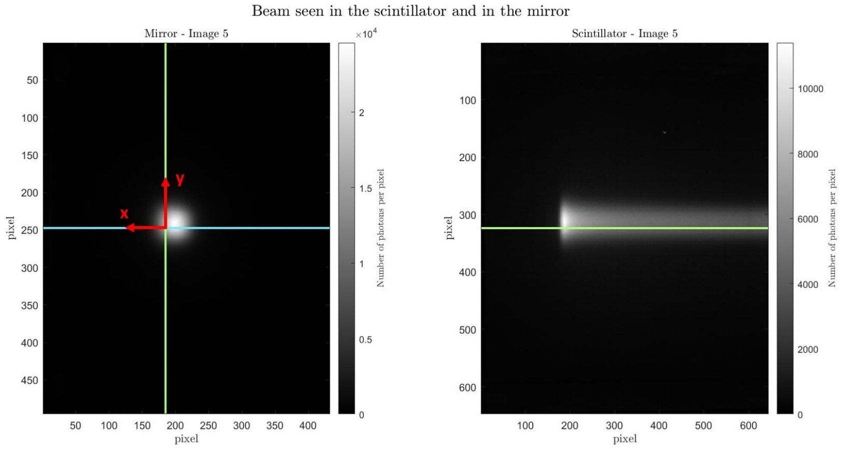

Figure 8.7: In the image, the paint (145 mm depth) can be seen in the mirror (left) and in the scintillator (right). For a better understanding of the coordinate system, it is shown on the mirror. The lines represent the center of the image.

For the correct evaluation of these values, it is essential to take the part of the scintillator that is not reflected in the mirror into consideration.

Table 8.2 presents the x- and y-coordinates (in millimeters) calculated at different depths. Ideally, if the setup were perfectly aligned, these coordinates should be zero, placing the center of the beam precisely in the middle of the mirror. The potential reasons for any deviation from this expected value are elaborated in Section 8.4.

Table 8.2: The table shows the depth of the paint and the x- and y-coordinates of the center. These values were calculated through Matlab.

Depth [mm]	Y coordinate [mm]	X coordinate [mm]
64	1.4	- 8.4
80	1.4	- 8.4
101	2.2	- 7.2
121	2.2	- 6.8
145	2.6	- 5.2

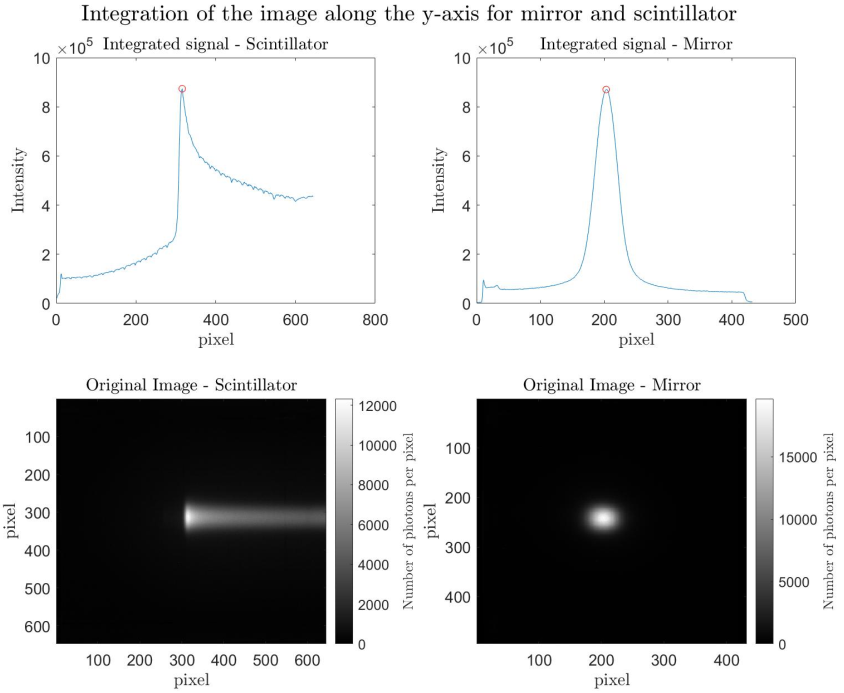

Figure 8.8: The figure illustrates the integration along the y-axis, featuring the scintillator on the left and the mirror on the right. Below, the original beam image is displayed. The depicted paint corresponds to an energy of 118.19 MeV (101 mm depth).

8.4 Results

Table 8.2 displays the depth at which the x and y-coordinates of the center were determined. Ideally, if the setup were perfectly aligned, these coordinates should be zero. However, the recorded values deviate from this ideal value, indicating potential alignment issues within the experimental setup.

The y-coordinates are found to be approximately 2 ± 0.5 mm. This suggests that the beam's y position has an offset from the ideal center, likely due to factors affecting the alignment of the beam with the center of the scintillator. The beam is aligned with the external case, but the relative precision between the scintillator and the case has not been validated yet.

On the other hand, the x-coordinates show more substantial deviations, averaging approximately -7.2 ± 1.3 mm. The significant difference in the x-coordinate values from the expected result may be attributed to several factors. Firstly, it could result from imperfect alignment of the mirror, causing a deviation from the intended 45-degree angle. Secondly, the discrepancy may stem from an alignment issue between the scintillator and the case.

In summary, the observed deviations in the x- and y-coordinates from the ideal zero values suggest alignment issues in the experimental setup.

Achieving precise alignment is essential for obtaining accurate measurements. Further adjustments and refinements may be necessary to address these deviations and improve the setup's accuracy.

Chapter 9

Evaluation of a different trigger modality

This chapter explores the potential of a different trigger modality to enhance the He-Check image acquisition process and to achieve a more precise synchronization of the timing events that determine the treatment duration.

9.1 Treatment administration at CNAO

To achieve efficient irradiation, the volume to be treated is divided into slices, and the pencil beam is utilized to paint each slice sequentially using scanning magnets.

The irradiation of the target is executed through spot scanning, where the beam is delivered through discrete beam positions (referred to as *spots*) defined in the treatment plan for each slice. This approach ensures an overall uniform dose profile.

A typical treatment at CNAO involves 60 spills distributed over 2-3 minutes. The duration of each spill varies depending on the treatment plan, ranging from a few milliseconds to over a second, with very high variability. There is an interval of 2-3 seconds required to extract another beam, resulting in an average of 60 spills.

The timing signal, delineating the 'beam on', is received by an Arduino, which converts it into a pulse train generating impulses with a specified period until the conclusion of the timing signal ('beam off).

After the timing signal transitions from HIGH to LOW, the Arduino ceases to generate the pulse train. This results in a pause where the sCMOS camera doesn't acquire frames until the next rising edge is detected by the Arduino.

To distinguish between two consecutive spills, a dark frame is acquired immediately after the timing signal goes LOW. The beam is then accelerated again and another pulse from the 'beam-on' signal is received, therefore the acquisition process resumes. The acquisition can be manually interrupted if the treatment concludes before reaching the specified length of the kinetic series.

9.2 External trigger modality

In the External Trigger modality, the camera and software are in a high state of readiness to accept a trigger from an external source [29].

The distinction between the external start and external trigger modes lies in their operational mechanism. In external start mode, a single external trigger event initiates the sequence, imposing a manually defined exposure period and kinetic series length. In contrast, the external trigger mode requires an external trigger for each frame within the kinetic series, making each frame dependent on an external trigger event.

In other words, the external trigger mode is triggered only by the rising edge of a HIGH (5 V) signal and acquires a single frame of a manually imposed duration. The following frame is acquired when another rising edge is detected. This is not the case in external start mode, where one rising edge triggers the entire kinetic series, acquiring a predetermined number of frames of a set duration. This modality does not provide the possibility to stop the acquisition once the timing signal is LOW, while the external trigger mode stops during this period and resumes acquiring again once the timing signal is HIGH.

The timing signal has only one rising edge, and this would lead to the acquisition of a single image in the chosen modality. To bypass this problem, an Arduino is triggered with the timing signal. The rising edge of the timing signal triggers the Arduino to start a pulse train that lasts as long as the timing signal is HIGH.

The sCMOS camera, set in the described modality, is able to acquire a number of images that depend on the chosen exposure time and the actual duration of the timing signal, which is not known beforehand. It is important to note that there is still the need to manually impose the exposure time and the kinetic series length.

Using this approach ensures that the camera is activated only for a certain period, aligning with the period during which the timing signal is in a high state, corresponding to the administration of the treatment.

9.3 Characterization

On average, the number of particles per treatment is equal to 1.7×10^9 carbon ions and 5.2×10^{10} protons, while the average number of particles per slice will be 3.3×10^7 for carbon ions and 1.3×10^9 for protons.

The number of spots per treatment is 3×10^4 for carbon ions and 1×10^4 for protons, meaning an average of 600 spots per slice for carbon ions and 238 spots per slice for protons. These values are recapped in Table 9.1 for more clarity.

Table 9.1: Statistical analysis of the irradiation performed on patients at CNAO

Number of particles per treatment	1.7×10^9 for Carbon Ions 5.2×10^{10} for Protons
Number of particles per slice	3.3×10^7 for Carbon Ions 1.3×10^9 for Protons
Number of spots per treatment	3.0×10^4 for Carbon Ions 1.0×10^4 for Protons
Number of spots per slice	6.0×10^2 for Carbon Ions 2.4×10^2 for Protons

Each slice is composed at least of one spill. It is possible to reconstruct the correspondence between spill and slice through the data produced by the DDS during the treatment. The DDS saves a file for each spill with an identifier that refers to each slice.

9.3.1 Exposure time

In the selected modality, the camera's exposure time must be manually set, considering the maximum frame rate of the sCMOS camera and the average duration of the timing signal during different treatments.

In the global shutter modality, the maximum frame rate is 50 Hz, corresponding to a period of 20 ms. Consequently, the exposure time can be chosen within the range of 20 ms and 1000 ms, considering an average spill duration of 1 second. This range means that there will be between 1 and 50 acquisitions for each spill.

The number of possible acquisitions needs to be carefully evaluated, considering that a lower exposure time will result in more images, requiring additional memory allocation. However, it would also lead to a clearer signal since it would acquire a smaller number of spots per frame than those acquired using a higher exposure time.

Choosing to impose a low exposure time has the downside of having more dead time between frames, resulting in a higher loss of information.

It's also essential to consider acquiring a dark frame between different spills to separate them correctly. While it is possible to access the metadata of the kinetic series through a Matlab program, the inclusion of a dark frame adds an extra layer of security.

9.3.2 Pulse Train Period

The period of the pulse train generated by Arduino is another critical parameter. Considering that the maximum frequency at which an Arduino can trigger pulses is 16 MHz and that the dead time[1] between frames is 150 μs, the pulse train should be configured with a period falling within this time range.

Figure 9.1 illustrates a possible system characterization, assuming a 200 ms exposure time and an average spill duration of 1 second. The pulse train generated by Arduino is not to scale for visualization purposes. It can be observed that the dead time between two frames will lead to information loss, which will be discussed in the following section.

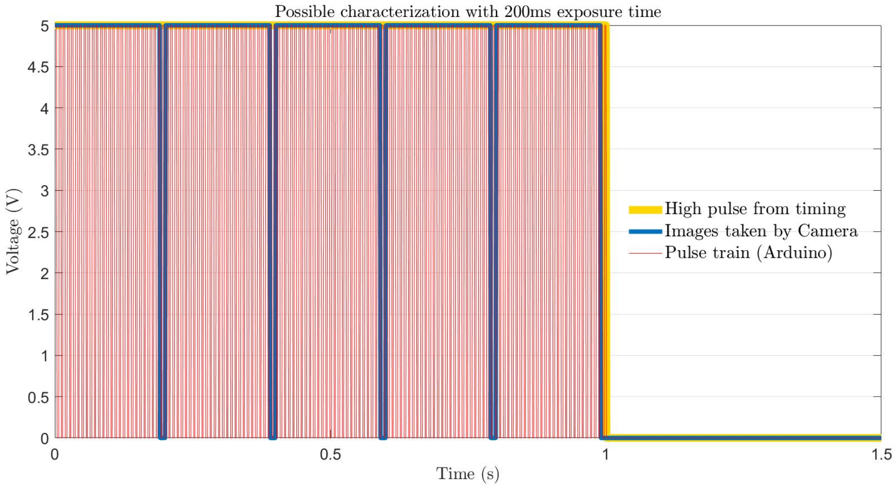

Figure 9.1: Image of a possible characterization with an exposure time of 200 ms and an average spill duration of 1 s. The pulse train generated by Arduino is not in scale for visualization purposes.

---

[1] Referring to the period after each event during which the system cannot record another event.

9.4 Analysis of the signal loss

Adding to the dead time between different acquisitions, additional delays are introduced due to the passage through Arduino. Therefore, there will be a delay introduced by the transition from the timing signal to Arduino and a delay from the passage of the pulse train to the actual moment when the camera captures an image.

These delays have been characterized using an oscilloscope and have the following duration:

- Delay between images, also called dead time, equal to 150 μs.
- Delay between timing signal and the start of the pulse train coming from Arduino, equal to $13.1 \pm 0.7 \mu s$.
- Delay between the pulse Train and the time in which the camera will acquire the frame, equal to $14 \pm 3 \mu s$.

Let n represent the average number of pictures taken during a spill. This value depends on both the specific treatment, that leads to fluctuating average durations of the timing signal, and the type of particle used.

- The dead time will cause a delay of $150 \times (n - 1)$ μs.
- The second delay listed will cause a delay for each image taken equal to $13.1 \times n$ μs.
- The third delay will appear once for every spill and will be equal to 14 μs.

To evaluate the total delay, the previously described delays must be multiplied by the average number of spills (N), which will be considered to be around 60.

The total lost information can be calculated using the following formula:

$$\text{Lost Information}(\mu s) = N \cdot [150 \cdot (n - 1) + 13.1 \cdot n + 14] \tag{9.1}$$

As depicted in Figure 9.2, signal loss consistently remains below an acceptable value of 1% for various numbers of images acquired per spill. The graph presents percentage and time values corresponding to different quantities of images acquired per spill.

Figure 9.3 highlights that the main source of signal loss arises from the dead time between pictures, a challenge that could potentially be mitigated with a different camera. However, it's worth noting that the signal loss is minimal, and given the low percentage, there may be no immediate need for mitigation.

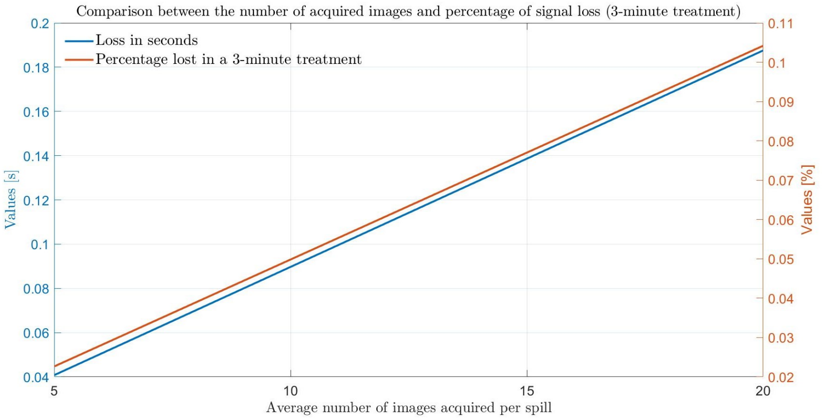

Figure 9.2: The number of acquired images is compared to the loss in seconds and the percentage of signal loss (referred to a 3-minute treatment).

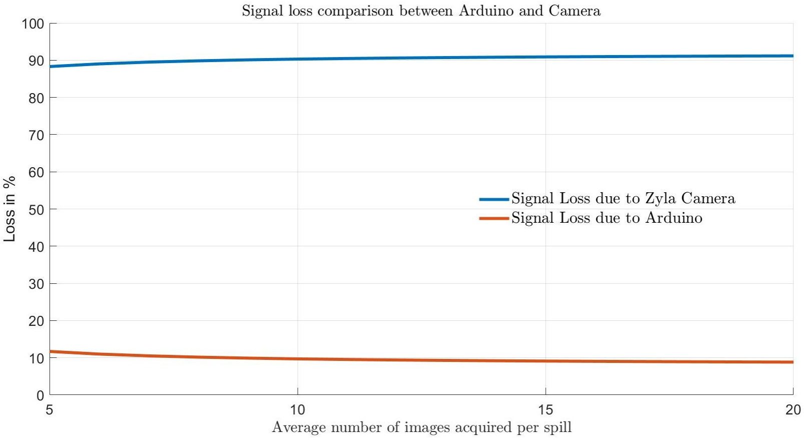

Figure 9.3: Comparison in percentage between the signal loss caused by the Zyla camera and Arduino.

9.4.1 Analysis of the noise with different binning values

After selecting the external trigger mode, an assessment of the noise at different binning values was conducted. The noise value was calculated in complete darkness using a kinetic series of 200 images per binning modality, and the results can be seen in Table 9.2.

If the need arises to consider different binning values, it is essential to take these noise values into account.

Table 9.2: Table showcasing the different values of noise with respect to the chosen binning values.

Binning Value	Noise [ADU]
1x1	118 ± 10
2x2	172 ± 22
3x3	261 ± 46
4x4	387 ± 75
8x8	1249 ± 273

9.5 First evaluations

A Spread-Out Bragg Peak (SOBP) acquisition was performed using various energies corresponding to different depths in water (64, 80, 101, 121, and 145 mm). The camera was configured in external trigger mode, with an exposure time of 200 ms for each acquisition.

During the acquisition sequence, black frames are automatically inserted by Andor Solis in the saved dataset. This is a consequence of manually setting the acquisition number; when the set number exceeds the actual acquisitions, the software automatically inserts black frames for the remaining acquisitions.

Every time the camera inserts a black frame, the mean value of the inserted frame is 11 ± 1 ADU. This standardized value makes it possible to identify and subsequently exclude the black frames from the analysis, ensuring that only valid data is considered.

These frames also function as separators between separate acquisitions when the signal is detected. The images between the separator frames were subsequently grouped and summed.

The ROI representing the mirror and the one representing the scintillator were derived from the light image acquired at the beginning of the acquisition, and they were subsequently employed to accurately crop the images.

The obtained images were integrated along the columns, and the peak value was utilized to determine both the range (using the ROI of the scintillator) and the center of the beam as reflected in the mirror (utilizing the ROI of the mirror). This process is illustrated in Figure 9.4, and the resulting values for the range calculation and the calculation of the coordinates of the center of the paint in the mirror can be found in Table 9.3.

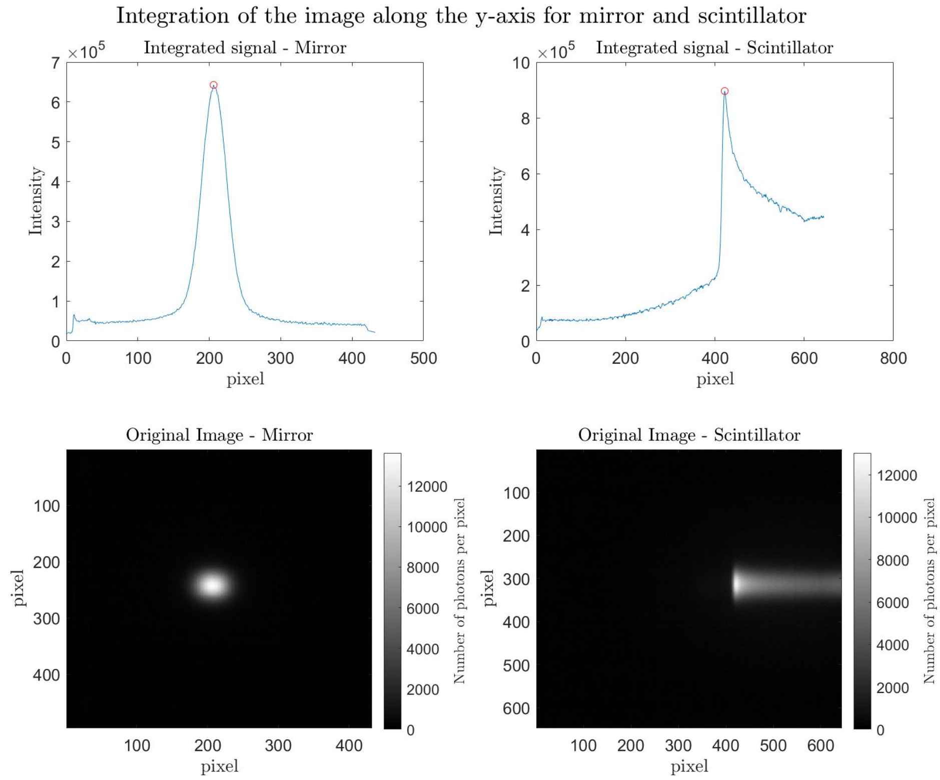

Figure 9.4: In this image the integrated signal of the ROI representing the mirror and the scintillator (upper row) and the original image seen from the camera (lower row), at 80 mm depth, can be seen. The red dots represent the maximum value.

Table 9.3: Mean value of the range of paints taken at different energies and the center coordinates of the paint as seen in the mirror.

Depth [mm]	Range calculation [mm]	X coordinate [mm]	Y coordinate [mm]
64	71.3	-8.6	1.4
80	84.9	-8.6	1.4
101	102.6	-7.1	2.2
120	119.8	-7.1	1.4
145	140.5	-5.8	1.4

9.6 Simulation of an operational setup

In this section, the previously described acquisition method was utilized to reconstruct an obstacle introduced into the radiation field. Instead of irradiating the scintillator without any obstacle in the beam's path, a flask filled to half its capacity was positioned within the radiation path.

The subsequent simulations involve testing the new setup with a more realistic geometry. The objective is to assess the sensitivity of the method to small variations in the target.

9.6.1 Experimental Setup

The experimental setup, represented in Figures 9.5 and 9.6, is composed of a flask, filled with water to its midpoint and six slabs (Water-equivalent RW3 slab phantoms) with a thickness of one centimeter each. Three slabs are situated before the flask, and the other three are placed after it. Another empty flask was used as a support for the filled flask, but will not be seen in the chosen radiation field.

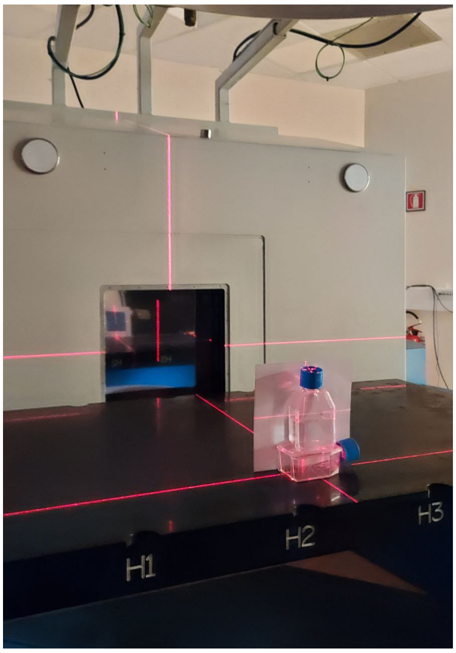

Figure 9.5: The setup of the measurement shows the flask filled to its half-point, positioned on another empty flask, which will not be directly irradiated.

The flask was irradiated with proton paints of varying energies and particle numbers, each consisting of 35x35 spots with a 2 mm step.

The number of protons used in each spot was chosen to be either 8e5 or 8e6. The

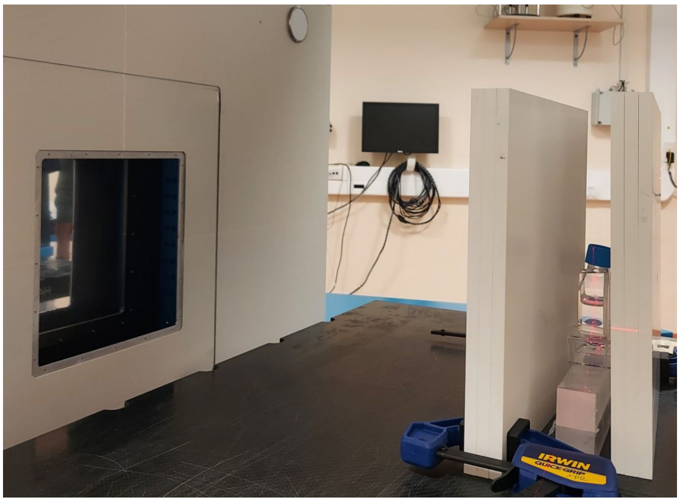

Figure 9.6: The setup of the measurement with the 3 slabs (each 1 cm of thickness) before and after the flask.

selection of the first value aligns with real-case scenarios, maintaining a 10% ratio between helium particles (simulated with protons) and carbon particles in the mixed beam. The second value was opted for to enhance the contrast against the background in these initial measurements. The resulting images are represented in Figure 9.7.

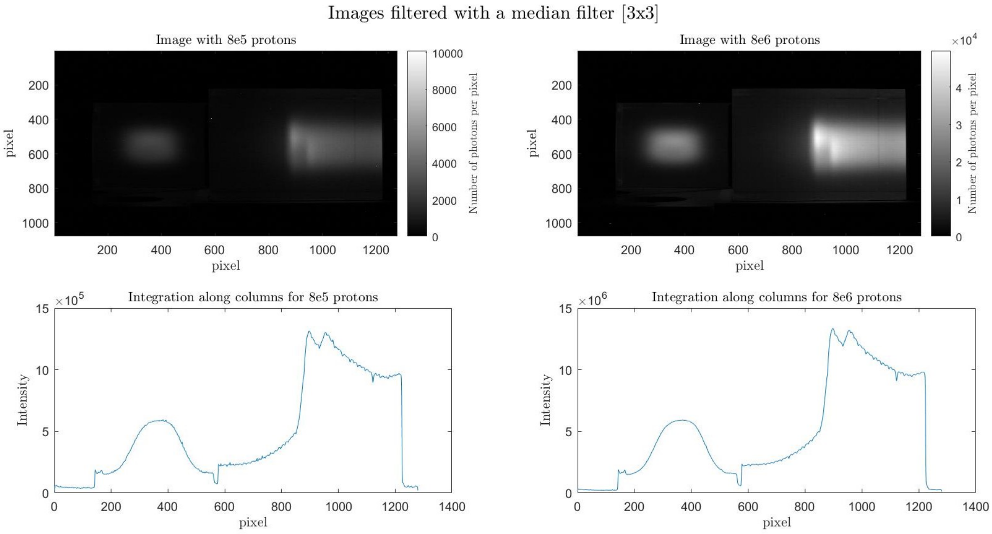

Figure 9.7: Comparison between the integration along columns of a paint with 8e5 protons and a paint with 8e6 protons per spot. The difference is visible.

The images were summed after doing what was previously described in section 9.5. The image was filtered with the use of a median filter and a kernel of [5x5].

In Figure 9.8, the image on the left represents the Region of Interest (ROI) within the mirror, while the image on the right depicts the ROI within the scintillator.

Notably, in the image on the right, the impact of the flask, filled to half its capacity, is evident. The light peak in the lower part of the flask, containing water, is visibly shifted back compared to the empty upper part. This configuration results in a differential path length for the beam passing through the water-filled section.

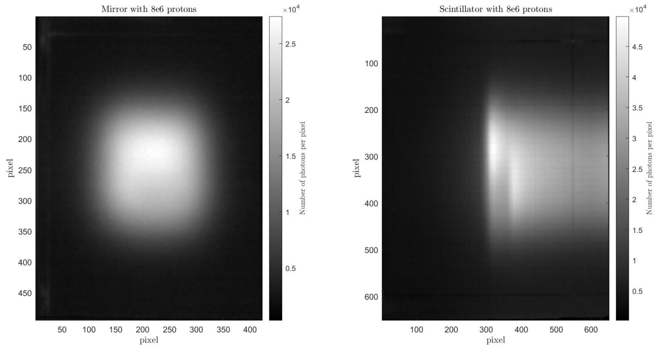

Figure 9.8: The image on the left represents the ROI of the mirror and on the right, the ROI of the scintillator is represented. The paint is composed of 35x35 spots with 8e6 protons each. From the image on the right, the difference of the path in water and air (in the flask) can be seen clearly.

9.6.2 Subtraction

In Figure 9.9, the subtraction between the ROIs representing the mirror and the scintillator is illustrated. These subtractions were initially carried out between two images acquired with the same proton beam and an unaltered setup. Following this, the subtraction was conducted between two images acquired with the same proton beam, but with the introduction of a 4 mm shift in the setup. The entire setup was shifted by moving the treatment table by 4 mm. In Figure 9.10, the impact of a setup shift of 8 mm is depicted.

In Figures 9.11 and 9.12, the results of subtraction between images with a 4 mm shift and an 8 mm shift of the flask and slab are presented. These visualizations highlight the impact of spatial shifts on the interaction between the mirror and the scintillator.

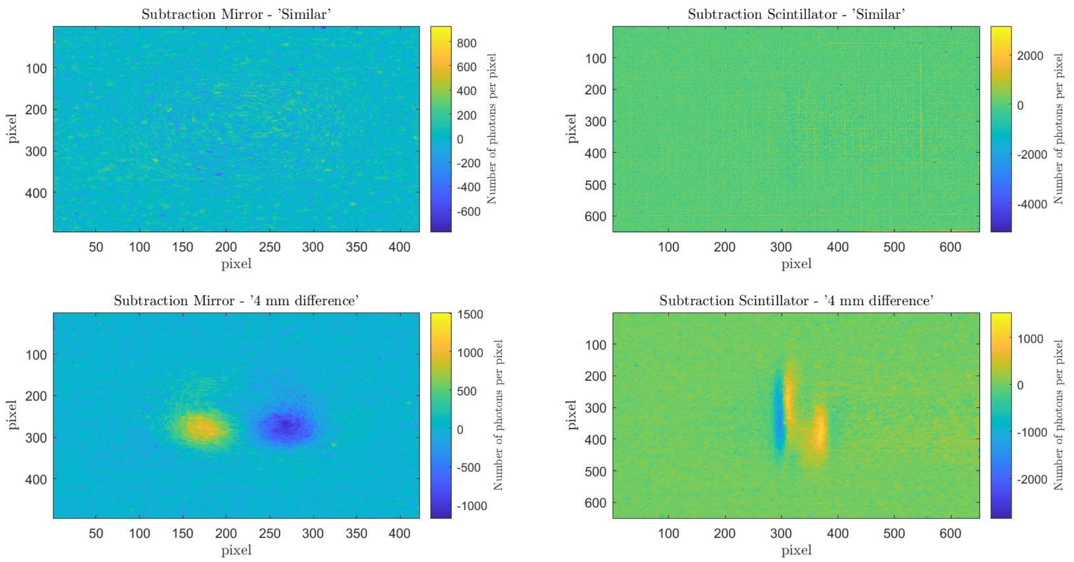

Figure 9.9: On the upper a lower row the subtraction of the ROI representing the mirror (left) and the scintillator (right) can be seen. On the upper row, the subtraction was done between 'identical images', while on the lower, the setup comprising the flask and the slabs were shifted 4 mm.

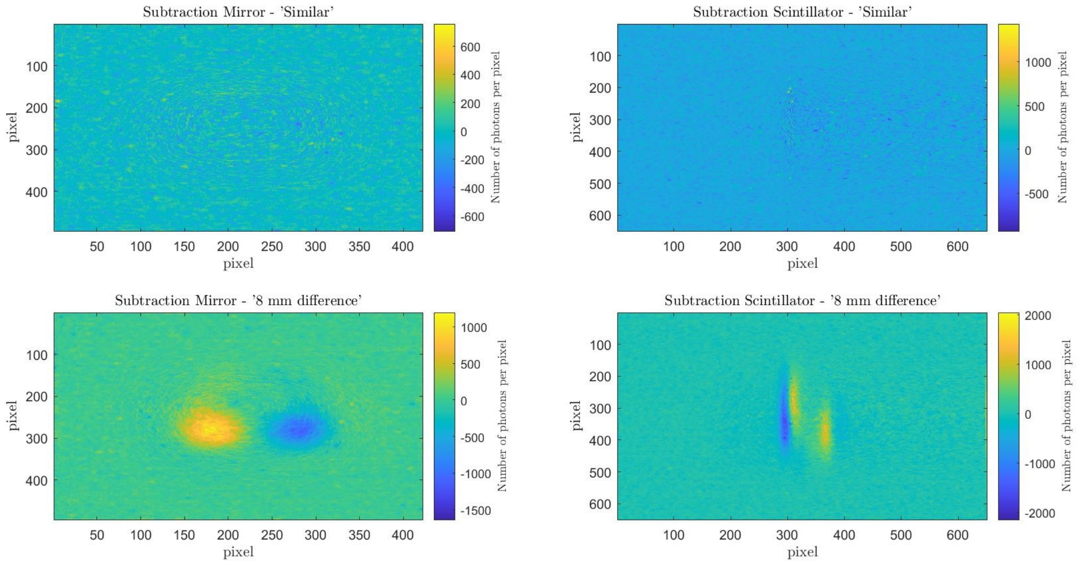

Figure 9.10: On the upper a lower row the subtraction of the ROI representing the mirror (left) and the scintillator (right) can be seen. On the upper row, the subtraction was done between 'identical images', while on the lower, the setup comprising the flask and the slabs were shifted 8 mm.

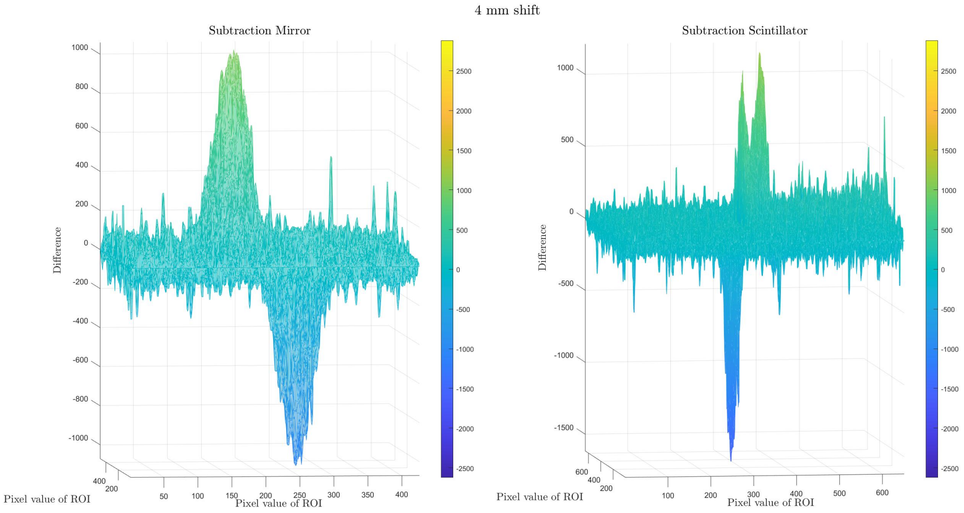

Figure 9.11: The subtraction is displayed between images with a 4 mm shift in the setup. On the left image, a 3D representation of the ROI of the mirror is visible, while on the right, a 3D representation of the ROI of the scintillator is presented.

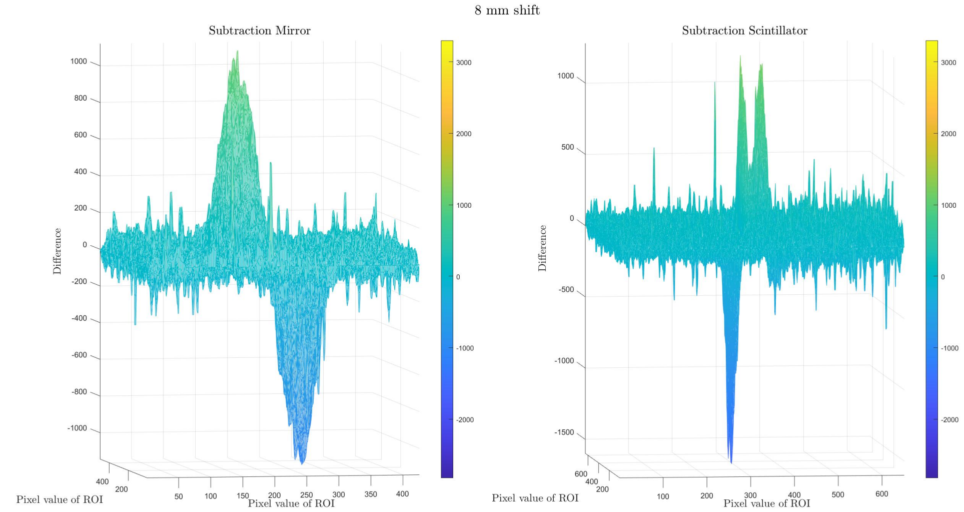

Figure 9.12: The subtraction is displayed between images with an 8 mm shift in the setup. On the left image, a 3D representation of the ROI of the mirror is visible, while on the right, a 3D representation of the ROI of the scintillator is presented.

9.7 Advancements in He-Check Image Acquisition through External Trigger Modality

In this chapter, an examination of the potential advantages associated with the adoption of the external trigger modality for He-Check image acquisition has been conducted.

The external trigger modality effectively addresses challenges tied to synchronizing image capture with the treatment process, specifically with the timing signal. This modality provides flexibility in initiating and terminating image acquisition, ensuring precise alignment with the treatment timeline.

System characterization has revealed critical considerations, including exposure time and pulse train period. These parameters must be carefully chosen to balance the number of acquired images, memory utilization, and signal clarity. A comprehensive understanding of the implications of delays and signal loss is crucial for optimizing the external trigger modality setup.

In summary, the external trigger modality emerges as a promising approach for enhancing the precision and efficiency of He-Check image acquisition in the context of radiation therapy. It allows for better synchronization with treatment events and offers opportunities for further refinement and optimization to improve the overall quality of acquired images.

Chapter 10

Conclusion

Hadrontherapy, a cutting-edge approach in cancer treatment, has gained significant traction for its precision and effectiveness in targeting malignant cells while sparing healthy tissue.
However, despite its advantages, the field faces challenges in terms of treatment delivery accuracy. Real-time verification techniques have emerged as a solution to reduce uncertainties by providing dynamic feedback on the ion beam range within the patient during the treatment session.

The purpose of the work carried out at the Centro Nazionale di Adroterapia Oncologica (CNAO), was to implement a system for the verification of the variation in the patient's anatomy during treatment. The system, called He-Check, is based on the joint acceleration of a fraction of helium ions and the primary ^{12}C beam used for therapy. While the helium, present in a quantity equal to 10% of the carbon, completely crosses the patient, reaching a scintillator, the carbon beam is used for therapy.
The scintillator and a Zyla 5.5 sCMOS camera allow for the measurement of the residual range of helium, enabling the reconstruction of the thickness traversed by the beam in the patient. The aim is to verify the presence of configurational changes in the irradiated volume.

By integrating the light emitted from the scintillator, it was possible to determine the range and assess the system's repeatability through image subtraction.

The introduction of a new element, a mirror, has expanded 2D measurements into the possibility of 3D measurements, enhancing overall capabilities.

Different acquisition methods were explored, using an Arduino coupled with both the camera and the timing signal of the beam delivery.

Through measurements and image processing, the following results have been obtained:

- The system's repeatability has been assessed, and the potential for post-processing, capable of eliminating noise and hot pixels after image acquisition, has been discussed. The system demonstrated the capability to distinguish a 2 mm difference in depth.
- To evaluate the residual range of particles, it is necessary to know a priori the transverse position of the beam in the scintillator. This can be determined by introducing a mirror into the setup.
- The advantages of a different acquisition modality, which has not been used before, were explored. The camera, set in external trigger mode, was coupled with an Arduino and the timing signal of the beam delivery system.
  This approach allows flexibility in initiating and stopping image acquisition in response to the timing signal, ensuring precise alignment with the treatment timeline. The system was able to capture a slice, minimizing signal loss to an extremely low percentage.

This work demonstrates the feasibility of implementing a dose distribution verification system for use during hadron therapy treatments. The analysis of repeatability and the integration of a mirror into the setup to measure the transverse position of the beam have provided valuable insights. These enhancements contribute to the ongoing improvement and increased precision of the system.

Furthermore, the use of the external trigger mode has enabled the synchronization of image acquisition with the timing signal of the beam delivery. This innovative approach holds promise for further improvement and opens avenues for more advanced and precise measurements in the future.

10.1 Future improvements

Setup improvements

While the current setup serves its purpose, there is room for refinement to enhance its performance. A redesign of the support structure, where various elements are mounted, could mitigate potential positioning errors, ensuring improved repeatability.

Moreover, to augment functionality, the incorporation of internal lighting within the box would enable the acquisition of light images without the need to open the case.

Additionally, integrating LEDs for calibration purposes could contribute to optimizing the system's accuracy and reliability.

Treatment plan adaptation

The parameters, including the exposure time of the sCMOS, have been configured based on an average treatment plan. However, considering the substantial variations in treatments across individuals, it is imperative to customize this modality to accommodate the diverse nature of different treatment plans.

List of Figures

List of Tables

Bibliography

[1] Marco G Pullia. Synchrotrons for hadrontherapy. *Reviews of accelerator science and technology*, 2(01):157–178, 2009.

[2] Javier Balibrea-Correa, Jorge Lerendegui-Marco, Victor Babiano-Suarez, César Domingo-Pardo, Ion Ladarescu, Carlos Guerrero, Teresa Rodríguez-González, Maria del Carmen Jiménez-Ramos, and Begoña Fernández-Martínez. First in-beam tests on simultaneous pet and compton imaging aimed at quasi-real-time range verification in hadron therapy. In *EPJ Web of Conferences*, volume 261, page 05002. EDP Sciences, 2022.

[3] Davide Mazzucconi, Stefano Agosteo, Michele Ferrarini, Luigi Fontana, Valeria Lante, Marco Pullia, and Simone Savazzi. Mixed particle beam for simultaneous treatment and online range verification in carbon ion therapy: Proof-of-concept study. *Medical physics*, 45(11):5234–5243, 2018.

[4] Wollina U Lotti J Tchernev G Lotti T Gianfaldoni S, Gianfaldoni R. An overview on radiotherapy: From its history to its current applications in dermatology. *Open Access Maced J Med Sci*, 2017.

[5] Coutard H. Principles of x-ray therapy of malignant disease. *Lancet*, 1934.

[6] L S Taylor. History of the international commission on radiological protection (icrp). *Health Phys*, 1958.

[7] Mullett L Fry DW, Harvie RB. A travelling-wave linear accelerator for 4-mev electrons. *Nature*, 1948.

[8] Riccardo Ridolfi. *Adroterapia: principi e applicazioni.* PhD thesis, 09 2015.

[9] Emmanouil Fokas, Gerhard Kraft, Hanxiang An, and Rita Engenhart-Cabillic. Ion beam radiobiology and cancer: time to update ourselves. *Biochimica et Biophysica Acta (BBA)-Reviews on Cancer*, 1796(2):216–229, 2009.

[10] Laurent Kelleter. *A Scintillator-Based Range Telescope for Particle Beam Radiotherapy.* PhD thesis, UCL (University College London), 2021.

[11] Ugo Amaldi, Manjit Dosanjh, Jacques Balosso, Jens Overgaard, and Brita Sørensen. A facility for tumour therapy and biomedical research in south-eastern europe. 09

2019.

[12] Lien Ai Pham-Huy, Hua He, and Chuong Pham-Huy. Free radicals, antioxidants in disease and health. *International journal of biomedical science: IJBS*, 4(2):89, 2008.

[13] Administrator. PTCOG - Facilities in Operation — ptcog.site. `https://ptcog.site/index.php/facilities-in-operation-public`. [Accessed 13-10-2023].

[14] Hwa Kyung Byun, Min Cheol Han, Kyungmi Yang, Jin Sung Kim, Gyu Sang Yoo, Woong Sub Koom, and Yong Bae Kim. Physical and biological characteristics of particle therapy for oncologists. *Cancer Research and Treatment: Official Journal of Korean Cancer Association*, 53(3):611–620, 2021.

[15] Jan Unkelbach and Harald Paganetti. Robust proton treatment planning: physical and biological optimization. In *Seminars in radiation oncology*, volume 28, pages 88–96. Elsevier, 2018.

[16] Oliver Jäkel, Günther H Hartmann, Christian P Karger, Peter Heeg, and Jürgen Rassow. Quality assurance for a treatment planning system in scanned ion beam therapy. *Medical physics*, 27(7):1588–1600, 2000.

[17] Uwe Schneider and Eros Pedroni. Proton radiography as a tool for quality control in proton therapy. *Medical physics*, 22(4):353–363, 1995.

[18] Introduction to PET Physics: The physical principles of PET — depts.washington.edu. `https://depts.washington.edu/imreslab/from%20old%20SITE/pet_intro/intro_src/section2.html`. [Accessed 18-09-2023].

[19] I Rinaldi, S Brons, J Gordon, R Panse, B Voss, O Jäkel, and K Parodi. Experimental characterization of a prototype detector system for carbon ion radiography and tomography. *Physics in Medicine & Biology*, 58(3):413, 2013.

[20] Julia Telsemeyer, Oliver Jäkel, and Mária Martišíková. Quantitative carbon ion beam radiography and tomography with a flat-panel detector. *Physics in Medicine & Biology*, 57(23):7957, 2012.

[21] K Parodi. Heavy ion radiography and tomography. *Physica medica*, 30(5):539–543, 2014.

[22] DAVIDE MAZZUCCONI. Hecheck: studio di fattibilità di un sistema di verifica in tempo reale della posizione del paziente durante un trattamento adroterapico. 2016.

[23] CECILIA LANDINI. Simulazioni numeriche per la validazione del metodo he-check su casi clinici. 2018.

[24] Lorenzo Cantù. A system for verifying the repeatability of dose delivery based on simultaneous acceleration of helium and carbon ions. 2023.

[25] Ahmet POLATOĞLU and İmam Can ÖZKESEN. Working principles of ccd and cmos sensors and their place in astronomy. *Journal of Anatolian Physics and Astronomy*, 2(1):51–59, 2022.

[26] Christophe Dujardin and Matthieu Hamel. Introduction—overview on plastic and inorganic scintillators. *Plastic Scintillators: Chemistry and Applications*, pages 3–33, 2021.

[27] S. Gupta e Y. Mao. *Nano Scintillator-Book*. 2020.

[28] Richard Crisp. Digital camera design, part 5: Basic noise considerations for cmos image sensors, Jan 2021.

[29] Andor: Oxford Instruments. *Zyla hardware user guide*, v1.7 edition, 2018.

[30] AK Jha, S Mithun, V Jaiswar, UB Sherkhane, NC Purandare, K Prabhash, V Rangarajan, A Dekker, L Wee, and A Traverso. Repeatability and reproducibility study of radiomic features on a phantom and human cohort. *Scientific reports*, 11(1):2055, 2021.

[31] IDS Imaging Development Systems GmbH. Hot pixels — 1stvision.com. `https://www.1stvision.com/cameras/IDS/IDS-manuals/uEye_Manual/hw_hotpixel.html`. [Accessed 13-11-2023].

[32] Cornelius T Leondes. *Multidimensional Systems: Signal Processing and Modeling Techniques: Advances in Theory and Applications*. Elsevier, 1995.

Appendix A

MATLAB CODES

Post-processing of the images and subtraction between same images

```
% REPEATABILITY
% Loading of images, subtraction backgorund and conversion int (PAINT)
% Insert the adequate Path

folderPath_181 = 'C:\...\Misure_12_Agosto\solo_scintillatore_630_mm\paint_2e6_181_mm_rip';
folderPath_101 = 'C:\...\Misure_12_Agosto\solo_scintillatore_630_mm\paint_2e6_101_mm_rip';
folderPath_50 = 'C:\...\Misure_12_Agosto\solo_scintillatore_630_mm\paint_2e6_50_mm_rip';


fileList_181 = dir(fullfile(folderPath_181, '*.tif'));
fileList_101 = dir(fullfile(folderPath_101, '*.tif'));
fileList_50 = dir(fullfile(folderPath_50, '*.tif'));

numImages = numel(fileList_50); %Number of images

% Background Image
myFolderBkg = 'C:\...\Misure_12_Agosto\solo_scintillatore_630_mm\No_beam_3s.tif';
fullFileName = fullfile(myFolderBkg); Bkg{1} = imread(fullFileName);

Paint_181 = cell(numImages, 1); Paint_101 = cell(numImages, 1); Paint_50 = cell(numImages, 1);
% Loop through each TIFF file and read the images
for i = 1:numImages
    %181
    filename_181 = fullfile(folderPath_181, fileList_181(i).name);
    image_181 = imread(filename_181);
    Paint_181{i} = image_181; Paint_181{i} = Paint_181{i}-Bkg{1};
    %101
    filename_101 = fullfile(folderPath_101, fileList_101(i).name);
    image_101 = imread(filename_101);
    Paint_101{i} = image_101; Paint_101{i} = Paint_101{i}-Bkg{1};
    %50
    filename_50 = fullfile(folderPath_50, fileList_50(i).name);
    image_50 = imread(filename_50);
    Paint_50{i} = image_50; Paint_50{i} = Paint_50{i}-Bkg{1};
end

%Thanks to cellfun I can convert the image from uint to int,
```

```
%necessary to subtract them. With uint every negative value is put to 0

Paint_181 = cellfun(@int16, Paint_181 , 'UniformOutput', false);
Paint_101 = cellfun(@int16, Paint_101 , 'UniformOutput', false);
Paint_50 = cellfun(@int16, Paint_50 , 'UniformOutput', false);

%Light image fo the evaluation of the ROI -> ROI_y and ROI_x need to be set
myFolderBkg = 'C:\...\Misure␣12␣Agosto\solo␣scintillatore␣630␣mm\Immagine␣in␣luce.tif';
fullFileName = fullfile(myFolderBkg); Light = imread(fullFileName);

%% ROI
ROI_y = (182:924); ROI_x = (197:944);
ROI_181={}; ROI_101={}; ROI_50={};
for i=1:numImages
    ROI_181{i,1}= Paint_181{i,1}(ROI_x,ROI_y);
    ROI_101{i,1}= Paint_101{i,1}(ROI_x,ROI_y);
    ROI_50{i,1}= Paint_50{i,1}(ROI_x,ROI_y);
end

%% REMOVE THE PEAKS FROM THE ORIGINAL IMAGE
thresh_181=1.5; thresh_101=3; thresh_50=4; % MANUALLY SET THRESHOLD VALUE

figure % Figure for 181 mm
for i = 1:numImages
    subplot(1, numImages, i)

    mean_Paint(i) = mean(max(ROI_181{i}));  % For thresholding, evaluate max values to find peaks
    threshold(i) = mean_Paint(i) * thresh_181;  % WARNING: Manually set threshold value
    plot(max(ROI_181{i})); hold on; yline(threshold(i)); hold on

    ROI_post_peak{i} = ROI_181{i}(:, 200:end); ROI_pre_peak{i} = ROI_181{i}(:, 1:199);
    Paint_ind = find(ROI_post_peak{i} > threshold(i));
    ROI_181_new_post{i, 1} = ROI_post_peak{i}; ROI_181_new_post{i, 1}(Paint_ind) = 0;
    ROI_181_new{i, 1} = [ROI_pre_peak{i}, ROI_181_new_post{i}];

    % Find the index and value of the global maximum to plot it
    x_max_global(i) = max(max(ROI_181_new{i}));
    [max_values_181(i), column_indices_181(i)] = max(max(ROI_181_new{i}));
    plot(column_indices_181(i), max_values_181(i), 'ro', 'DisplayName', 'Data␣Point');
    % Add a label to the point
    label = sprintf('[%d,␣%d]', max_values_181(i), column_indices_181(i));
    % Format the label with the coordinates
    text(column_indices_181(i) - 170, max_values_181(i) - 60, label, 'FontSize', 14, 'Interpreter', 'latex');
    % Adjust the position and font size of the label
    hold on; plot(max(ROI_181_new{i}))
    title(['Image␣', num2str(i)], 'Interpreter', 'latex')
    xlabel('Pixel␣value␣of␣ROI', 'Interpreter', 'latex');  ylabel('Intensity␣value', 'Interpreter', 'latex')
    sgtitle('Peak␣Removal␣for␣ROI␣at␣181␣mm', 'Interpreter', 'latex')
end

figure  % Figure for 101 mm
for i = 1:numImages
    subplot(1, numImages, i)
    mean_Paint(i) = mean(max(ROI_101{i}));
    threshold(i) = mean_Paint(i) * thresh_101;  % WARNING: Manually set threshold value
    plot(max(ROI_101{i})); hold on
```

```
    yline(threshold(i), 'Linewidth', 1.5); hold on

    % For this, a different approach is needed - divide them into two parts
    ROI_post_peak{i} = ROI_101{i}(:, 450:end); ROI_pre_peak{i} = ROI_101{i}(:, 1:449);
    Paint_ind = find(ROI_post_peak{i} > threshold(i));
    ROI_101_new_post{i, 1} = ROI_post_peak{i}; ROI_101_new_post{i, 1}(Paint_ind) = 0;
    ROI_101_new{i, 1} = [ROI_pre_peak{i}, ROI_101_new_post{i}];

    x_max_global(i) = max(max(ROI_101_new{i}));
    [max_values_101(i), column_indices_101(i)] = max(max(ROI_101_new{i}));
    plot(column_indices_101(i), max_values_101(i), 'ro', 'DisplayName', 'Data␣Point');
    label = sprintf('[%d,␣%d]', max_values_101(i), column_indices_101(i));
    text(column_indices_101(i) - 170, max_values_101(i) - 60, label, 'FontSize', 14, 'Interpreter', 'latex');
    hold on; plot(max(ROI_101_new{i}))
    title(['Image␣', num2str(i)], 'Interpreter', 'latex')
    xlabel('Pixel␣value␣of␣ROI', 'Interpreter', 'latex'); ylabel('Intensity␣value', 'Interpreter', 'latex')
    sgtitle('Peak␣Removal␣for␣ROI␣at␣101␣mm', 'Interpreter', 'latex')
end

figure % Figure for 50 mm
for i = 1:numImages
    subplot(1, numImages, i)

    mean_Paint(i) = mean(max(ROI_50{i}));
    threshold(i) = mean_Paint(i) * thresh_50;  % WARNING: Manually set threshold value

    plot(max(ROI_50{i})); hold on; yline(threshold(i)); hold on
    % For this, a different approach is needed - divide them into two parts
    ROI_post_peak{i} = ROI_50{i}(:, 610:end);  ROI_pre_peak{i} = ROI_50{i}(:, 1:609);
    Paint_ind = find(ROI_post_peak{i} > threshold(i));
    ROI_50_new_post{i, 1} = ROI_post_peak{i};  ROI_50_new_post{i, 1}(Paint_ind) = 0;
    ROI_50_new{i, 1} = [ROI_pre_peak{i}, ROI_50_new_post{i}];

    x_max_global(i) = max(max(ROI_50_new{i}));
    [max_values_50(i), column_indices_50(i)] = max(max(ROI_50_new{i}));
    plot(column_indices_50(i), max_values_50(i), 'ro', 'DisplayName', 'Data␣Point');
    label = sprintf('[%d,␣%d]', max_values_50(i), column_indices_50(i));
    text(column_indices_50(i) - 170, max_values_50(i) - 60, label, 'FontSize', 14, 'Interpreter', 'latex');
    hold on; plot(max(ROI_50_new{i}), 'r')
    title(['Image␣', num2str(i)], 'Interpreter', 'latex')
    xlabel('Pixel␣value␣of␣ROI', 'Interpreter', 'latex'); ylabel('Intensity␣value', 'Interpreter', 'latex')
    sgtitle('Peak␣Removal␣for␣ROI␣at␣50␣mm', 'Interpreter', 'latex')
end

%% Mean and std of the max peak value and its index
close all
mean_max = [mean(max_values_50), mean(max_values_101), mean(max_values_181)];
mean_ind = [mean(column_indices_50), mean(column_indices_101), mean(column_indices_181)];

std_max = [std(double(max_values_50)), std(double(max_values_101)), std(double(max_values_181))];
std_ind = [std(double(column_indices_50)), std(double(column_indices_101)), std(double(column_indices_181))];

%% IMMAGINE Showing the 3 depths and their maximum and the original image seen in the scintillator
figure;
Dimensione_x = size(ROI_50_new{1}, 2);
```

```
segnale_integrato{i} = max(double(ROI_50_new{i}));
[picchi, indici_picchi] = findpeaks(segnale_integrato{i});
[massimo_picco, indice_massimo] = max(picchi);
pixel_corrispondente{i} = Dimensione_x - indici_picchi(indice_massimo);

% Plot 50 mm
subplot(2, 3, 1);
plot(segnale_integrato{i}); hold on;
scatter(indici_picchi(indice_massimo), massimo_picco, 'ro', 'DisplayName', 'Massimo␣Picco');
ylabel('Luminosity', 'Interpreter', 'latex', 'FontSize', 14);
xlabel('Pixel', 'Interpreter', 'latex', 'FontSize', 14);
title('Signal␣-␣50␣mm', 'Interpreter', 'latex', 'FontSize', 14);
subplot(2, 3, 4); imshow(ROI_50_new{i}, []);
title('Original␣Image', 'Interpreter', 'latex', 'FontSize', 14);
shading flat; colormap gray; c = colorbar;
xlabel('pixel', 'Interpreter', 'latex', 'FontSize', 14);
ylabel('pixel', 'Interpreter', 'latex', 'FontSize', 14);
ylabel(c, 'Number␣of␣photons␣per␣pixel', 'Interpreter', 'latex', 'FontSize', 14)
segnale_integrato{i} = max(double(ROI_101_new{i}));
[picchi, indici_picchi] = findpeaks(segnale_integrato{i});
[massimo_picco, indice_massimo] = max(picchi);
pixel_corrispondente{i} = Dimensione_x - indici_picchi(indice_massimo);

% Plot 101 mm
subplot(2, 3, 2);
plot(segnale_integrato{i}); hold on;
scatter(indici_picchi(indice_massimo), massimo_picco, 'ro', 'DisplayName', 'Massimo␣Picco');
ylabel('Luminosity', 'Interpreter', 'latex', 'FontSize', 14);
xlabel('Pixel', 'Interpreter', 'latex', 'FontSize', 14);
title('Signal␣-␣101␣mm', 'Interpreter', 'latex', 'FontSize', 14);
subplot(2, 3, 5); imshow(ROI_101_new{i}, []);
title('Original␣Image', 'Interpreter', 'latex', 'FontSize', 14);
shading flat;colormap gray;c = colorbar;
xlabel('pixel', 'Interpreter', 'latex', 'FontSize', 14);
ylabel('pixel', 'Interpreter', 'latex', 'FontSize', 14);
ylabel(c, 'Number␣of␣photons␣per␣pixel', 'Interpreter', 'latex', 'FontSize', 14);
segnale_integrato{i} = max(double(ROI_181_new{i}));
[picchi, indici_picchi] = findpeaks(segnale_integrato{i});
[massimo_picco, indice_massimo] = max(picchi);
pixel_corrispondente{i} = Dimensione_x - indici_picchi(indice_massimo);

% Plot 181 mm
subplot(2, 3, 3);
plot(segnale_integrato{i}); hold on;
scatter(indici_picchi(indice_massimo), massimo_picco, 'ro', 'DisplayName', 'Massimo␣Picco');
ylabel('Luminosity', 'Interpreter', 'latex', 'FontSize', 14);
xlabel('Pixel', 'Interpreter', 'latex', 'FontSize', 14);
title('Signal␣-␣181␣mm', 'Interpreter', 'latex', 'FontSize', 14);
subplot(2, 3, 6); imshow(ROI_181_new{i}, []);
title('Original␣Image', 'Interpreter', 'latex', 'FontSize', 14);
shading flat;colormap gray;c = colorbar;
xlabel('pixel', 'Interpreter', 'latex', 'FontSize', 14);
ylabel('pixel', 'Interpreter', 'latex', 'FontSize', 14);
ylabel(c, 'Number␣of␣photons␣per␣pixel', 'Interpreter', 'latex', 'FontSize', 14);

sgtitle('Integrated␣signal␣with␣peak␣and␣original␣image␣of␣the␣spill', 'Interpreter',
```

```
'latex', 'FontSize', 16);

%% Range Calculation
% These value are calculated from the light image, taking into
% consideration the length in pixel of the scintillator walls (outside for
% K_prox and inside for K_dist) and diving them by 200 mm (length of scintillator)

K_prox= 1/3.7266; %mm/pixel -->  x = 100
K_dist= 1/3.0375; % --> x = -100
L_s= 200; % Length of the scintillator
n_air =1; n_scint = 1.58;

N_threshold_50=column_indices_50; N_threshold_101=column_indices_101;
N_threshold_181=column_indices_181;

N_edge=size(ROI_50_new{1}, 2);   %Pixel: end of scintillator on the right
H_r = 10.5; %mm Maximum length of the reflection

x_real_50 = 0; x_real_101 = 0; x_real_181 = 0; % real beam position inside the scintillator

R_50 = (((((K_prox - K_dist)/L_s)*((L_s/2)- x_real_50 )*(n_air/n_scint))+K_prox).*
(N_edge-N_threshold_50)-((H_r/L_s)*(x_real_50 - L_s/2))).*1.02
R_101 = (((((K_prox - K_dist)/L_s)*((L_s/2)- x_real_101 )*(n_air/n_scint))+K_prox).*
(N_edge-N_threshold_101)-((H_r/L_s)*(x_real_101 - L_s/2))).*1.02
R_181 = (((((K_prox - K_dist)/L_s)*((L_s/2)- x_real_181 )*(n_air/n_scint))+K_prox).*
(N_edge-N_threshold_181)-((H_r*2/L_s)*(x_real_181 - L_s/2))).*1.02

mean_R_50= [mean(R_50)]; std_R_50= [std(R_50)]
mean_R_101= [mean(R_101)]; std_R_101= [std(R_101)]
mean_R_181= [mean(R_181)]; std_R_181= [std(R_181)]

%% ROI OF THE VALUES BETWEEN THE 80% AND 100% OF THE PEAK  - Alternative approach. These ROI's
% were evaluated in a separate code with the methodology outlined in the thesis

ROI_y_181 = (120:165); ROI_x_181 = (335:370);
ROI_y_101 =(385:406); ROI_x_101 = (333:370);
ROI_y_50 = (553:566) ; ROI_x_50 = (334:372);

for i=1:5
    small_50{i,1}= ROI_50_new{i,1}(ROI_x_50,ROI_y_50);
    small_101{i,1}= ROI_101_new{i,1}(ROI_x_101,ROI_y_101);
    small_181{i,1}= ROI_181_new{i,1}(ROI_x_181,ROI_y_181);
end

for i=1:5
    mean_50(i)=mean(double(ROI_50_new{i}(:)));  std_50(i)=std(double(ROI_50_new{i}(:)));
    mean_101(i)=mean(double(ROI_101_new{i}(:)));  std_101(i)=std(double(ROI_101_new{i}(:)));
    mean_181(i)=mean(double(ROI_181_new{i}(:)));  std_181(i)=std(double(ROI_181_new{i}(:)));

    peak_50(i)=max(max(ROI_50_new{i}));
    peak_101(i)=max(max(ROI_101_new{i}));
    peak_181(i)=max(max(ROI_181_new{i}));

    small_mean_50(i)=mean(double(small_50{i}(:)));  small_std_50(i)=std(double(small_50{i}(:)));
    small_mean_101(i)=mean(double(small_101{i}(:)));  small_std_101(i)=std(double(small_101{i}(:)));
    small_mean_181(i)=mean(double(small_181{i}(:)));  small_std_181(i)=std(double(small_181{i}(:)));
```

```
end


mean_peak_50 = mean(peak_50);mean_peak_101 = mean(peak_101);mean_peak_181 = mean(peak_181)
std_peak_50 = std(double(peak_50));std_peak_101 = std(double(peak_101));std_peak_181 = std(double(peak_181))

mean_small_50 = mean(small_mean_50);mean_small_101 = mean(small_mean_101);mean_small_181 = mean(small_mean_181)
std_small_50 = std(small_std_50);std_small_101 = std(small_std_101);std_small_181 = std(small_std_181)

mean_vals = [mean_small_50, mean_small_101, mean_small_181]’;
std_vals = [std_small_50, std_small_101, std_small_181]’;

col_names = {’Mean_50’,’Std_50’,’Mean_101’,’Std_101’,’Mean_181’,’Std_181’};
row_names = {’ROI’};
data_table = table(mean_vals(1,:)’, std_vals(1,:)’, mean_vals(2,:)’, std_vals(2,:)’, mean_vals(3,:)’,
std_vals(3,:)’, ’VariableNames’, col_names, ’RowNames’, row_names);
disp(data_table);

%% PART 1 — NO FILTERING
%% SUBTRACTION BETWEEN NOT FILTERED IMAGES

SUB_50= {(ROI_50_new{1}) — ROI_50_new{2}; ROI_50_new{1} — ROI_50_new{3}; ROI_50_new{1} — ROI_50_new{4};
          ROI_50_new{1} — ROI_50_new{5}; ROI_50_new{2} — ROI_50_new{3};  ROI_50_new{2} — ROI_50_new{4};
          ROI_50_new{2} — ROI_50_new{5};ROI_50_new{3} — ROI_50_new{4}; ROI_50_new{3} — ROI_50_new{5};
          ROI_50_new{4} — ROI_50_new{5};}


SUB_101= {(ROI_101_new{1}) — ROI_101_new{2};ROI_101_new{1} — ROI_101_new{3}; ROI_101_new{1} — ROI_101_new{4};
          ROI_101_new{1} — ROI_101_new{5}; ROI_101_new{2} — ROI_101_new{3}; ROI_101_new{2} — ROI_101_new{4};
          ROI_101_new{2} — ROI_101_new{5}; ROI_101_new{3} — ROI_101_new{4}; ROI_101_new{3} — ROI_101_new{5};
          ROI_101_new{4} — ROI_101_new{5};}

SUB_181= {(ROI_181_new{1}) — ROI_181_new{2}; ROI_181_new{1} — ROI_181_new{3}; ROI_181_new{1} — ROI_181_new{4};
          ROI_181_new{1} — ROI_181_new{5}; ROI_181_new{2} — ROI_181_new{3}; ROI_181_new{2} — ROI_181_new{4};
          ROI_181_new{2} — ROI_181_new{5}; ROI_181_new{3} — ROI_181_new{4}; ROI_181_new{3} — ROI_181_new{5};
          ROI_181_new{4} — ROI_181_new{5};}

for i=1:10
    max_sub_50(i)=max(double(SUB_50{i}(:))); min_sub_50(i)=min(double(SUB_50{i}(:)));
    max_sub_101(i)=max(double(SUB_101{i}(:))); min_sub_101(i)=min(double(SUB_101{i}(:)));
    max_sub_181(i)=max(double(SUB_181{i}(:))); min_sub_181(i)=min(double(SUB_181{i}(:)));
end

max_mean_50 = mean (max_sub_50); max_std_50 = std (max_sub_50);
min_mean_50 = mean(min_sub_50); min_std_50 = std (min_sub_50);
max_mean_101 = mean (max_sub_101); max_std_101 = std (max_sub_101);
min_mean_101 = mean(min_sub_101); min_std_101 = std (min_sub_101);
max_mean_181 = mean (max_sub_181); max_std_181 = std (max_sub_181);
min_mean_181 = mean(min_sub_181); min_std_181 = std (min_sub_181);

data = [max_mean_50, max_std_50, min_mean_50, min_std_50;
        max_mean_101, max_std_101, min_mean_101, min_std_101;
        max_mean_181, max_std_181, min_mean_181, min_std_181];

%table
variable_names = {’Max_Mean’, ’Std_Max’, ’Min_Mean’, ’Std_Min’};
```

```
row_names = {’Depth␣50’, ’Depth␣101’, ’Depth␣181’};
T = array2table(data, ’VariableNames’, variable_names, ’RowNames’, row_names);
disp(T);

%% IMAGE — NO FILTERING
max_value = max([max(ROI_50_new{1}(:)), max(ROI_50_new{2}(:)), max(SUB_50{1}(:))]);
min_value = min([min(ROI_50_new{1}(:)), min(ROI_50_new{2}(:)), min(SUB_50{1}(:))]);

figure
%First subplot
subplot(1,3,1)
meshc(ROI_50_new{1}); colormap(jet); colorbar;
title(’First␣Picture’, ’Interpreter’, ’latex’, ’FontSize’, 16)
xlabel(’Pixel␣value␣of␣ROI’, ’Interpreter’, ’latex’, ’FontSize’, 14)
ylabel(’Pixel␣value␣of␣ROI’, ’Interpreter’, ’latex’, ’FontSize’, 14)
zlabel(’Difference’, ’Interpreter’, ’latex’, ’FontSize’, 14)
axis tight; caxis([min_value, max_value]);

% Second subplot
subplot(1,3,2)
meshc(ROI_50_new{2}); colormap(jet); colorbar;
title(’Second␣Picture’, ’Interpreter’, ’latex’, ’FontSize’, 16)
xlabel(’Pixel␣value␣of␣ROI’, ’Interpreter’, ’latex’, ’FontSize’, 14)
ylabel(’Pixel␣value␣of␣ROI’, ’Interpreter’, ’latex’, ’FontSize’, 14)
zlabel(’Difference’, ’Interpreter’, ’latex’, ’FontSize’, 14)
axis tight; caxis([min_value, max_value]);

% Third subplot
subplot(1,3,3)
meshc(SUB_50{1}); colormap(jet); colorbar;
title(’Difference␣between␣two␣"identical"␣paints’, ’Interpreter’, ’latex’, ’FontSize’, 16)
xlabel(’Pixel␣value␣of␣ROI’, ’Interpreter’, ’latex’, ’FontSize’, 14)
ylabel(’Pixel␣value␣of␣ROI’, ’Interpreter’, ’latex’, ’FontSize’, 14)
zlabel(’Difference’, ’Interpreter’, ’latex’, ’FontSize’, 14)
axis tight;
sgtitle(’Images␣and␣subtraction␣without␣filtering’, ’Interpreter’, ’latex’, ’FontSize’, 16)


%% PART 2 FILTERING
% Two filtering methods are applied, re—binning and median filter
% 1. Re—binning
% 2. Median Filtering

%% 1. Rebinning

L_kernel = 3; % Only change This value to change the kernel size

n_righe = size(ROI_50_new{1},1); n_colonne = size(ROI_50_new{1},2);
size_1= round(size(ROI_50_new{1},1)/L_kernel); size_2 = round(size(ROI_50_new{1},2)/L_kernel);

immagine_ricomposta_50={}; immagine_ricomposta_101={}; immagine_ricomposta_181={};
for s =1:5
    for i = 1:L_kernel:(size(ROI_50_new{1},1)—L_kernel)
        for j = 1:L_kernel:(size(ROI_50_new{1},2)—L_kernel)

            finestra_50 = ROI_50_new{s}(i:i+(L_kernel—1), j:j+(L_kernel—1));
```

```
            finestra_101 = ROI_101_new{s}(i:i+(L_kernel−1), j:j+(L_kernel−1));
            finestra_181 = ROI_181_new{s}(i:i+(L_kernel−1), j:j+(L_kernel−1));

            media_50 = mean(finestra_50(:)); media_101 = mean(finestra_101(:));
            media_181 = mean(finestra_181(:));

            immagine_ricomposta_50{s}((i−1)/L_kernel + 1, (j−1)/L_kernel + 1) = media_50;
            immagine_ricomposta_101{s}((i−1)/L_kernel + 1, (j−1)/L_kernel + 1) = media_101;
            immagine_ricomposta_181{s}((i−1)/L_kernel + 1, (j−1)/L_kernel + 1) = media_181;

        end
    end
end

% SUBTRACTION OF THE SAME IMAGE
for i=1:5
    max_peak_50(i) = max(immagine_ricomposta_50{i}(:));
    max_peak_101(i) = max(immagine_ricomposta_101{i}(:));
    max_peak_181(i) = max(immagine_ricomposta_181{i}(:));
end

mean_peak_50 = mean(max_peak_50); mean_peak_101 = mean(max_peak_101);
mean_peak_181 = mean(max_peak_181);
std_peak_50 = std(double(max_peak_50)); std_peak_101 = std(double(max_peak_101));
std_peak_181 = std(double(max_peak_181));

SUB_50= {(immagine_ricomposta_50{1}) − immagine_ricomposta_50{2};
          immagine_ricomposta_50{1} − immagine_ricomposta_50{3};
          immagine_ricomposta_50{1} − immagine_ricomposta_50{4};
          immagine_ricomposta_50{1} − immagine_ricomposta_50{5};
          immagine_ricomposta_50{2} − immagine_ricomposta_50{3};
          immagine_ricomposta_50{2} − immagine_ricomposta_50{4};
          immagine_ricomposta_50{2} − immagine_ricomposta_50{5};
          immagine_ricomposta_50{3} − immagine_ricomposta_50{4};
          immagine_ricomposta_50{3} − immagine_ricomposta_50{5};
          immagine_ricomposta_50{4} − immagine_ricomposta_50{5};}

SUB_101= {(immagine_ricomposta_101{1}) − immagine_ricomposta_101{2};
          immagine_ricomposta_101{1} − immagine_ricomposta_101{3};
          immagine_ricomposta_101{1} − immagine_ricomposta_101{4};
          immagine_ricomposta_101{1} − immagine_ricomposta_101{5};
          immagine_ricomposta_101{2} − immagine_ricomposta_101{3};
          immagine_ricomposta_101{2} − immagine_ricomposta_101{4};
          immagine_ricomposta_101{2} − immagine_ricomposta_101{5};
          immagine_ricomposta_101{3} − immagine_ricomposta_101{4};
          immagine_ricomposta_101{3} − immagine_ricomposta_101{5};
          immagine_ricomposta_101{4} − immagine_ricomposta_101{5};}

SUB_181= {(immagine_ricomposta_181{1}) − immagine_ricomposta_181{2};
          immagine_ricomposta_181{1} − immagine_ricomposta_181{3};
          immagine_ricomposta_181{1} − immagine_ricomposta_181{4};
          immagine_ricomposta_181{1} − immagine_ricomposta_181{5};
          immagine_ricomposta_181{2} − immagine_ricomposta_181{3};
          immagine_ricomposta_181{2} − immagine_ricomposta_181{4};
          immagine_ricomposta_181{2} − immagine_ricomposta_181{5};
          immagine_ricomposta_181{3} − immagine_ricomposta_181{4};
```

```
          immagine_ricomposta_181{3} — immagine_ricomposta_181{5};
          immagine_ricomposta_181{4} — immagine_ricomposta_181{5};}

for i=1:10
    max_sub_50(i)=max((SUB_50{i}(:))); min_sub_50(i)=min((SUB_50{i}(:)));
    max_sub_101(i)=max((SUB_101{i}(:)));  min_sub_101(i)=min((SUB_101{i}(:)));
    max_sub_181(i)=max((SUB_181{i}(:))); min_sub_181(i)=min((SUB_181{i}(:)));
end

mean_max_sub_50=mean(max_sub_50);std_max_sub_50=std(max_sub_50);
mean_min_sub_50=mean(min_sub_50);std_min_sub_50=std(min_sub_50);
mean_max_sub_101=mean(max_sub_101);std_max_sub_101=std(max_sub_101);
mean_min_sub_101=mean(min_sub_101);std_min_sub_101=std(min_sub_101);
mean_max_sub_181=mean(max_sub_181);std_max_sub_181=std(max_sub_181);
mean_min_sub_181=mean(min_sub_181);std_min_sub_181=std(min_sub_181);

% Table  for 3x3
max_vals = [mean_max_sub_50, mean_max_sub_101, mean_max_sub_181]’;
min_vals = [mean_min_sub_50, mean_min_sub_101, mean_min_sub_181]’;

col_names = {’Max_50’,’Min_50’,’Max_101’,’Min_101’,’Max_181’,’Min_181’};
row_names = {’KERNEL␣3X3␣—␣Re—binning’, };
data_table_3 = table(max_vals(1,:)’, min_vals(1,:)’, max_vals(2,:)’, min_vals(2,:)’,
max_vals(3,:)’, min_vals(3,:)’, ’VariableNames’, col_names, ’RowNames’, row_names);
disp(data_table_3);

%% IMMAGE for re—binnning
max_value = max([max(immagine_ricomposta_50{1}(:)), max(immagine_ricomposta_50{2}(:)), max(SUB_50{1}(:))]);
min_value = min([min(immagine_ricomposta_50{1}(:)), min(immagine_ricomposta_50{2}(:)), min(SUB_50{1}(:))]);

figure
subplot(1,3,1)
meshc(immagine_ricomposta_50{1}); colormap(jet); colorbar;
title(’First␣Picture’, ’Interpreter’, ’latex’, ’FontSize’, 16)
xlabel(’Pixel␣value␣of␣ROI’, ’Interpreter’, ’latex’, ’FontSize’, 14)
ylabel(’Pixel␣value␣of␣ROI’, ’Interpreter’, ’latex’, ’FontSize’, 14)
zlabel(’Difference’, ’Interpreter’, ’latex’, ’FontSize’, 14)
axis tight; caxis([min_value, max_value]);

subplot(1,3,2)
meshc(immagine_ricomposta_50{2}); colormap(jet); colorbar;
title(’Second␣Picture␣’, ’Interpreter’, ’latex’, ’FontSize’, 16)
xlabel(’Pixel␣value␣of␣ROI’, ’Interpreter’, ’latex’, ’FontSize’, 14)
ylabel(’Pixel␣value␣of␣ROI’, ’Interpreter’, ’latex’, ’FontSize’, 14)
zlabel(’Difference’, ’Interpreter’, ’latex’, ’FontSize’, 14)
axis tight; caxis([min_value, max_value]);

subplot(1,3,3)
meshc(SUB_50{1}); colormap(jet); colorbar;
title(’Difference␣between␣two␣"identical"␣paints’, ’Interpreter’, ’latex’, ’FontSize’, 16)
xlabel(’Pixel␣value␣of␣ROI’, ’Interpreter’, ’latex’, ’FontSize’, 14)
ylabel(’Pixel␣value␣of␣ROI’, ’Interpreter’, ’latex’, ’FontSize’, 14)
zlabel(’Difference’, ’Interpreter’, ’latex’, ’FontSize’, 14)
axis tight; caxis([min_value, max_value]);
sgtitle(’Subtraction␣of␣similar␣images␣with␣Re—Binning’,’Interpreter’, ’latex’, ’FontSize’, 16 )
```

```
%% 2. Median Filter
med50_3 = {}; med50_5={}; med50_7={}; med101_3 = {}; med101_5={}; med101_7={}; med181_3 = {};
med181_5={}; med181_7={};

for i=1:numImages
    % 50 mm
    med50_3{i} = (medfilt2(ROI_50_new{i}, [3,3])); med50_5{i} = (medfilt2(ROI_50_new{i}, [5,5]));
    % 101 mm
    med101_3{i} = (medfilt2(ROI_101_new{i}, [3,3])); med101_5{i} = (medfilt2(ROI_101_new{i}, [5,5]));
    % 181 mm
    med181_3{i} = (medfilt2(ROI_181_new{i}, [3,3])); med181_5{i} = (medfilt2(ROI_181_new{i}, [5,5]));
end


% KERNEL 3
for i=1:5
    max_peak_50(i) = max(med50_3{i}(:)); max_peak_101(i) = max(med101_3{i}(:));
    max_peak_181(i) = max(med181_3{i}(:));
end
mean_peak_50 = mean(max_peak_50); mean_peak_101 = mean(max_peak_101);
mean_peak_181 = mean(max_peak_181);
std_peak_50 = std(double(max_peak_50)); std_peak_101 = std(double(max_peak_101));
std_peak_181 = std(double(max_peak_181))

% KERNEL 5
for i=1:5
    max_peak_50(i) = max(med50_5{i}(:)); max_peak_101(i) = max(med101_5{i}(:));
    max_peak_181(i) = max(med181_5{i}(:));
end
mean_peak_50 = mean(max_peak_50); mean_peak_101 = mean(max_peak_101);
mean_peak_181 = mean(max_peak_181);
std_peak_50 = std(double(max_peak_50)); std_peak_101 = std(double(max_peak_101));
std_peak_181 = std(double(max_peak_181))

% KERNEL 3
SUB_50_3= {(med50_3{1}) — med50_3{2}; med50_3{1} — med50_3{3}; med50_3{1} — med50_3{4};
          med50_3{1} — med50_3{5}; med50_3{2} — med50_3{3}; med50_3{2} — med50_3{4};
          med50_3{2} — med50_3{5}; med50_3{3} — med50_3{4}; med50_3{3} — med50_3{5};
          med50_3{4} — med50_3{5};}

SUB_101_3= {(med101_3{1}) — med101_3{2};med101_3{1} — med101_3{3};med101_3{1} — med101_3{4};
          med101_3{1} — med101_3{5};med101_3{2} — med101_3{3};med101_3{2} — med101_3{4};
          med101_3{2} — med101_3{5}; med101_3{3} — med101_3{4}; med101_3{3} — med101_3{5};
          med101_3{4} — med101_3{5};}

SUB_181_3= {(med181_3{1}) — med181_3{2};med181_3{1} — med181_3{3}; med181_3{1} — med181_3{4};
          med181_3{1} — med181_3{5};med181_3{2} — med181_3{3};med181_3{2} — med181_3{4};
          med181_3{2} — med181_3{5}; med181_3{3} — med181_3{4}; med181_3{3} — med181_3{5};
          med181_3{4} — med181_3{5};}

for i=1:10
    max_sub_50_3(i)=max((SUB_50_3{i}(:)));  min_sub_50_3(i)=min((SUB_50_3{i}(:)));
    max_sub_101_3(i)=max((SUB_101_3{i}(:))); min_sub_101_3(i)=min((SUB_101_3{i}(:)));
    max_sub_181_3(i)=max((SUB_181_3{i}(:))); min_sub_181_3(i)=min((SUB_181_3{i}(:)));
end
```

```
% KERNEL 5
SUB_50_5= {(med50_5{1}) - med50_5{2}; med50_5{1} - med50_5{3}; med50_5{1} - med50_5{4};
          med50_5{1} - med50_5{5}; med50_5{2} - med50_5{3}; med50_5{2} - med50_5{4};
          med50_5{2} - med50_5{5}; med50_5{3} - med50_5{4}; med50_5{3} - med50_5{5};
          med50_5{4} - med50_5{5};}

SUB_101_5= {(med101_5{1}) - med101_5{2}; med101_5{1} - med101_5{3}; med101_5{1} - med101_5{4};
          med101_5{1} - med101_5{5}; med101_5{2} - med101_5{3};med101_5{2} - med101_5{4};
          med101_5{2} - med101_5{5}; med101_5{3} - med101_5{4};med101_5{3} - med101_5{5};
          med101_5{4} - med101_5{5};}

SUB_181_5= {(med181_5{1}) - med181_5{2}; med181_5{1} - med181_5{3};med181_5{1} - med181_5{4};
          med181_5{1} - med181_5{5}; med181_5{2} - med181_5{3};med181_5{2} - med181_5{4};
          med181_5{2} - med181_5{5};med181_5{3} - med181_5{4}; med181_5{3} - med181_5{5};
          med181_5{4} - med181_5{5};}

for i=1:10
    max_sub_50_5(i)=max((SUB_50_5{i}(:))); min_sub_50_5(i)=min((SUB_50_5{i}(:)));
    max_sub_101_5(i)=max((SUB_101_5{i}(:))); min_sub_101_5(i)=min((SUB_101_5{i}(:)));
    max_sub_181_5(i)=max((SUB_181_5{i}(:))); min_sub_181_5(i)=min((SUB_181_5{i}(:)));
end

% 50
mean_max_50_3=mean(max_sub_50_3); mean_min_50_3=mean(min_sub_50_3);
mean_max_50_5=mean(max_sub_50_5); mean_min_50_5=mean(min_sub_50_5);
%101
mean_max_101_3=mean(max_sub_101_3); mean_min_101_3=mean(min_sub_101_3);
mean_max_101_5=mean(max_sub_101_5); mean_min_101_5=mean(min_sub_101_5);
%181
mean_max_181_3=mean(max_sub_181_3); mean_min_181_3=mean(min_sub_181_3);
mean_max_181_5=mean(max_sub_181_5); mean_min_181_5=mean(min_sub_181_5);

% Table
max_vals = [mean_max_50_3, mean_max_101_3, mean_max_181_3]';
min_vals = [mean_min_50_3, mean_min_101_3, mean_min_181_3]';
max_vals_5 = [mean_max_50_5, mean_max_101_5, mean_max_181_5]';
min_vals_5 = [mean_min_50_5, mean_min_101_5, mean_min_181_5]';

col_names = {'Max_50','Min_50','Max_101','Min_101','Max_181','Min_181'};
row_names = {'KERNEL␣3X3', };
data_table_3 = table(max_vals(1,:)', min_vals(1,:)', max_vals(2,:)', min_vals(2,:)',
max_vals(3,:)', min_vals(3,:)', 'VariableNames', col_names, 'RowNames', row_names);
disp(data_table_3);

col_names = {'Max_50','Min_50','Max_101','Min_101','Max_181','Min_181'};
row_names = {'KERNEL␣5X5'};
data_table_5 = table(max_vals_5(1,:)', min_vals_5(1,:)', max_vals_5(2,:)', min_vals_5(2,:)',
max_vals_5(3,:)', min_vals_5(3,:)', 'VariableNames', col_names, 'RowNames', row_names);
disp(data_table_5);

% Image - Median filter
max_value = max([max(med50_3{1}(:)), max(med50_3{2}(:)), max(SUB_50_3{1}(:))]);
min_value = min([min(med50_3{1}(:)), min(med50_3{2}(:)), min(SUB_50_3{1}(:))]);

figure
subplot(1,3,1)
```

```
meshc(med50_3{1}); colormap(jet); colorbar;
title(’First␣Picture’, ’Interpreter’, ’latex’, ’FontSize’, 16)
xlabel(’Pixel␣value␣of␣ROI’, ’Interpreter’, ’latex’, ’FontSize’, 14)
ylabel(’Pixel␣value␣of␣ROI’, ’Interpreter’, ’latex’, ’FontSize’, 14)
zlabel(’Difference’, ’Interpreter’, ’latex’, ’FontSize’, 14)
axis tight; caxis([min_value, max_value]);

subplot(1,3,2)
meshc(med50_3{2}); colormap(jet); colorbar;
title(’Second␣Picture’, ’Interpreter’, ’latex’, ’FontSize’, 16)
xlabel(’Pixel␣value␣of␣ROI’, ’Interpreter’, ’latex’, ’FontSize’, 14)
ylabel(’Pixel␣value␣of␣ROI’, ’Interpreter’, ’latex’, ’FontSize’, 14)
zlabel(’Difference’, ’Interpreter’, ’latex’, ’FontSize’, 14)
axis tight; caxis([min_value, max_value]);

subplot(1,3,3)
meshc(SUB_50_3{1}); colormap(jet); colorbar;
title(’Difference␣between␣two␣"identical"␣paints’, ’Interpreter’, ’latex’, ’FontSize’, 16)
xlabel(’Pixel␣value␣of␣ROI’, ’Interpreter’, ’latex’, ’FontSize’, 14)
ylabel(’Pixel␣value␣of␣ROI’, ’Interpreter’, ’latex’, ’FontSize’, 14)
zlabel(’Difference’, ’Interpreter’, ’latex’, ’FontSize’, 14)
axis tight; caxis([min_value, max_value]);
sgtitle(’Subtraction␣of␣similar␣images␣with␣Median␣Filter’,’Interpreter’, ’latex’, ’FontSize’, 16)
```

Post-processing of the images and subtraction between different images

```
% Load the correct folder paths
folderPath_50 = ’C:\...\Misure␣10_09_23\paint\Paint_50’;
folderPath_52 = ’C:\..\Misure␣10_09_23\paint\Paint_52’;
folderPath_54 = ’C:\...\Misure␣10_09_23\paint\Paint_54’;
folderPath_101 = ’C:\...\Misure␣10_09_23\paint\Paint_101’;
folderPath_103 = ’C:\...\Misure␣10_09_23\paint\Paint_103’;

fileList_50 = dir(fullfile(folderPath_50, ’∗.tif’));
fileList_52 = dir(fullfile(folderPath_52, ’∗.tif’));
fileList_54 = dir(fullfile(folderPath_54, ’∗.tif’));

fileList_101 = dir(fullfile(folderPath_101, ’∗.tif’));
fileList_103 = dir(fullfile(folderPath_103, ’∗.tif’));

numImages = numel(fileList_50);
Paint_50 = cell(numImages, 1); Paint_52 = cell(numImages, 1); Paint_54 = cell(numImages, 1);
Paint_101 = cell(numImages, 1); Paint_103 = cell(numImages, 1);

for i = 1:numImages
    filename_50 = fullfile(folderPath_50, fileList_50(i).name);
    image_50 = imread(filename_50); Paint_50{i} = image_50;
    filename_52 = fullfile(folderPath_52, fileList_52(i).name);
    image_52 = imread(filename_52); Paint_52{i} = image_52;
    filename_54 = fullfile(folderPath_54, fileList_54(i).name);
    image_54 = imread(filename_54);Paint_54{i} = image_54;
    filename_101 = fullfile(folderPath_101, fileList_101(i).name);
    image_101 = imread(filename_101); Paint_101{i} = image_101;
    filename_103 = fullfile(folderPath_103, fileList_103(i).name);
    image_103 = imread(filename_103); Paint_103{i} = image_103;
end

myFolderBkg = ’C:\...\Misure␣10_09_23\background_1s.tif’;
fullFileName = fullfile(myFolderBkg); Bkg{1} = imread(fullFileName);

for i=1:numImages
    Paint_50{i} = Paint_50{i}−Bkg{1}; Paint_52{i} = Paint_52{i}−Bkg{1};
    Paint_54{i} = Paint_54{i}−Bkg{1};
    Paint_101{i} = Paint_101{i}−Bkg{1}; Paint_103{i} = Paint_103{i}−Bkg{1};
end

Paint_50 = cellfun(@int16, Paint_50 , ’UniformOutput’, false);
Paint_52 = cellfun(@int16, Paint_52 , ’UniformOutput’, false);
Paint_54 = cellfun(@int16, Paint_54 , ’UniformOutput’, false);
Paint_101 = cellfun(@int16, Paint_101 , ’UniformOutput’, false);
Paint_103 = cellfun(@int16, Paint_103 , ’UniformOutput’, false);


%% ROI
ROI_y = (231:980); ROI_x = (177:926);
ROI_Paint_50={}; ROI_Paint_52={}; ROI_Paint_54={};
ROI_Paint_101={}; ROI_Paint_103={};

for i=1:numImages
    ROI_Paint_50{i,1}= Paint_50{i,1}(ROI_x,ROI_y); ROI_Paint_52{i,1}= Paint_52{i,1}(ROI_x,ROI_y);
```

```
    ROI_Paint_54{i,1}= Paint_54{i,1}(ROI_x,ROI_y);
    ROI_Paint_101{i,1}= Paint_101{i,1}(ROI_x,ROI_y); ROI_Paint_103{i,1}= Paint_103{i,1}(ROI_x,ROI_y);
end

%%
Paint_ind=[]; Paint_new_50={}; Paint_new_52={}; Paint_new_54={};
soglia=[]; mean_Paint=[];
valore_prima_picco = 500;   % MANUALLY IMPOSE
valore_soglia = 0.5;        % MANUALLY IMPOSE

figure  % 50
for i = 1:numImages
    subplot(1,numImages,i)
    mean_Paint(i)=mean(max(ROI_Paint_50{i})); soglia(i) = mean_Paint(i)*valore_soglia;
    plot(max(ROI_Paint_50{i})); hold on
    yline(soglia(i)); hold on
    Paint_ind = find(ROI_Paint_50{i}(:, 1:valore_prima_picco) > soglia(i));
    Paint_new_50{i,1} = ROI_Paint_50{i};
    Paint_new_50{i,1}(Paint_ind) = 0;
    x_max_globale(i)=max(max(Paint_new_50{i}));
    [max_values_50(i), indici_colonne_50(i)] = max(max(Paint_new_50{i}));
    plot(indici_colonne_50(i),max_values_50(i), 'ro', 'DisplayName', 'Data_Point');
    label = sprintf('[%d,␣%d]', max_values_50(i), indici_colonne_50(i));
    text(indici_colonne_50(i) - 170, max_values_50(i) - 60, label, 'FontSize', 14,  Interpreter='latex');
    hold on; plot(max(Paint_new_50{i}))
    title('Immagine␣', num2str(i), Interpreter='latex')
    xlabel('Pixel␣value␣of␣ROI', 'Interpreter', 'latex')
    ylabel('Intensity␣value', 'Interpreter', 'latex')
    sgtitle('Rimozione␣picchi␣per␣ROI␣a␣50␣mm',  Interpreter='latex')
end

figure % 52
for i = 1:numImages
    subplot(1,numImages,i)
    mean_Paint(i)=mean(max(ROI_Paint_52{i}));
    soglia(i) = mean_Paint(i)*valore_soglia;
    plot(max(ROI_Paint_52{i})); hold on
    yline(soglia(i)); hold on
    Paint_ind = find(ROI_Paint_52{i}(:, 1:valore_prima_picco) > soglia(i));
    Paint_new_52{i,1} = ROI_Paint_52{i};
    Paint_new_52{i,1}(Paint_ind) = 0;
    x_max_globale(i)=max(max(Paint_new_52{i}));
    [max_values_52(i), indici_colonne_52(i)] = max(max(Paint_new_52{i}));
    plot(indici_colonne_52(i),max_values_52(i), 'ro', 'DisplayName', 'Data_Point');
    label = sprintf('[%d,␣%d]', max_values_52(i), indici_colonne_52(i));
    text(indici_colonne_52(i) - 170, max_values_52(i) - 60, label, 'FontSize', 14,  Interpreter='latex');
    hold on; plot(max(Paint_new_52{i}))
    title('Immagine␣', num2str(i), Interpreter='latex')
    xlabel('Pixel␣value␣of␣ROI', 'Interpreter', 'latex')
    ylabel('Intensity␣value', 'Interpreter', 'latex')
    sgtitle('Rimozione␣picchi␣per␣ROI␣a␣52mm', 'Interpreter', 'latex')
end

figure % 54
for i = 1:numImages
    subplot(1,numImages,i)
```

```
    mean_Paint(i)=mean(max(ROI_Paint_54{i}));
    soglia(i) = mean_Paint(i)∗valore_soglia;
    plot(max(ROI_Paint_54{i})); hold on
    yline(soglia(i));  hold on
    Paint_ind = find(ROI_Paint_54{i}(:, 1:valore_prima_picco) > soglia(i));
    Paint_new_54{i,1} = ROI_Paint_54{i};
    Paint_new_54{i,1}(Paint_ind) = 0;
    x_max_globale(i)=max(max(Paint_new_54{i}));
    [max_values_54(i), indici_colonne_54(i)] = max(max(Paint_new_54{i}));
    hold on; plot(indici_colonne_54(i),max_values_54(i), 'ro', 'DisplayName', 'Data␣Point');
    label = sprintf('[%d,␣%d]', max_values_54(i), indici_colonne_54(i));
    text(indici_colonne_54(i) — 170, max_values_54(i) — 60, label, 'FontSize', 14,  Interpreter='latex');
    plot(max(Paint_new_54{i}))
    title('Immagine␣', num2str(i), Interpreter='latex')
    xlabel('Pixel␣value␣of␣ROI', 'Interpreter', 'latex')
    ylabel('Intensity␣value', 'Interpreter', 'latex')
    sgtitle('Rimozione␣picchi␣per␣ROI␣a␣54mm', 'Interpreter', 'latex')
end

%%
close all
Paint_ind=[]; Paint_new_101={}; Paint_new_103={};
soglia=[]; mean_Paint=[];
valore_prima_picco = 362;   % MANUALLY IMPOSED
valore_soglia = 0.4;        % MANUALLY IMPOSED

figure % 101
for i = 1:numImages
    subplot(1,numImages,i)
    mean_Paint(i)=mean(max(ROI_Paint_101{i}));
    soglia(i) = mean_Paint(i)∗valore_soglia;
    plot(max(ROI_Paint_101{i})); hold on
    yline(soglia(i));  hold on
    Paint_ind = find(ROI_Paint_101{i}(:, 1:valore_prima_picco) > soglia(i));
    Paint_new_101{i,1} = ROI_Paint_101{i};
    Paint_new_101{i,1}(Paint_ind) = 0;
    x_max_globale(i)=max(max(Paint_new_101{i}));
    [max_values_101(i), indici_colonne_101(i)] = max(max(Paint_new_101{i}));
    hold on
    plot(indici_colonne_101(i),max_values_101(i), 'ro', 'DisplayName', 'Data␣Point');
    label = sprintf('[%d,␣%d]', max_values_101(i), indici_colonne_101(i));
    text(indici_colonne_101(i) — 170, max_values_101(i) — 60, label, 'FontSize', 14,  Interpreter='latex');
    plot(max(Paint_new_101{i}))
    title('Immagine␣', num2str(i), Interpreter='latex')
    xlabel('Pixel␣value␣of␣ROI', 'Interpreter', 'latex')
    ylabel('Intensity␣value', 'Interpreter', 'latex')
    sgtitle('Rimozione␣picchi␣per␣ROI␣a␣101mm', 'Interpreter', 'latex')
end


figure % 103
for i = 1:numImages
    subplot(1,numImages,i)
    mean_Paint(i)=mean(max(ROI_Paint_103{i}));
    soglia(i) = mean_Paint(i)∗valore_soglia;
    plot(max(ROI_Paint_103{i})); hold on
```

```
    yline(soglia(i)); hold on
    Paint_ind = find(ROI_Paint_103{i}(:, 1:valore_prima_picco) > soglia(i));
    Paint_new_103{i,1} = ROI_Paint_103{i};
    Paint_new_103{i,1}(Paint_ind) = 0;
    x_max_globale(i)=max(max(Paint_new_103{i}));
    [max_values_103(i), indici_colonne_103(i)] = max(max(Paint_new_103{i}));
    hold on
    plot(indici_colonne_103(i),max_values_103(i), 'ro', 'DisplayName', 'Data␣Point');
    label = sprintf('[%d,␣%d]', max_values_103(i), indici_colonne_103(i));
    text(indici_colonne_103(i) − 170, max_values_103(i) − 60, label, 'FontSize', 14,  Interpreter='latex');
    plot(max(Paint_new_103{i}))
    title('Immagine␣', num2str(i), Interpreter='latex')
    xlabel('Pixel␣value␣of␣ROI', 'Interpreter', 'latex')
    ylabel('Intensity␣value', 'Interpreter', 'latex')
    sgtitle('Rimozione␣picchi␣per␣ROI␣a␣103mm', 'Interpreter', 'latex')
end


%% Filtering is applied: 1. Median Filter  2. Re−binning
%% 1. Median filter
med50_3 = {}; med50_5={}; med52_3 = {}; med52_5={};  med54_3 = {}; med54_5={};
med101_3 = {}; med101_5={}; med103_3 = {}; med103_5={};

for i=1:numImages
    med50_3{i} = (medfilt2(Paint_new_50{i}, [3,3])); med50_5{i} = (medfilt2(Paint_new_50{i}, [5,5]));
    med52_3{i} = (medfilt2(Paint_new_52{i}, [3,3])); med52_5{i} = (medfilt2(Paint_new_52{i}, [5,5]));
    med54_3{i} = (medfilt2(Paint_new_54{i}, [3,3])); med54_5{i} = (medfilt2(Paint_new_54{i}, [5,5]));
    med101_3{i} = (medfilt2(Paint_new_101{i}, [3,3])); med101_5{i} = (medfilt2(Paint_new_101{i}, [5,5]));
    med103_3{i} = (medfilt2(Paint_new_103{i}, [3,3])); med103_5{i} = (medfilt2(Paint_new_103{i}, [5,5]));
end

%% SUBTRACTION with median filter −−> KERNEL 3
for i=1:3
    max_peak_50(i) = max(med50_3{i}(:)); max_peak_52(i) = max(med52_3{i}(:));
    max_peak_54(i) = max(med54_3{i}(:));
    max_peak_101(i) = max(med101_3{i}(:)); max_peak_103(i) = max(med103_3{i}(:));
end
mean_peak_50 = mean(max_peak_50); mean_peak_52 = mean(max_peak_52); mean_peak_54 = mean(max_peak_54);
mean_peak_101 = mean(max_peak_101); mean_peak_103 = mean(max_peak_103);

std_peak_50 = std(double(max_peak_50)); std_peak_52 = std(double(max_peak_52));
std_peak_54 = std(double(max_peak_54));
std_peak_101 = std(double(max_peak_101)); std_peak_103 = std(double(max_peak_103));

% Image average between the three images, the resulting images will be subtracted
med50_3_tot= (med50_3{1,1} + med50_3{1,2} + med50_3{1,3})/3;
med52_3_tot= (med52_3{1,1} + med52_3{1,2} + med52_3{1,3})/3;
med54_3_tot= (med54_3{1,1} + med54_3{1,2} + med54_3{1,3})/3;
med101_3_tot= (med101_3{1,1} + med101_3{1,2} + med101_3{1,3})/3;
med103_3_tot= (med103_3{1,1} + med103_3{1,2} + med103_3{1,3})/3;

% Calculate the maximum and the peak index for the average image
massimo_50 = max(med50_3_tot(:));[indice_riga_50, indice_colonna_50] = find(med50_3_tot == massimo_50);
massimo_52 = max(med52_3_tot(:));[indice_riga_52, indice_colonna_52] = find(med52_3_tot == massimo_52);
massimo_54 = max(med54_3_tot(:));[indice_riga_54, indice_colonna_54] = find(med54_3_tot == massimo_54);
massimo_101 = max(med101_3_tot(:));[indice_riga_101, indice_colonna_101] = find(med101_3_tot == massimo_101);
```

```
massimo_103 = max(med103_3_tot(:));[indice_riga_103, indice_colonna_103] = find(med103_3_tot == massimo_103);

% TABELLA
depths = [50, 52, 54, 101, 103];
peak_values = [massimo_50, massimo_52, massimo_54, massimo_101, massimo_103];
peak_indices = [indice_colonna_50, indice_colonna_52, indice_colonna_54, indice_colonna_101, indice_colonna_103];
T = table(depths', peak_values', peak_indices',  ...
    'VariableNames', {'Depth', 'Peak␣Value', 'Peak␣Index'});
disp(T);

%% Subtraction
SUB_5250 = med52_3_tot-med50_3_tot; SUB_5452 = med54_3_tot-med52_3_tot;
SUB_5450 = med54_3_tot-med50_3_tot;
SUB_103101 = med103_3_tot-med101_3_tot;

% 52-50
massimo_1 = max(SUB_5250(:)); minimo_1 = min(SUB_5250(:));
[indice_riga_1, indice_colonna_1] = find(SUB_5250 == massimo_1);
% 54-52
massimo_2 = max(SUB_5452(:)); minimo_2 = min(SUB_5452(:));
[indice_riga_2, indice_colonna_2] = find(SUB_5452 == massimo_2);
% 54-50
massimo_3 = max(SUB_5450(:));minimo_3 = min(SUB_5450(:));
[indice_riga_3, indice_colonna_3] = find(SUB_5450 == massimo_3);
% 103-101
massimo_4 = max(SUB_103101(:));minimo_4 = min(SUB_103101(:));
[indice_riga_4, indice_colonna_4] = find(SUB_103101 == massimo_4);
%%
figure
subplot(1, 2, 1)
meshc(SUB_5250); colormap(jet); colorbar;
title('Difference␣between␣52␣and␣50␣mm␣depth', 'Interpreter', 'latex', 'FontSize', 16)
xlabel('Pixel␣value␣of␣ROI', 'Interpreter', 'latex', 'FontSize', 16)
ylabel('Pixel␣value␣of␣ROI', 'Interpreter', 'latex', 'FontSize', 16)
zlabel('Difference␣[ADU]', 'Interpreter', 'latex', 'FontSize', 16)

subplot(1, 2, 2)
meshc(SUB_103101); colormap(jet); colorbar;
title('Difference␣between␣103␣and␣101␣mm␣depth', 'Interpreter', 'latex', 'FontSize', 16)
xlabel('Pixel␣value␣of␣ROI', 'Interpreter', 'latex', 'FontSize', 16)
ylabel('Pixel␣value␣of␣ROI', 'Interpreter', 'latex', 'FontSize', 16)
zlabel('Difference', 'Interpreter', 'latex', 'FontSize', 16)
sgtitle('Examples␣of␣subtraction␣with␣Median␣filter', 'Interpreter', 'latex', 'FontSize', 18)
% TABLE
depths = [5250, 5452, 5450 ,103101];
peak_values = [massimo_1, massimo_2, massimo_3, massimo_4];
min_values = [minimo_1, minimo_2, minimo_3, minimo_4];
peak_indices = [indice_colonna_1, indice_colonna_2, indice_colonna_3,indice_colonna_4];
T = table(depths', peak_values', min_values',peak_indices',  ...
    'VariableNames', {'Subtraction', 'Peak␣Value', 'Min␣Values' 'Peak␣Index'});
disp(T);

%% 2. Re-binning
L_kernel = 3; % Only change the kernel value

n_righe = size(Paint_new_50{1},1); n_colonne = size(Paint_new_50{1},2);
```

```
size_1= round(size(Paint_new_50{1},1)/L_kernel);
size_2 = round(size(Paint_new_50{1},2)/L_kernel);

immagine_ricomposta={}; immagine_ricomposta_diff = {};
for s =1:numImages
    for i = 1:L_kernel:(size(Paint_new_50{1},1)-L_kernel)
        for j = 1:L_kernel:(size(Paint_new_50{1},2)-L_kernel)

            finestra_50 = Paint_new_50{s}(i:i+(L_kernel-1), j:j+(L_kernel-1));
            finestra_52 = Paint_new_52{s}(i:i+(L_kernel-1), j:j+(L_kernel-1));
            finestra_54 = Paint_new_54{s}(i:i+(L_kernel-1), j:j+(L_kernel-1));
            finestra_101 = Paint_new_101{s}(i:i+(L_kernel-1), j:j+(L_kernel-1));
            finestra_103 = Paint_new_103{s}(i:i+(L_kernel-1), j:j+(L_kernel-1));

            media_50 = mean(finestra_50(:)); media_52 = mean(finestra_52(:));
            media_54 = mean(finestra_54(:));
            media_101 = mean(finestra_101(:)); media_103 = mean(finestra_103(:));

            immagine_ricomposta_50{s}((i-1)/L_kernel + 1, (j-1)/L_kernel + 1) = media_50;
            immagine_ricomposta_52{s}((i-1)/L_kernel + 1, (j-1)/L_kernel + 1) = media_52;
            immagine_ricomposta_54{s}((i-1)/L_kernel + 1, (j-1)/L_kernel + 1) = media_54;
            immagine_ricomposta_101{s}((i-1)/L_kernel + 1, (j-1)/L_kernel + 1) = media_101;
            immagine_ricomposta_103{s}((i-1)/L_kernel + 1, (j-1)/L_kernel + 1) = media_103;
        end
    end
end

%% SUBTRACTION
% To make the value more repeatable an average image between the three was taken
bin50_3_tot= (immagine_ricomposta_50{1,1} + immagine_ricomposta_50{1,2} + immagine_ricomposta_50{1,3})/3;
bin52_3_tot= (immagine_ricomposta_52{1,1} + immagine_ricomposta_52{1,2} + immagine_ricomposta_52{1,3})/3;
bin54_3_tot= (immagine_ricomposta_54{1,1} + immagine_ricomposta_54{1,2} + immagine_ricomposta_54{1,3})/3;
bin101_3_tot= (immagine_ricomposta_101{1,1} + immagine_ricomposta_101{1,2} + immagine_ricomposta_101{1,3})/3;
bin103_3_tot= (immagine_ricomposta_103{1,1} + immagine_ricomposta_103{1,2} + immagine_ricomposta_103{1,3})/3;

massimo_50 = max(bin50_3_tot(:)); [indice_riga_50, indice_colonna_50] = find(bin50_3_tot == massimo_50);
massimo_52 = max(bin52_3_tot(:));[indice_riga_52, indice_colonna_52] = find(bin52_3_tot == massimo_52);
massimo_54 = max(bin54_3_tot(:));[indice_riga_54, indice_colonna_54] = find(bin54_3_tot == massimo_54);
massimo_101 = max(bin101_3_tot(:));[indice_riga_101, indice_colonna_101] = find(bin101_3_tot == massimo_101);
massimo_103 = max(bin103_3_tot(:));[indice_riga_103, indice_colonna_103] = find(bin103_3_tot == massimo_103);

% Table
depths = [50, 52, 54, 101, 103];
peak_values = [massimo_50, massimo_52, massimo_54, massimo_101, massimo_103];
peak_indices = [indice_colonna_50, indice_colonna_52, indice_colonna_54, indice_colonna_101, indice_colonna_103];
T = table(depths', peak_values', peak_indices',  ...
    'VariableNames', {'Depth', 'Peak_Value', 'Peak_Index'});
disp(T);


%% Subtraction
SUB_5250 = bin52_3_tot-bin50_3_tot; SUB_5452 = bin54_3_tot-bin52_3_tot;
SUB_5450 = bin54_3_tot-bin50_3_tot;
SUB_103101 = bin103_3_tot-bin101_3_tot;

massimo_1 = max(SUB_5250(:)); minimo_1 = min(SUB_5250(:));
```

```
[indice_riga_1, indice_colonna_1] = find(SUB_5250 == massimo_1);
massimo_2 = max(SUB_5452(:)); minimo_2 = min(SUB_5452(:));
[indice_riga_2, indice_colonna_2] = find(SUB_5452 == massimo_2);
massimo_3 = max(SUB_5450(:));minimo_3 = min(SUB_5450(:));
[indice_riga_3, indice_colonna_3] = find(SUB_5450 == massimo_3);
massimo_4 = max(SUB_103101(:));minimo_4 = min(SUB_103101(:));
[indice_riga_4, indice_colonna_4] = find(SUB_103101 == massimo_4);

figure
subplot(1, 2, 1)
meshc(SUB_5250);colormap(jet); colorbar;
title(’Difference␣between␣52␣and␣50␣mm␣depth’, ’Interpreter’, ’latex’, ’FontSize’, 16)
xlabel(’Pixel␣value␣of␣ROI’, ’Interpreter’, ’latex’, ’FontSize’, 16)
ylabel(’Pixel␣value␣of␣ROI’, ’Interpreter’, ’latex’, ’FontSize’, 16)
zlabel(’Difference␣[ADU]’, ’Interpreter’, ’latex’, ’FontSize’, 16)

subplot(1, 2, 2)
meshc(SUB_103101); colormap(jet); colorbar;
title(’Difference␣between␣103␣and␣101␣mm␣depth’, ’Interpreter’, ’latex’, ’FontSize’, 16)
xlabel(’Pixel␣value␣of␣ROI’, ’Interpreter’, ’latex’, ’FontSize’, 16)
ylabel(’Pixel␣value␣of␣ROI’, ’Interpreter’, ’latex’, ’FontSize’, 16)
zlabel(’Difference’, ’Interpreter’, ’latex’, ’FontSize’, 16)
sgtitle(’Examples␣of␣subtraction␣with␣Manual␣Binning’, ’Interpreter’, ’latex’, ’FontSize’, 18)

% Table
sub = [5250, 5452, 5450 ,103101];
peak_values = [massimo_1, massimo_2, massimo_3, massimo_4];
min_values = [minimo_1, minimo_2, minimo_3, minimo_4];
peak_indices = [indice_colonna_1, indice_colonna_2, indice_colonna_3,indice_colonna_4];
T = table(sub’, peak_values’, min_values’,peak_indices’,  ...
    ’VariableNames’, {’Depth’, ’Peak␣Value’, ’Min␣Values’ ’Peak␣Index’});
disp(T);

%%
figure
subplot(1, 2, 1)
meshc(SUB_5250); colormap(jet); colorbar;
title(’Difference␣between␣52␣and␣50␣mm␣depth’, ’Interpreter’, ’latex’, ’FontSize’, 16)
xlabel(’Pixel␣value␣of␣ROI’, ’Interpreter’, ’latex’, ’FontSize’, 16)
ylabel(’Pixel␣value␣of␣ROI’, ’Interpreter’, ’latex’, ’FontSize’, 16)
zlabel(’Difference␣[ADU]’, ’Interpreter’, ’latex’, ’FontSize’, 16)

subplot(1, 2, 2)
meshc(SUB_103101); colormap(jet); colorbar;
title(’Difference␣between␣103␣and␣101␣mm␣depth’, ’Interpreter’, ’latex’, ’FontSize’, 16)
xlabel(’Pixel␣value␣of␣ROI’, ’Interpreter’, ’latex’, ’FontSize’, 16)
ylabel(’Pixel␣value␣of␣ROI’, ’Interpreter’, ’latex’, ’FontSize’, 16)
zlabel(’Difference’, ’Interpreter’, ’latex’, ’FontSize’, 16)
sgtitle(’Examples␣of␣subtraction␣with␣Re–binning’, ’Interpreter’, ’latex’, ’FontSize’, 18)
```

ARDUINO CODE

```
int sensorPin = 2;
int outputPin = 6;
boolean pulseTrainActive = false;
const int pulsePeriodMicros = 100;
const int pulseDurationMicros = 50;
int pulsenumber;
int sensorValue;
const int exposureTime = 210;  //  Impose here the exposure time put on the camera with a +10 value (margin)

unsigned long currentTime;
unsigned long startTime;

void setup() {
  pinMode(outputPin, OUTPUT); // This sets the outputPin as an OUTPUT
  pinMode(sensorPin, INPUT);
}

void loop() {
  sensorValue = digitalRead(sensorPin);
  if (sensorValue == HIGH) { // If the sensor detects a HIGH state the Pulse Train is generated
    generatePulseTrain();
  }
}

void generatePulseTrain() {
  // Keep track of the start time for additional pulses, millis is used to mark the current
  // time when the initial pulse train end and the code enters the section to generate additional pulses
  unsigned long startAdditionalPulsesTime = millis();

  while (sensorValue == HIGH) {
    digitalWrite(outputPin, HIGH);
    delayMicroseconds(pulseDurationMicros);
    digitalWrite(outputPin, LOW);
    delayMicroseconds(pulsePeriodMicros - pulseDurationMicros);

    // Update the sensor value
    sensorValue = digitalRead(sensorPin);
  }

//
  if (millis() - startAdditionalPulsesTime >= 10) {
    // Here it checks if after the initial pulse train at least 10 ms have intercurred
    // The image is taken because the pulse train starts but there won't be another image taken
    // If the signal lasts longer than 10 ms:
    // Generate additional pulses for the exposure time in milliseconds (+10 ms to be sure)
    unsigned long additionalPulsesEndTime = millis() + exposureTime;
    while (millis() < additionalPulsesEndTime) {
```

```
      digitalWrite(outputPin, HIGH);
      delayMicroseconds(pulseDurationMicros);
      digitalWrite(outputPin, LOW);
      delayMicroseconds(pulsePeriodMicros - pulseDurationMicros);
    }
  }
}
```

Ringraziamenti

Desidero esprimere la mia sincera gratitudine a tutte le persone che hanno contribuito al successo di questa tesi con il loro supporto.

Innanzitutto, voglio ringraziare il mio relatore, il Professor Gianni Coppa che, tramite le sue lezioni, mi ha trasmetto l'interesse verso questo argomento.

Ringrazio il Dottor Marco Pullia, mio relatore presso il CNAO, per la sua guida esperta e il suo costante sostegno durante tutto il processo di ricerca. La sua passione verso il suo lavoro e la sua eccezionale preparazione hanno sicuramente plasmato il risultato di questo lavoro.

Un ringraziamento speciale va anche al Dottor Simone Savazzi, che mi ha affiancato durante questo percorso e al Dottor Guglielmo Frisella, i loro contributi e feedback hanno arricchito notevolmente questa tesi.